論文 / 著書情報
Article / Book Information

題目(和文)	バー型海岸における水理特性および地形変化特性
Title(English)	Hydro- and morpho-dynamics on a barred beach
著者(和文)	栗山善昭
Author(English)	Yoshiaki Kuriyama
出典(和文)	学位:博士(工学), 学位授与機関:東京工業大学, 報告番号:乙第3535号, 授与年月日:2001年4月30日, 学位の種別:論文博士, 審査員:
Citation(English)	Degree:Doctor (Engineering), Conferring organization: Tokyo Institute of Technology, Report number:乙第3535号, Conferred date:2001/4/30, Degree Type:Thesis doctor, Examiner:
学位種別(和文)	博士論文
Type(English)	Doctoral Thesis

Hydro- and Morpho-Dynamics on a Barred Beach

April, 2001

Yoshiaki KURIYAMA

Contents

1. Introduction

1.1 Background of this study

The surf zone is the region extending from the wave breaking zone to the shore, where waves and currents are strong and cause large amounts of sediment transport and topographic variation. This makes the surf zone a crucial area in coastal management. The surf zone also plays an important role in the ecosystem because it forms the transition zone linking the marine and terrestrial environments.

Longshore bars, which are underwater ridges of sand (Komar, 1998), are frequently formed in the surf zone of sandy beaches. During storms, waves break on bar crests and reform at troughs. As a result, wave deformation, nearshore currents and beach profile variations are different on barred beaches compared to planar beaches.

The influence of longshore bars on the topographic variations in the foreshore has been previously shown by Yamamoto and Sato (1998). They conducted experiments in a large flume and showed that the shoreline on a barred beach, which normally advanced in mild wave conditions, did not advance under these conditions after the longshore bar had been removed. This result indicates that shoreline management should pay close attention to longshore bar movement. The revision of the Coastal Act in Japan in 1999, which requires coastal management over a wider region, encourages attention to the bar movement.

Longshore bars also influence longshore sediment transport. The cross-shore distribution of the longshore sediment transport rate on a barred beach is expected to change according to the size or the location of a longshore bar. Though coastal structures such as groins, jetties and detached breakwaters are useful for protection of beaches against erosion, these coastal structures also trap some of the sediment that is transported alongshore and therefore influence the sediment budget in the down-drift region. Consequently, design features of coastal structures, such as their length and location, should be carefully considered. Understanding and predicting bar movements as well as waves and currents over longshore bars are essential in designing coastal structures on barred beaches.

The investigation of waves, currents and morphological variations over bar-trough topography is also required from the standpoint of beach nourishment. In the United States, Australia and Europe, an offshore nourishment technique has been recently

developed as a cost effective nourishment method (e.g., McLellan and Kraus, 1991; Murray et al., 1994). In this method, sediment is placed in the nearshore, and is expected to move shoreward, or at least to stay in the nearshore. Since the nourished sediment forms a bar, understanding of bar movements as well as waves and nearshore currents over bars is essential to ensure the effectiveness of the offshore nourishment technique.

Longshore bars also provide different ecosystems than those on planar slopes. Higano and Yasunaga (1988) reported that a bivalve species which lives seaward of a bar crest is different from that which lives shoreward of the crest. The ecosystems are expected to be influenced by the nearshore current based on the investigation by Fleischack and Freitas (1989), who showed that there is a correlation between longshore current velocity and the zonation of benthos. Hence, investigations on the influence of longshore bars on physical environment are also required for understanding nearshore ecosystems.

1.2 Aim and scope of this study

The objective of this study is to investigate hydro- and morpho-dynamics on a barred beach using field data and numerical simulations. The field data were mainly obtained at Hazaki Oceanographical Research Station (HORS), which is described in section 1.3.

Morphodynamics on a barred beach are investigated in Chapter 2. Although numerous studies have been undertaken to understand bar behavior, which involves bar generation, migration and decay, the processes of sediment movement associated with the bar behavior, which is important in coastal zone management, have not been fully investigated. Furthermore, the effect of wave characteristics on medium-term bar movement and sediment transport is poorly understood. Hence, Chapter 2 discusses the medium-term bar movement, sediment transport associated with the bar movement and the relationship between the sediment transport and wave characteristics.

In Chapter 3, waves over longshore bars are examined. Nearshore currents, sediment suspension, and morphological variation in the surf zone are mainly caused by turbulence, mass flux and momentum flux induced by breaking waves. Breaking waves have a much greater influence on these factors than do non-breaking waves. Hence, it is essential to accurately estimate the conditions for wave breaking and wave reforming.

However, previous investigations did not include field studies of wave reforming at troughs, which is a peculiar phenomenon of a barred beach. As a result, previous models could not accurately predict the fraction of breaking waves (the ratio of the number of breaking waves to the total number of waves) at troughs, though these models could quantitatively or at least qualitatively predict this fraction on planar beaches and on the seaward slopes of longshore bars. Chapter 3 describes how field measurements of wave breaking and wave reforming were carried out over longshore bars and troughs, and the conditions at the time of wave reforming. On the basis of the wave conditions at the time of wave reforming, a model for wave height and the fraction of breaking waves is developed and verified with field and large-scale experimental data.

The objective of Chapter 4 is to investigate the characteristics of the cross-shore distribution of the longshore current velocity on barred beaches on the basis of field data acquired at HORS and numerical simulations. It is known that obliquely incident waves induce longshore currents. So far, two types of cross-shore distributions of the longshore current velocity have been reported; one type has a peak velocity seaward of the bar crest, and the other has a peak velocity shoreward of the bar crest. The frequencies and causes of the two types of distributions have not yet been thoroughly evaluated.

The discussion in Chapter 4 shows that the momentum flux due to bores, *i.e.*, surface rollers, plays an important role in the cross-shore distribution of the longshore current velocity. The momentum flux due to surface rollers, which also has strong influence on undertow velocity, was included in previous models for longshore current and nearshore current. Few models, however, have been verified with field data. Thus, in Chapter 5, a one-dimensional model that includes the surface roller effect is developed to describe undertow and longshore current, and calibrated with field data obtained over longshore bars at HORS. The model is then verified with data from large-scale experiments and other field measurements. In addition, on the basis of the model, causes of the cross-shore distribution of the longshore current velocity on a barred beach in the field are discussed.

Finally, summary and conclusions are provided in Chapter 6.

1.3 Hazaki Oceanographical Research Station

The Hazaki Oceanographical Research Station (HORS) is a research facility for field measurements of various phenomena in the nearshore zone, and was constructed in 1986 by the Port and Harbour Research Institute, Ministry of Transport. HORS is located on the Hasaki coast of Japan facing the Pacific Ocean (Figure 1.1). HORS consists of offices, storerooms, and a 427-meters-long pier; the pier deck is 3.3 m wide and 6.9 m above the low water level, and is supported on single pilings. Hereafter, "HORS" will be used with reference to the pier.

Based on the datum level at Hasaki (Tokyo Peil –0.687 m), the high, the mean and the low water levels are 1.252 m, 0.651 m, and –0.196 m, respectively. Large waves are mainly generated by typhoons from July to September and by strong atmospheric depressions from February to April.

The beach profile along HORS is measured at 5 m intervals every day, except for weekends and holidays, using a 5 kg lead on the pier, and using a level and a staff shoreward of the pier. The median sediment diameter is 0.18 mm and almost uniform along HORS, whereas it varied from 0.15 mm to 1.0 mm in troughs (Katoh and Yanagishima, 1995).

Water surface elevations along HORS are measured with several ultrasonic wave gages installed along one side of the pier, and offshore waves are measured offshore of the Kashima Port at a water depth of 23.4 m; the location of the offshore wave gage is also shown in Figure 1.1. Besides the ultrasonic wave gages, HORS provides electro magnetic current meters, optical back-scatterance sensors (OBS), anemometers and other sensors.

Figure 1.2 shows the co-ordinate system used in this study. The positive directions of the x-axis and the y-axis are southward and seaward, respectively. The vertical (z) axis extends upwards. Elevations are relative to the datum level in Hasaki (D.L.). The wave direction is defined relative to the shore and is positive in the counterclockwise direction.

A position along HORS will be referred to as the offshore distance relative to the reference point, located near the entrance of the pier, and the mark "P"; for example, P230m denotes the position where the offshore distance is 230 m.

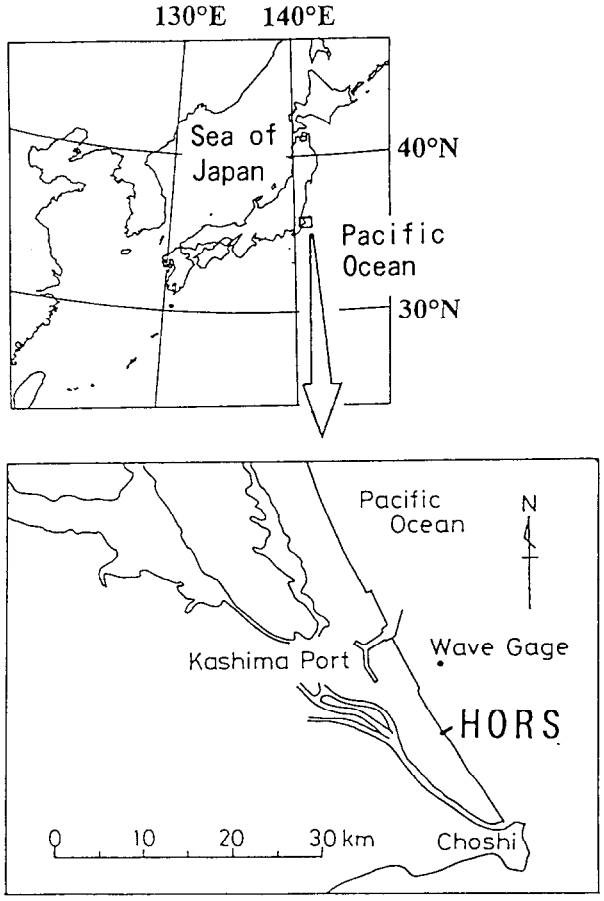

Figure 1.1 Location of HORS.

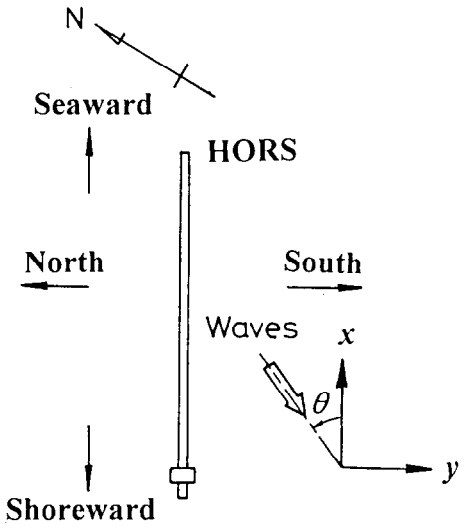

Figure 1.2 Definition sketch of co-ordinate system.

2. Medium-term bar behaviour and the associated sediment transport

2.1 Introduction

Studies of longshore bar started in the 19th century (Komar, 1998). Recently, long-term and medium-term topography data have been obtained using echo-sounding and video technique, and long-term and medium-term bar movements on several coasts in the United States, the Netherlands and New Zealand have been investigated (Birkemeier, 1984; Lippmann et al., 1993; Ruessink and Kroon, 1994; Wijnberg and Terwindt, 1995; Shand and Bailey, 1999). These studies focused on bar behavior including bar generation, movement and decay, but little attention was paid to the sediment movement associated with the bar behavior, which is important in coastal zone management. Ruessink and Terwindt (2000) proposed a model in which knowledge of sediment movement in short-term process is aggregated to explain medium-term bar movement. The model partially succeeded in reproducing the medium-term bar movement, but could not explain the bar generation process; the processes of the sediment movement during bar generation were still unknown.

Furthermore, the effect of wave characteristics on the medium-term bar movement and the sediment transport is poorly understood in spite of the numerous studies on short-term bar movement and wave characteristics (e.g., Sallenger et al., 1985; Sallenger and Howd, 1989; Lippmann and Holman, 1990; Greenwood and Osborne, 1991; Larson and Kraus, 1992; Sunamura and Takeda, 1993; Kuriyama, 1996; Thornton et al., 1996; Plant and Holman, 1997; Gallagher et al., 1998; Aagaard and Greenwood, 1999; Miller et al., 1999). Plant et al. (1999) and Larson et al. (2000) investigated the relationship between medium-term beach profile changes and wave characteristics. Plant et al. (1999) proposed a model to predict bar crest movement with the offshore wave height, and Larson et al. (2000) showed a strong correlation between the beach profile and the ratio of wave breaking using canonical correlation analysis.

The objective of this chapter is to discuss medium-term bar movement, sediment movement associated with the bar movement and the relationship between the sediment movement and wave characteristics on the basis of beach profile data obtained at HORS.

2.2 Beach Profile Data

Beach profile data used in this study were obtained over the course of eight years from January in 1987 to December in 1994 at HORS. The upper part of Figure 2.1 shows the mean beach profile and the maximum and minimum values of elevation from 1987 to 1994, and the lower one shows the standard deviation in elevation. Since local scours occur around pilings supporting the pier deck of HORS, the elevations measured at the survey points close to the pilings were replaced by the values that were obtained by interpolating with the elevations measured where the effects of the scours were negligible shoreward and seaward of the pilings; the survey points close to pilings are located where the offshore distances are 100, 105, 165, 175, 200, 205, 220, 235, 250, 265, 280, 295, 310, 325, 340, 355, 370 and 385 m.

The mean beach slope in the area from P-60m to P200m is about 1/50, and the slope seaward of the area is about 1/120. The standard deviation in elevation increases seaward from around P20m, has a peak around at P210m, and then gradually decreases to P380m.

2.3 Alongshore uniformity of topography near HORS and influence of pilings

The alongshore uniformity of the topography near HORS and the influence of the pilings on the topography were examined using seventeen topographic maps of the area near HORS; these maps were obtained from November 1986, when the influence of the construction work of HORS on the topography was assumed to be small, to August 1998. Besides the daily surveying at HORS, the bottom topography around HORS was surveyed once or twice a year in the area that is 600 m wide in the alongshore direction and about 700 m long in the cross-shore direction. Figure 2.2 shows an example of the topography near HORS. The alongshore interval of the survey lines expanding cross-shore was 50 m, and the cross-shore intervals of the survey points were 10 m shoreward of the points where the offshore distance was 150 m, and 20 m seaward of the points.

Figure 2.3 shows the mean beach profiles and the standard deviations in elevation along HORS and along six survey lines. Three of the six lines are located north of HORS, and the others are located south of HORS. The alongshore distances between the survey lines and HORS range from 200 m to 300 m. At a distance from HORS, the mean elevations are in close agreement, as are the standard deviations. This result

indicates that the topography near HORS was generally uniform alongshore.

Along HORS, however, from P200m to P400m, the elevation of the mean beach profile is lower and the standard deviation in elevation is larger than those at a distance from HORS. This is probably caused by local scours around pilings. Nevertheless, the beach profile data along HORS can still be used for the investigation of medium-term beach profile changes at Hasaki, provided that the beach profile change along HORS qualitatively agrees with that at a distance from HORS. Thus, the relationship between the beach profiles along HORS and at a distance from HORS was further investigated.

As parameters representing beach profiles on barred beaches, the elevations and the locations of bar crests and troughs were chosen. The parameters along HORS were compared with those in a northern and a southern regions; the northern and the southern regions cover the areas 200 m to 300 m north and south of HORS, respectively. The bar crest and the trough were defined to be the points that had the local maximum and minimum elevations, respectively. The local maximum and minimum elevations were defined to have a beach slope of zero; the beach slope was estimated as the mean slope in the area of 60 m cross-shore. Even though the bar crest and the trough were defined to be the points with the local maximum and minimum elevations, a bar whose height (i.e., difference in elevation between the bar crest and the shoreward trough) was below certain criteria was eliminated. The bar height criteria were set to be 50 cm along HORS and 30 cm at a distance from HORS because the standard deviation in elevation along HORS was larger than those at a distance from HORS (Figure 2.3). The elevations and the locations of the bar crests and the troughs in the northern and the southern regions were estimated on the basis of the mean beach profiles in the regions.

Figures 2.4 (1) and (2) show comparisons between the elevations and the locations of the bar crests and the troughs along HORS and those at a distance from HORS. As shown in Figure 2.4 (1), the locations and the elevations of the bar crests along HORS agree very well with those at a distance from HORS. At the troughs, on the other hand, elevations along HORS are deeper than those at a distance from HORS (Figure 2.4 (2)). This is thought to be caused by local scours. However, even though elevations at the troughs along HORS are lower than those at a distance from HORS, the locations of the troughs along HORS agree with those at a distance from HORS. This means the locations of the troughs were not greatly influenced by scours.

In summary, the results of the analysis on the alongshore uniformity of the topography near HORS show: a) the topography near HORS was generally uniform alongshore, b) the pilings had a negligible effect on topography on and around the bar crests, and c) although elevations of the troughs along HORS were lower than those at a distance from HORS, the locations of the troughs along HORS agreed well with those at a distance from HORS. With these findings, it is concluded that the beach profile changes represented by bar movements at HORS were not much disturbed by scours of the pilings.

This conclusion is similar to that shown by Miller et al. (1983) for the Field Research Facility (FRF) in the United States. The FRF is a 561 m long field observation pier, and is located on the Atlantic Ocean in Duck, North Carolina. Miller et al. (1983) investigated beach profile changes along and at a distance from the FRF with an empirical eigenfunction analysis, and concluded that the beach profile changes along the FRF associated with bar movements were not disturbed by the pilings. The FRF is supported by double pilings, whereas HORS is supported by single pilings. Hence, the conclusion that the beach profile change at HORS was not much influenced by the pilings is reasonable.

2.4 Results

2.4.1 Medium-term bar movement

Figure 2.5 shows a space-time map of the variation from the time-averaged beach profile at HORS from 1987 to 1994. Although accumulations and erosions occurred alternatively with time shoreward of P150m, accumulated areas seaward of P150m repeatedly moved seaward with a period of about a year.

Then, the difference between the beach profile changes in the seaward and the shoreward regions was investigated by applying the power spectrum analysis to the elevations at P0m and P300m, which were selected as representative points in the shoreward and the seaward regions, respectively. Figure 2.6 shows that the power spectrum at P0m has a broad peak over periods of about 300 to 500 days and a sharp peak at a period of 190 days, whereas the spectral density at P300m is concentrated at a period of a year.

Investigations of bar crest migration revealed that seaward of P200m, the bar crest

migrated seaward with a period of a year as shown in Figure 2.7; this behavior is particularly evident between 1987 and 1992. A bar crest was generated at around P180m, migrated seaward, and reached the tip of HORS about a year after the beginning of the migration. Almost at the same time when the bar crest reached the tip of HORS, a new bar crest was generated at around P180m and began to migrate seaward.

Since no bars were observed seaward of P450m as shown in Figure 2.4 (1), bar crests are expected to migrate seaward and disappear shortly after reaching the tip of HORS. Hence, at HORS, the duration time of the bar crest migration, which is a period when a bar exists, is assumed to be approximately equal to the return period of the bar crest migration, which is a period between bar migration cycles, whereas the duration time is longer than the return period in eight out of nine coasts investigated by Shand and Bailey (1999).

An empirical eigenfunction analysis was applied to the beach profiles at HORS. In this paper, an eigenfunction is derived from a covariance matrix based on variations from the mean as in Birkemeier (1984). Figures 2.8 (1) to (3) show the first three eigenfunctions and their temporal weightings; the variances explained by the three eigenfunctions from the first are 42 %, 28 % and 8 %. The first two eigenfunctions are large only seaward of P150m, whereas the third is large even close to the shore at around P0m. Figure 2.9 shows the cross-shore distribution of the variance at each location explained by the first three eigenfunctions. These results, shown in Figures 2.8 and 2.9, suggest that the first two eigenfunctions represent beach profile changes in the nearshore and the third one in the foreshore. Although the third eigenfunction gives the variances in the foreshore, from P-40m to P100m, that are below 50% (Figure 2.9), the correlation between C_3 and the shoreline position from the mean is strong as shown in Figure 2.10. This result confirms that the third eigenfunction represents beach profile changes in the foreshore.

The second eigenfunction e_2 has a phase difference of $\pi/2$ (one fourth of the wavelength) from the first eigenfunction e_1 as shown in Figures 2.8 (1) and (2). The temporal weighting on the second eigenfunction C_2 also has a phase difference of $\pi/2$ from that on the first eigenfunction C_1 as shown by the cross spectra between C_1 and C_2 in Figure 2.11. Wijnberg and Wolf (1994) showed that the superposition of two eigenfunctions with a phase difference of $\pi/2$ in their shapes and temporal weightings

represents a bar crest migration, which is a progressive wave motion. The superposition of the beach profile changes reconstructed by the first two eigenfunctions at HORS also represents the seaward migration of the bar crest in the nearshore as shown in Figure 2.12.

2.4.2 Bar movement and cross-shore sediment transport

To examine sediment transport rates associated with the medium-term bar crest migration, low frequency components (<0.006 cycle/day, >160 days) of cross-shore sediment transport rates per unit length in the alongshore direction at three locations, P210m, P260m and P310m, were investigated. Figure 2.13 shows the low frequency components together with the bar crest migration. The transport rates were estimated using the beach profiles reconstructed by the first two eigenfunctions on the basis of three assumptions. The first is that the beach profile change was not influenced by the gradient of the longshore sediment transport rate. The second is that the cross-shore sediment transport rate was zero at P-115m, the shoreward limit of the survey area and located at the foot of a dune. The third is that the porosity is equal to 0.4. The shoreward sediment transport was defined to be positive.

Although the bar crest migrates almost only in the seaward direction, the cross-shore sediment transport rates fluctuate shoreward and seaward. Furthermore, there are phase differences among the transport rates. The cross spectra between the cross-shore sediment transport rates at P210m and P260m, and those between the rates at P260m and P310m in Figure 2.14 show two main features. First, the spectral density of the cross-shore sediment transport rate is high at periods of a year and six months, and second, the fluctuation at P210m precedes that at P260m by $\pi/4$ to $\pi/2$, whereas the fluctuation at P310m is later than that at P260m by $\pi/4$ to $\pi/2$.

Figure 2.15 shows a time-space map of the low frequency component of the cross-shore sediment transport rate seaward of P150m. The fluctuation in Figure 2.15 is similar to that in Figure 2.12. As the accumulation areas move seaward, the areas where the seaward sediment transport occurred move seaward. Similarly, as the erosion areas move seaward, the areas with the shoreward sediment transport move seaward.

Hence, the correlation between the cross-shore sediment transport and beach profile was examined. Figure 2.16 shows cross-shore distributions of the low frequency

component of the cross-shore sediment transport rate (upper panels) and beach profiles (lower panels) in 1989; those in the first half of the bar crest migration are shown in (a) and those in the second half in (b). Seaward sediment movement occurred on and around the bar crests, while shoreward sediment movement temporally occurred there in August as shown in (b). In contrast, shoreward sediment movement occurred in the trough regions. The phase differences among the cross-shore sediment transport rates shown in Figure 2.13 are likely attributed to the differences in times when the bar crests reached the three locations.

Figure 2.16 also shows the development and decay of a bar during the seaward bar crest migration; the bar height increased in the first half of the bar crest migration, and decreased in the second half. The cross-shore distribution of the bar height averaged over the eight years is shown in Figure 2.17, where the location of a bar is defined to be the middle point of the bar crest and the trough. The bar height increases from P200m to P250m, has a peak at around P250m, and then decreases to P380m like the bar deformation shown in Figure 2.16. This bar height variation is probably caused by the cross-shore distribution of the cross-shore sediment transport rate. To further evaluate this hypothesis, the root-mean-square value of the cross-shore sediment transport rate at each survey point $Q_t(y)$ was calculated using Eq. (2.1).

$$Q_t(y) = \sqrt{\sum_{t=1}^{N_t} Q_e(y,t)^2 \Big/ N_t}, \tag{2.1}$$

where y is the offshore distance, t is time, N_t is the number of the data, and $Q_e(y, t)$ is the cross-shore sediment transport rate per unit length in the alongshore direction estimated on the basis of the beach profiles reconstructed by the first two eigenfunctions. Figure 2.18 shows that $Q_t(y)$ rapidly increases from P150m to P250m, and then gradually decreases. This distribution is similar to that of the observed bar height. This seems to mean that the bar height increased to P250m because the magnitude of the cross-shore sediment transport rate increased, and the bar height decreased because the magnitude decreased.

Therefore the relationship between the bar deformation and the cross-shore distribution of the cross-shore sediment transport rate was examined with a simple model. The cross-shore sediment transport rate was assumed to be expressed by a sine function whose amplitude is 0 at P150m and at P350m, and maximum at P250m. This

assumption is based in part on the variation of the cross-shore sediment transport rate, which increases from P150m, reaches the maximum at P250m, and decreases seaward (Figure 2.17). Three additional assumptions were also made: (a) the period of the temporal variation in the cross-shore sediment transport rate is a year (365 days), (b) the variation moves seaward at a constant speed, and (c) the wavelength of the cross-shore distribution of the sediment transport rate is 200 m. Assumption (c) is based on the cross-shore distributions of the cross-shore sediment transport rate shown in Figure 2.16. Accordingly, the variation of the cross-shore sediment transport rate $Q_c(y, t)$ is expressed by

$$Q_c(y,t) = A\sin(k_2 y')\sin(k_1 y' - \sigma t), \tag{2.2}$$

where A is the maximum amplitude of the variation of the cross-shore sediment transport rate, $k_2 = 2\pi/L_2$, L_2 is the wavelength of the cross-shore distribution of the amplitude (= 400 m), $y' = y - 150$, $k_1 = 2\pi/L_1$, L_1 is the wavelength of the cross-shore distribution of the sediment transport rate (= 200 m), σ is the angular frequency (= $2\pi/T$), and T is the period of the variation in cross-shore sediment transport rate (= 365 days).

Let $z(y, t)$ be elevation relative to the mean profile. Because $\partial z/\partial t = \partial Q/\partial y$, the elevation becomes $z = \int \partial Q/\partial y \, dt$. As a result, $z(y, t)$ can be expressed as

$$\begin{aligned} z(x,t) &= \frac{A}{\sigma}\sqrt{A_1^2 + A_2^2}\,\sin(k_1 x' - \sigma t + \alpha), \\ A_1 &= k_2 \cos k_2 x', \quad A_2 = -k_1 \sin k_2 x', \\ \tan\alpha &= A_1 / A_2. \end{aligned} \tag{2.3}$$

Figure 2.19 shows beach profiles estimated with Eq. (2.3); the variation is normalized by the maximum value at P250m. The bar height increases from P150m to P250m, and then decreases to P350m. This result indicates that the bar development and decay is caused by the cross-shore distribution of the cross-shore sediment transport rate with a peak at P250m.

2.4.3 Cross-shore sediment transport and wave energy

The relationship between the cross-shore sediment transport rate and wave energy in deep water is now discussed. First, the magnitude of the cross-shore sediment transport, which is a scalar value, was examined. As a parameter representing the magnitude, the

root-mean-square value of the cross-shore sediment transport rates from P150m to P380m $Q_s(t)$ was taken.

$$Q_s(t) = \sqrt{\sum_{y=150}^{380} Q_e(y,t)^2 \Big/ N_y}\,, \tag{2.4}$$

where N_y is the number of data.

The wave energy flux in deep water $E_f(t)$ was estimated with Eq. (2.3) on the basis of the offshore wave data, obtained at a water depth of 23.4 m.

$$E_f(t) = \frac{1}{16}\rho g (H_{1/3})_0^2 C_g\,, \tag{2.5}$$

where ρ is the density of sea water, g is the gravitational acceleration, $(H_{1/3})_0$ is the offshore significant wave height, and C_g is the group velocity.

Figure 2.20 shows the cross spectra between $Q_s(t)$ and E_f. The coherence is high, and the phase difference is almost 0. This means that the sediment movement was active when the offshore wave energy flux was large, as might be expected.

The cross-shore sediment transport was then investigated with consideration of the direction of the sediment movement. Figure 2.21 shows the seasonal variations in the low frequency components of the cross-shore sediment transport rates at P210m, P260m and P310m (the middle panel), and E_f (the lower panel) as well as those in elevations at these points (the upper panel). Note that the shoreward direction of sediment transport is defined to be positive.

The energy flux is large from winter to spring owing to depressions and in autumn owing to typhoons, whereas the energy flux is small in summer. The sediment transport rates at the three points are mainly seaward from winter to spring. The peak value of the seaward sediment transport rate moves seaward during this period. Although the sediment transport rates are small in summer, they become large in the shoreward direction in autumn; the peaks of the shoreward sediment transport rates move seaward, analogous to the peaks of the seaward sediment transport rates.

The seaward sediment transport at the points during the period from winter to spring corresponds to the existence of a bar at the points, whereas shoreward sediment transport in autumn corresponds to the existence of a trough. As shown in Figure 2.21, the shift in the peak value of the seaward sediment transport rate is correlated with the bar crest movement, and that of the shoreward sediment transport rate is correlated with

the trough movement.

The correlation between the sediment movement and the beach profile change is also seen in Figures 2.12 and 2.15. As bar crests move seaward from winter to spring (Figure 2.12), regions with the seaward sediment transport rate migrate seaward (Figure 2.15). Similarly, regions with the shoreward sediment movement rate migrate seaward in autumn according to the movement of the trough regions.

2.4.4 Summary of the bar movement and cross-shore sediment transport at Hasaki

On the basis of the investigations described above, the characteristics of the bar crest migration and sediment movement are summarized below.

1) The bar crest moves seaward with a period of a year.

2) In the first half of the bar crest movement, the bar height increases from P180m to P250m, and in the second half the bar height decreases from P250m to P380m.

3) The seaward sediment transport occurs on and around bar crests, whereas the shoreward sediment transport occurs at troughs.

4) The root-mean-square value of the cross-shore sediment transport rate increases from P150m to P250m, has a peak at P250m, and decreases with proximity to P380m.

5) The magnitude of the cross-shore sediment transport rate is strongly positively correlated with the wave energy flux in deep water; i.e., the sediment movement increases when the wave energy flux is large.

6) The wave energy flux is large from winter to spring and in autumn, and small in summer. In the region around P250m, where bars are most developed and large amounts of sediment movement occur, bar crests migrate seaward from winter to spring causing seaward sediment transport. The sediment transport rate changes at a given locality according its proximity to the migrating bar crest. Although the cross-shore sediment transport rate and the beach profile changes near P250m are small during the summer, troughs pass through this region in autumn and the shoreward sediment transport occurs; the shoreward sediment transport rate changes according to the trough movements.

Figure 2.22 schematically shows the bar crest migration and the sediment movement at Hasaki that were described above. The middle panel shows these features in the first half of the bar crest migration from winter to spring, and the lower panel shows them in

the second half in autumn. The variation of the wave energy flux E_f is shown in the upper panel. The kinds of lines used to describe the beach profile correspond to those used to describe the sediment transport and E_f.

2.5 Discussion

The seaward migration of the bar crest at HORS shown in Figure 2.8 is similar to those observed on several coasts in the United States, the Netherlands and New Zealand (Birkemeier, 1984; Lippmann et al., 1993; Ruessink and Kroon, 1994; Wijnberg and Terwindt, 1995; Shand and Bailey, 1999), while the Hasaki Coast, where HORS is located, basically has a single bar in contrast with the other coasts having multiple bars. Bars at Hasaki are typically generated at around P180m, move seaward, and disappear at around P450m. Ruessink and Kroon (1994) proposed a conceptual model for bar behavior, which consists of generation, seaward migration and degeneration of a bar. The bar behavior observed at HORS is consistent with that explained by the conceptual model.

Table 2.1 lists the duration time of the seaward bar migration, the nearshore and the foreshore slopes, the mean wave height and period, and the wave height in storm at Hasaki and three other coasts on the basis of Shand and Bailey (1999) and Shand et al. (1999). The wave height in storm was defined to be the height at which waves are unlikely to exceed the given height at the 99% level, i.e., the nonexceedance probability is 0.99. The statistical values of wave climate were estimated on the basis of the daily-averaged significant wave height.

The duration time of seaward bar crest migration at Hasaki is shorter than that in the Netherlands, and this difference is consistent with the results of Shand et al. (1999). Shand et al. (1999) investigated the relationships between the duration time of the seaward bar crest migration and hydrodynamic and morphological properties, and showed that a long duration time corresponds to a mild nearshore slope. They assumed that a beach with a mild slope would tend to be exposed to high waves, which would generate a large bar that required a long time for seaward migration. An alternative explanation is that if the water depth at which the bar disappears is assumed to be fixed, on a beach with a mild slope, the distance a bar crest must migrate is relatively long; the long distance results in the long duration time. In addition, in the Netherlands, multiple

bars exist, so that low waves that are generated by the energy dissipation on an offshore bar may decrease the seaward bar migration speed, as suggested by Ruessink and Terwindt (2000).

Although the difference between the duration time of the bar crest migration at Hasaki and that in the Netherlands can be explained by the difference in the nearshore slope, the difference between the duration time at Hasaki and those at Duck and Wanganui cannot be explained by the difference in the nearshore slope. According to the nearshore slope, the duration time at Hasaki would be longer than those at Duck and Wanganui. Other factors, such as longshore current, are also likely to affect the duration time (Shand et al., 1999).

The empirical eigenfunction analysis applied to the beach profiles at HORS separated the topography variation in the nearshore from that in the foreshore as shown in Figures 2.8 (1) to (3), whereas these were rarely separated in previous studies (e.g., Winant et al., 1975; Aubrey, 1979; Birkemeier, 1984; Wijnberg and Terwindt, 1995). This separation shows that the beach profile change in the foreshore at HORS was almost independent of the bar movement. Takeda and Sunamura (1992), however, showed that a shoreline with a bar close to it tends to be less retreated than that with a bar at a distance from it. Furthermore, Stive et al. (1996) suggest a strong correlation between bar movement and the foreshore topographic variation. Further field investigations on the relationship between bar movement and the topographic variation in the foreshore are required.

Compared with long-term and medium-term bar crest migrations, the sediment movements associated with the bar crest migrations have rarely been investigated. Investigations described in section 2.4.2 revealed that the cross-shore distribution of the low frequency component of the cross-shore sediment transport rate at Hasaki consisted of seaward sediment transport on and around bar crests and shoreward sediment transport in trough regions; the seaward sediment transport induced the medium-term seaward bar crest migration, and the shoreward sediment transport contributed to the next bar generation. This result is consistent with that for short-term sediment movement shown by Aagaard and Greenwood (1999). They showed on the basis of field data that seaward sediment transport is induced by a large wave height-water depth ratio, whereas shoreward sediment transport is induced by a relatively large water depth. On and around a bar crest, waves tend to break and hence the wave height-water depth

tends to be large. In a trough, the water depth is relatively large. Therefore their result suggests that seaward sediment transport is likely to occur on and around bar crests and that shoreward sediment transport is likely to occur in trough regions.

A model for medium-term bar movement proposed by Ruessink and Terwindt (2000) is based on the wave height-water depth ratio, where a large ratio results in seaward sediment movement and a small ratio results in shoreward sediment movement. Hence, although their model could not explain a bar generation on a Dutch coast, it may explain medium-term sediment transport and bar crest migration observed at Hasaki.

Short-term sediment transport on a barred beach was also investigated by Thornton et al. (1996). They estimated cross-shore sediment transport rates with the Bowen (1980)/Bailard (1982) model using cross-shore and longshore current velocities measured in the field. Under a storm condition, seaward sediment transport was observed on and around a bar crest and shoreward sediment transport was observed in a trough region. This result is also consistent with the sediment movement at Hasaki

2.6 Conclusions

The beach profile data obtained from the foot of a dune to a water depth of about 5 m at HORS showed that bar crests migrated seaward with a period of a year. The duration time of the migration, which is almost equal to the return period, is shorter than those observed on coasts in the United States, the Netherlands, and New Zealand. The difference between the duration time at HORS and that in the Netherlands can be explained by the difference in the nearshore slope as shown by Shand et al. (1999). However, the difference between the duration time at HORS and those in the United States and New Zealand cannot be explained by the difference in the slope.

Although the bar crest migrated almost exclusively in a seaward direction, the cross-shore sediment transport associated with the bar crest migration fluctuated seaward and shoreward. Seaward sediment transport occurred on and around bar crests and induced the seaward migration of the bar crests, whereas shoreward sediment transport occurred in trough regions and contributed to the generation of the next bars.

The cross-shore sediment transport rate increased from P150m to P250m, had a peak at P250m, and then gradually decreased seaward. This cross-shore distribution induced the development and decay of the bar; the bar developed from P180m to P250m, and

decayed from P250m to P380m.

In the region around P250m, where the sediment transport rate was large and the bar was most developed, the bar crest moved seaward and the seaward sediment movement primarily occurred from winter to spring. The sediment transport rate and the beach profile change were small in summer, but were greater in autumn owing to the increased shoreward sediment transport rate and trough migration.

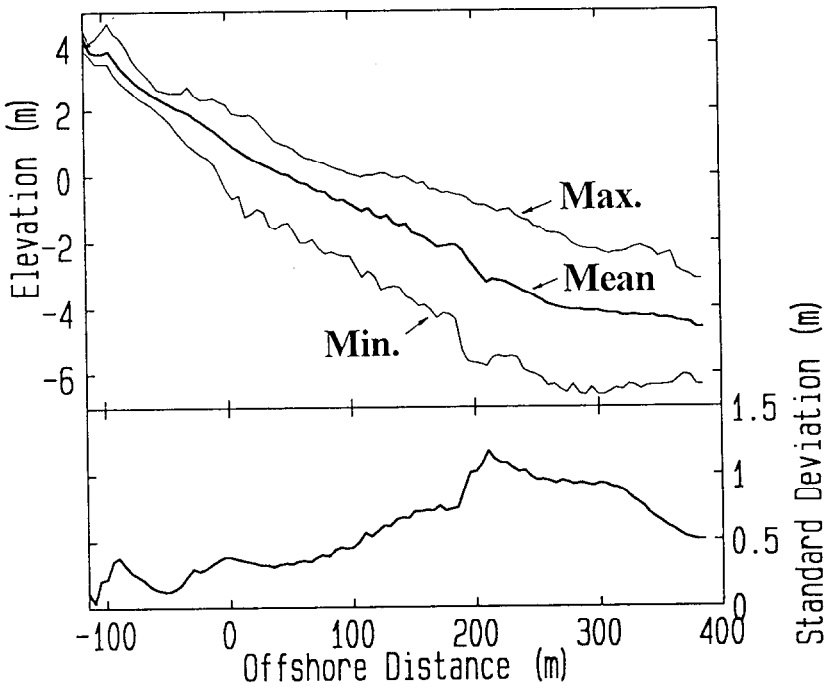

Figure 2.1 Mean beach profile, maximum and minimum elevations, and standard deviation in elevation at HORS.

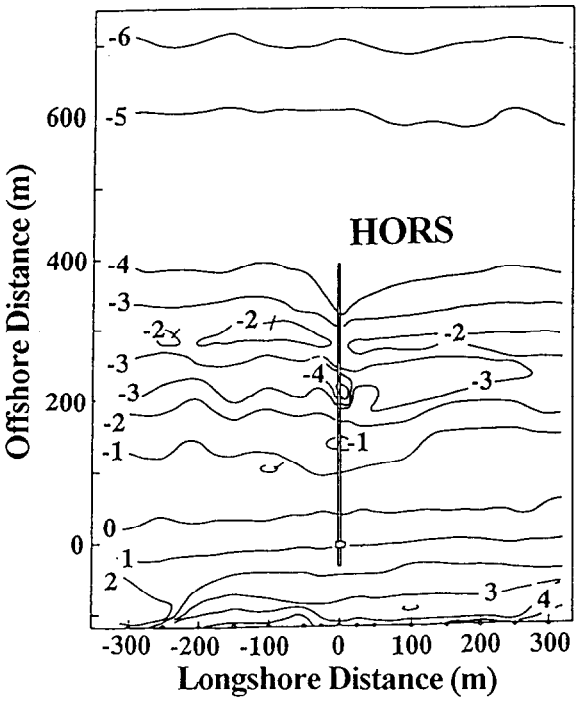

Figure 2.2 An example of the topography near HORS, which was surveyed on March 31, 1989.

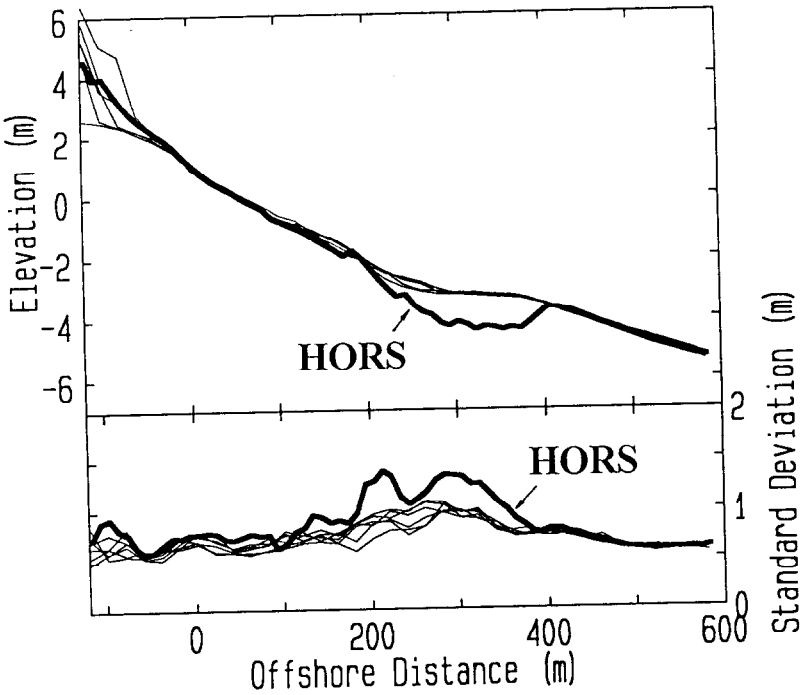

Figure 2.3 Mean beach profiles and standard deviations in elevation estimated along HORS and along six survey lines. Three of the six lines are located north of HORS, and the others are located south of HORS. The alongshore distances between the survey lines and HORS range from 200 m to 300 m. Thick lines show the values along HORS.

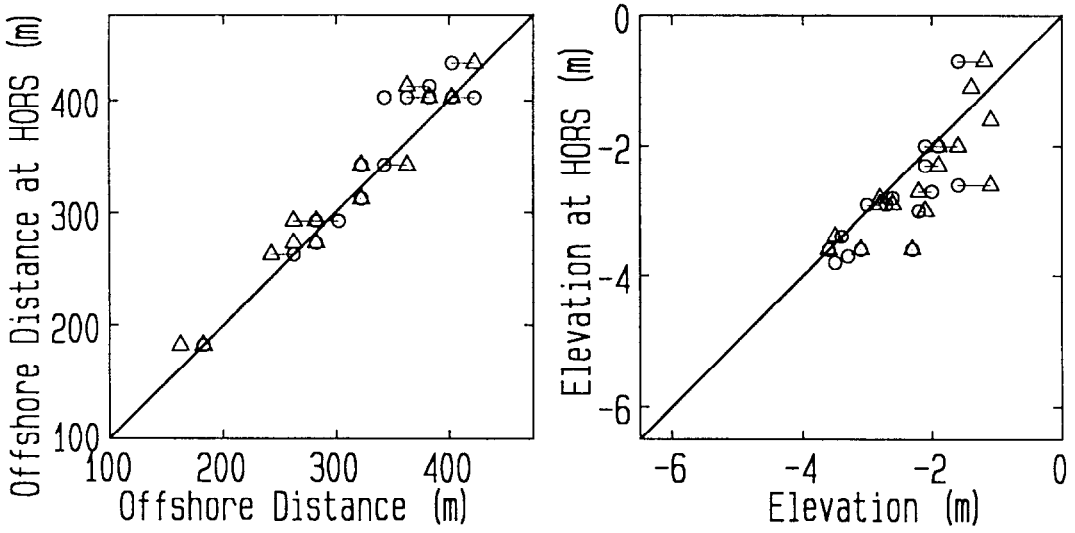

Figure 2.4 (1) Locations and elevations of the bar crests. Open circles and triangles show the values in the northern and the southern regions, respectively.

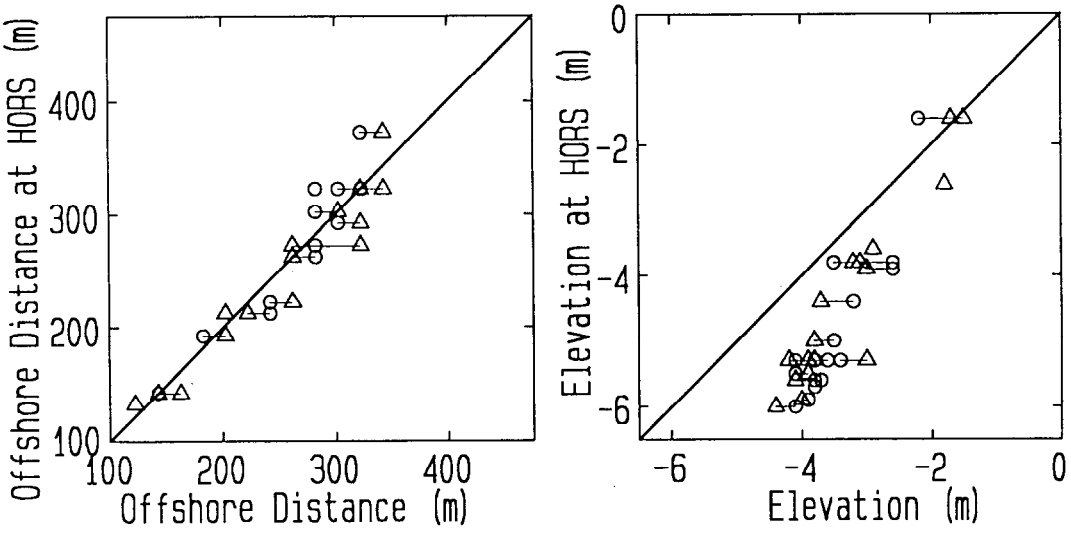

Figure 2.4 (2) Locations and elevations of the troughs. (Details are as in Figure 2.4 (1).)

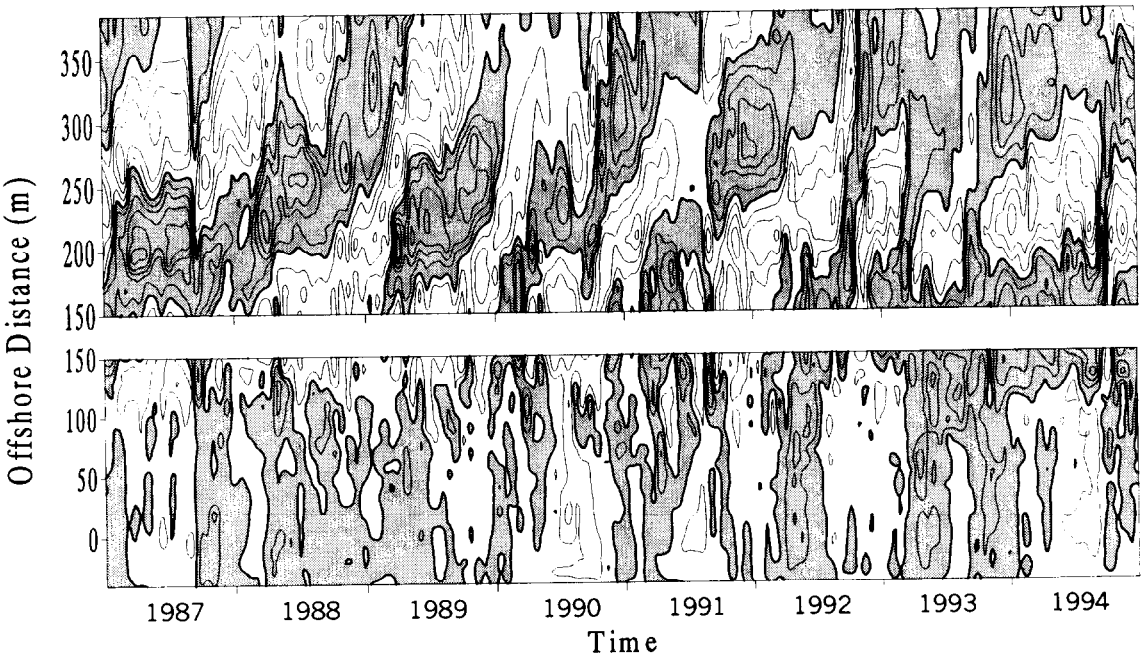

Figure 2.5 Variation from the mean beach profile at HORS. The areas of accumulation and erosion are shown by white and gray colors, respectively. The contour interval is 0.5 m.

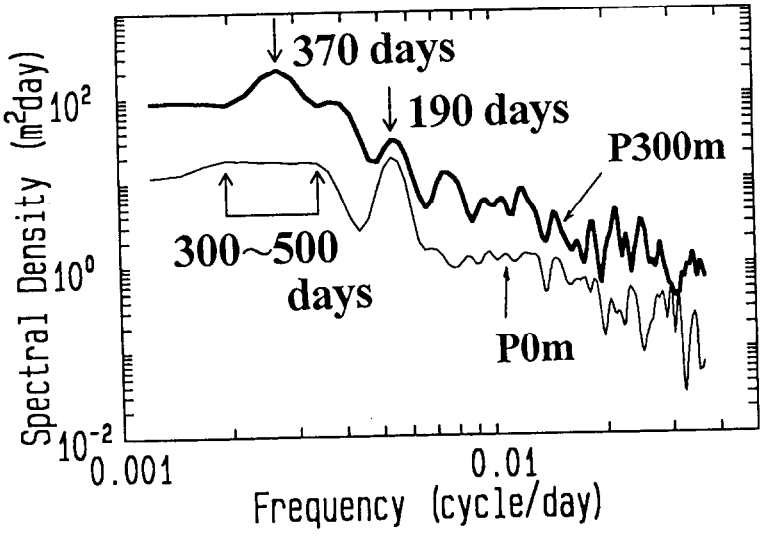

Figure 2.6 Power spectra of elevations at P0m and P300m.

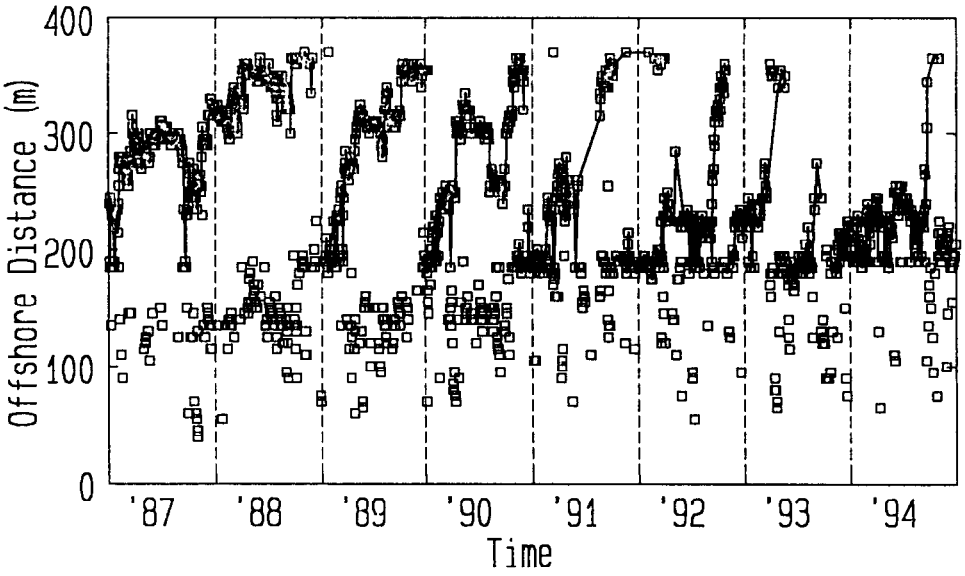

Figure 2.7 Bar crest migration over time.

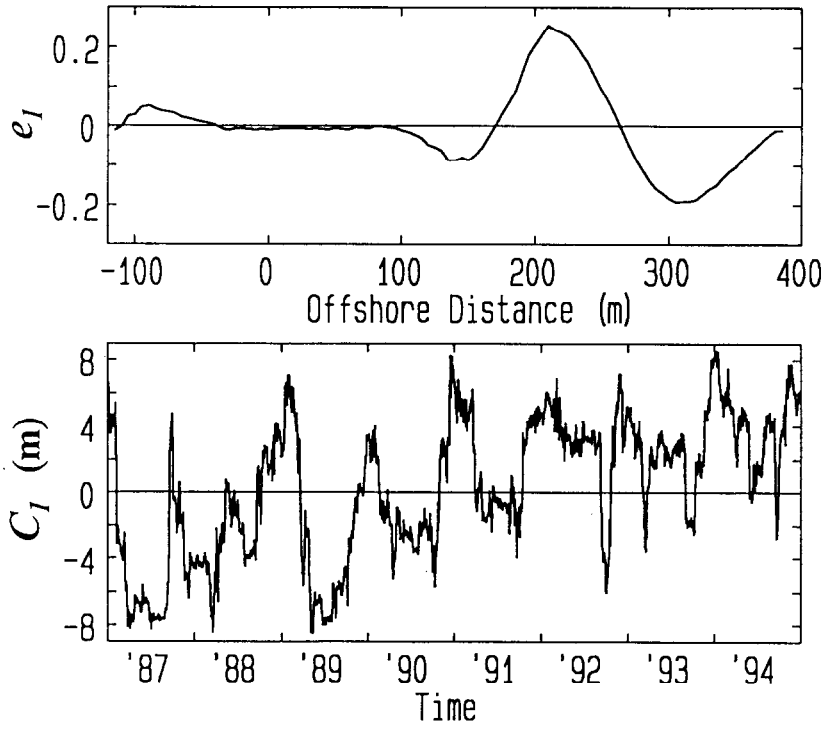

Figure 2.8 (1) The first eigenfunction, e_1 and its temporal weighting, C_1.

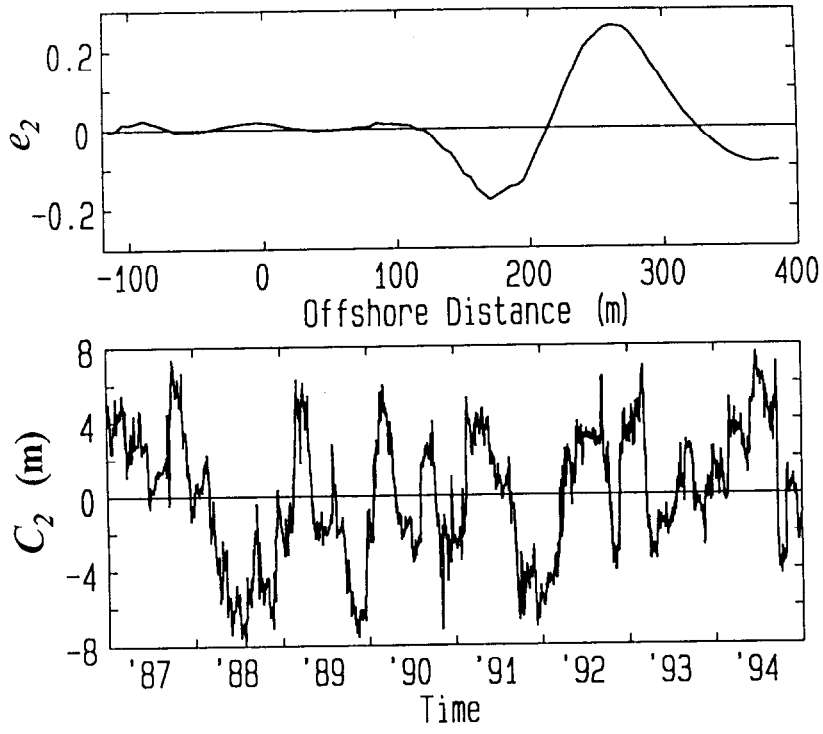

Figure 2.8 (2) The second eigenfunction, e_2 and its temporal weighting, C_2.

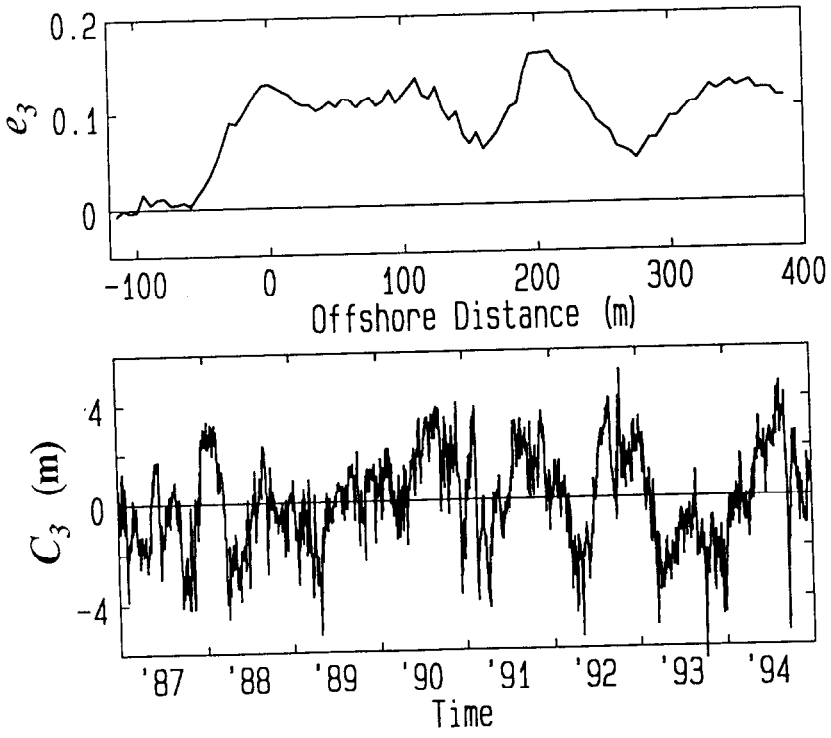

Figure 2.8 (3) The third eigenfunction, e_3 and its temporal weighting, C_3.

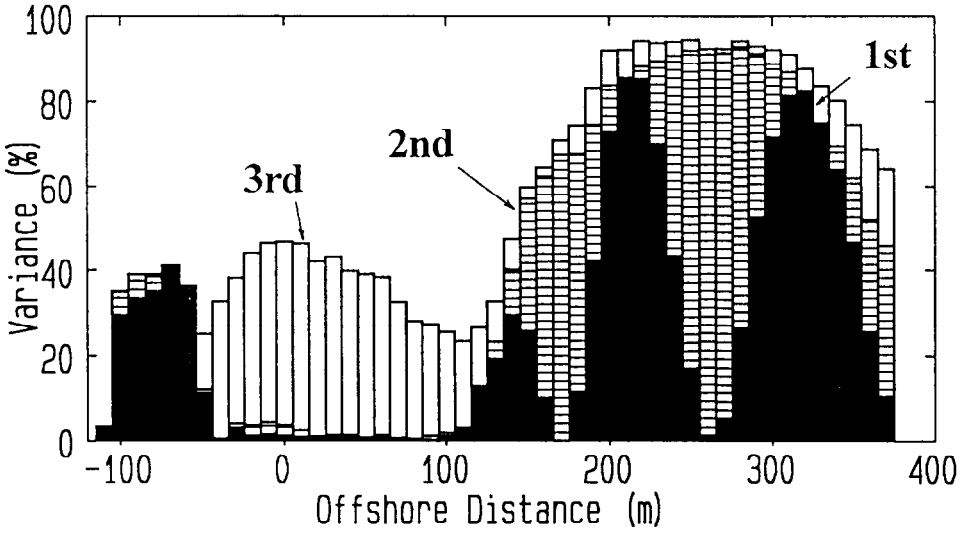

Figure 2.9 Variance at each location explained by the first three eigenfunctions.

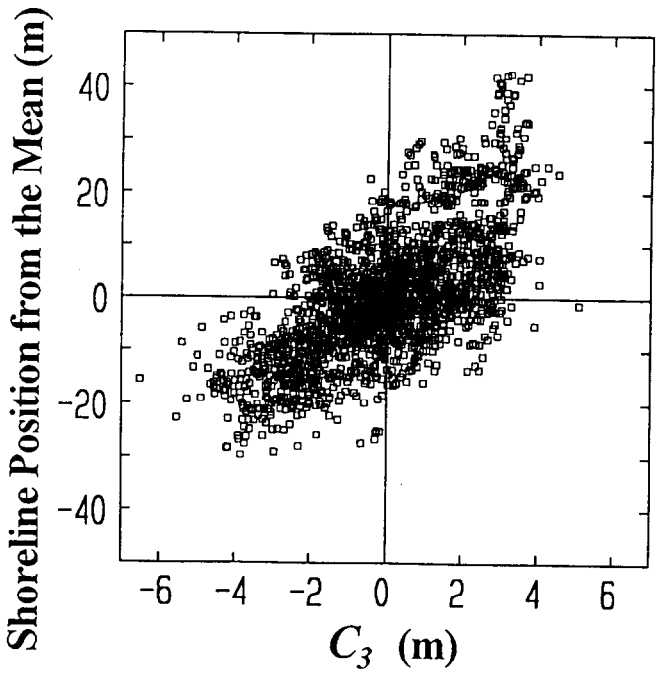

Figure 2.10 Relationship between C_3 and the shoreline position from the mean.

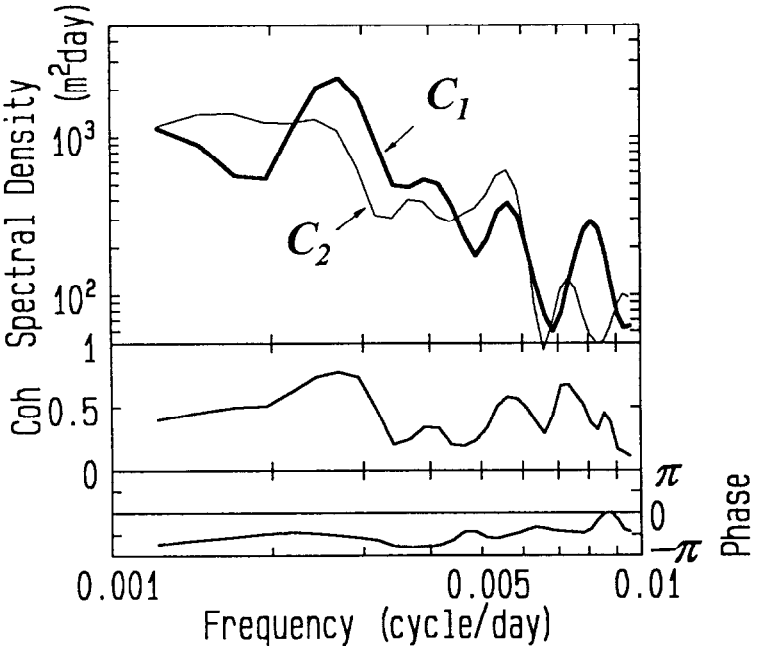

Figure 2.11 Cross spectra between C_1 and C_2.

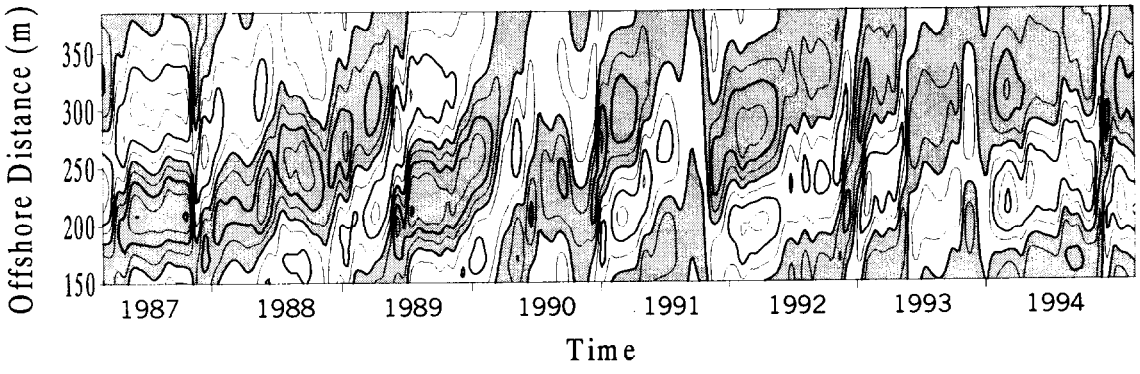

Figure 2.12 Beach profile change at HORS reconstructed by the first two eigenfunctions. The areas of accumulation and erosion are shown by white and gray colors, respectively. The intervals of the thin contour lines and thick contour lines are 0.5 m and 1 m.

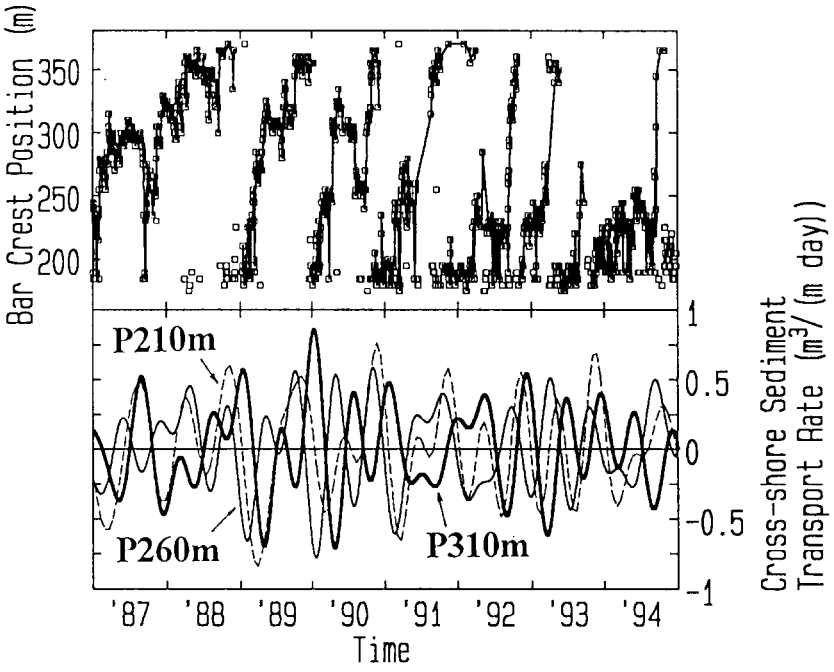

Figure 2.13 Low frequency components of cross-shore sediment transport rates and bar crest migration.

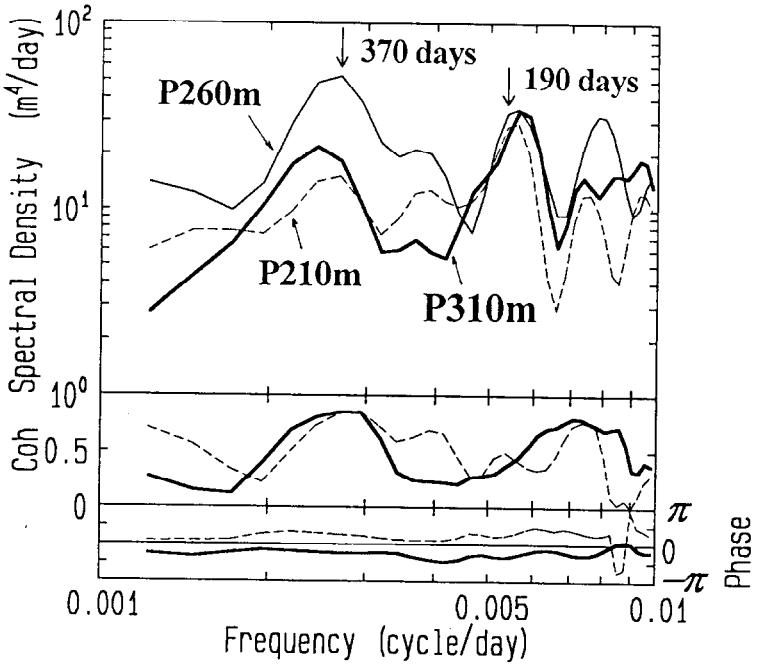

Figure 2.14 Cross spectra between the cross-shore sediment transport rates at P210m and P260m, and those between the rates at P260m and P310m. The thin broken lines in the middle and lower panels show the result between the transport rates at P210m and P260m, and the thick solid lines show that between the transport rates at P260m and P310m.

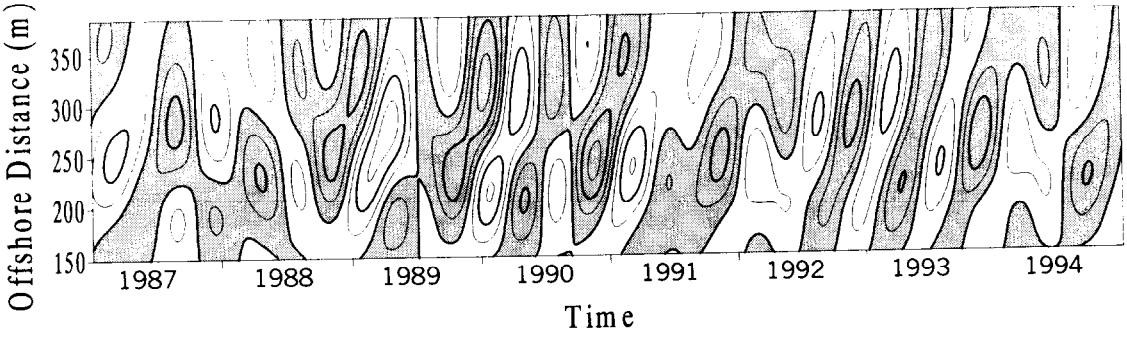

Figure 2.15 Low frequency component of the cross-shore sediment transport rate. The seaward and the shoreward sediment transport rates are shown by white and gray colors, respectively. The intervals of the thin contour lines and thick contour lines are 0.25 m^3/m/day and 0.5 m^3/m/day, respectively.

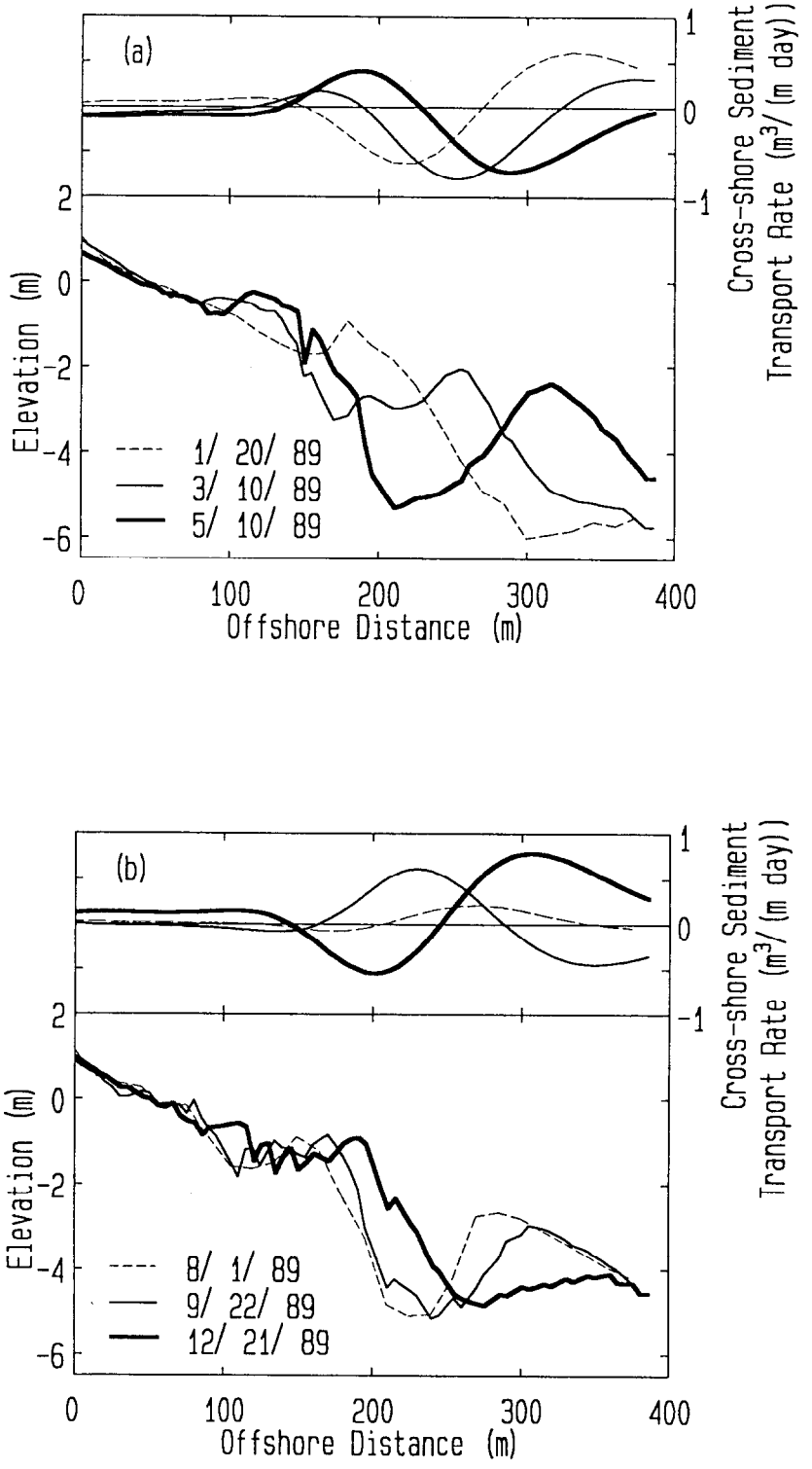

Figure 2.16 Beach profiles and cross-shore distributions of the low frequency component of the cross-shore sediment transport rate during (a) the first half of the seaward bar crest migration and (b) the second half.

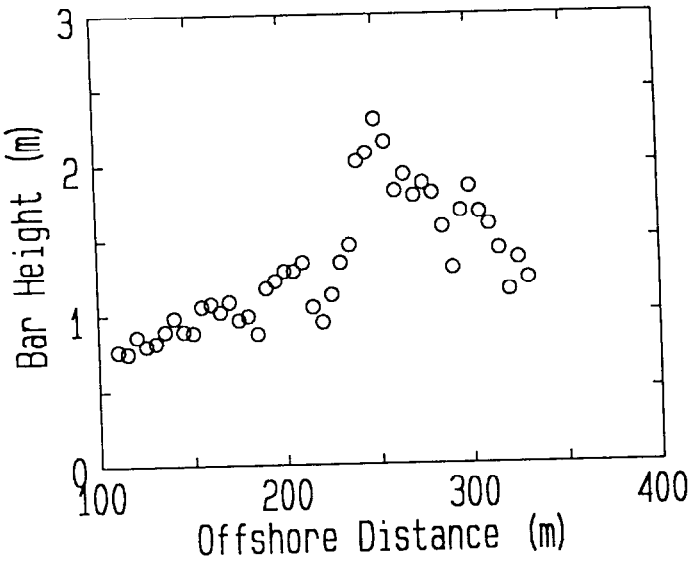

Figure 2.17 Cross-shore distribution of bar height.

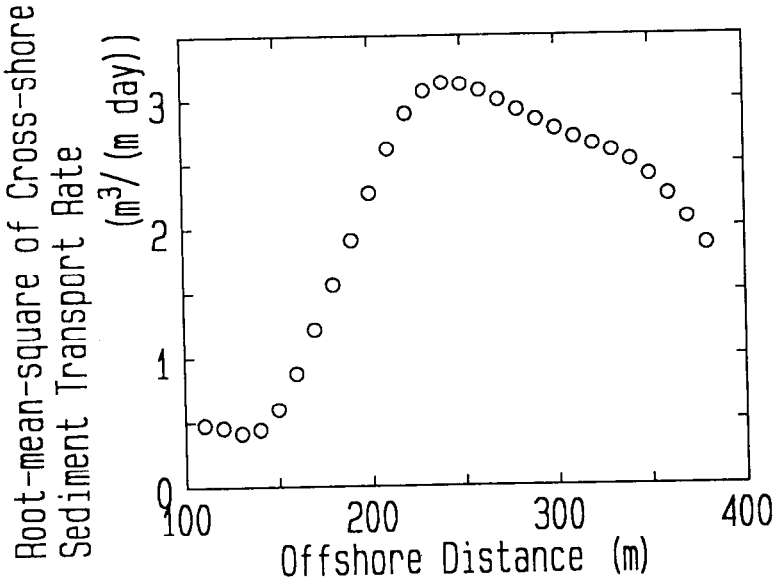

Figure 2.18 Cross-shore distribution of root-mean-square value of cross-shore sediment transport rate.

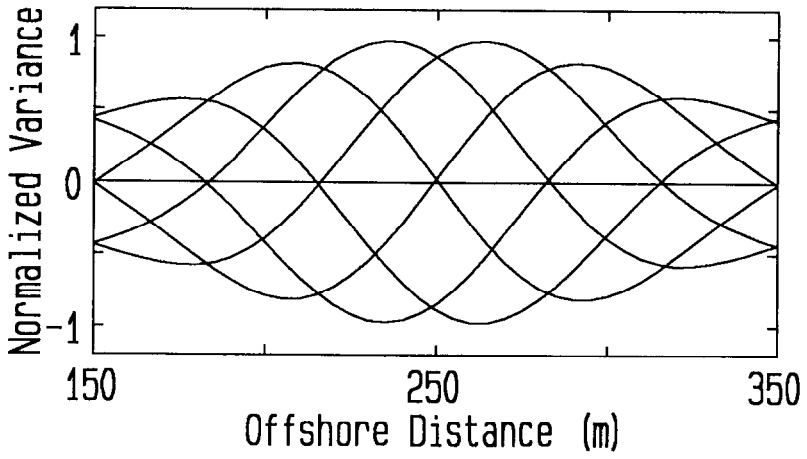

Figure 2.19 Beach profiles estimated with Eq. (2.3).

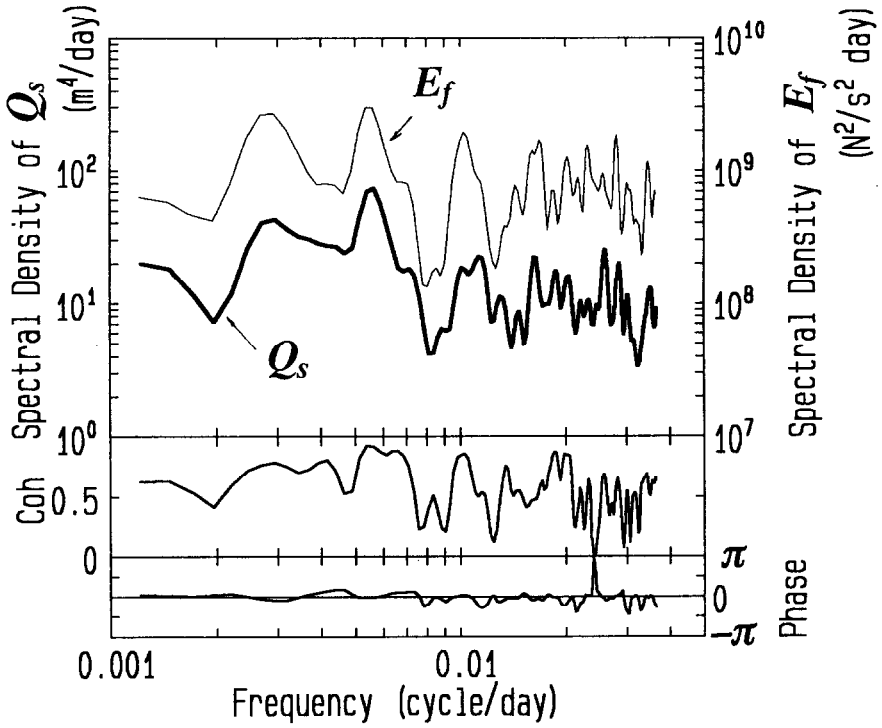

Figure 2.20 Cross spectra between $Q_s(t)$ and E_f.

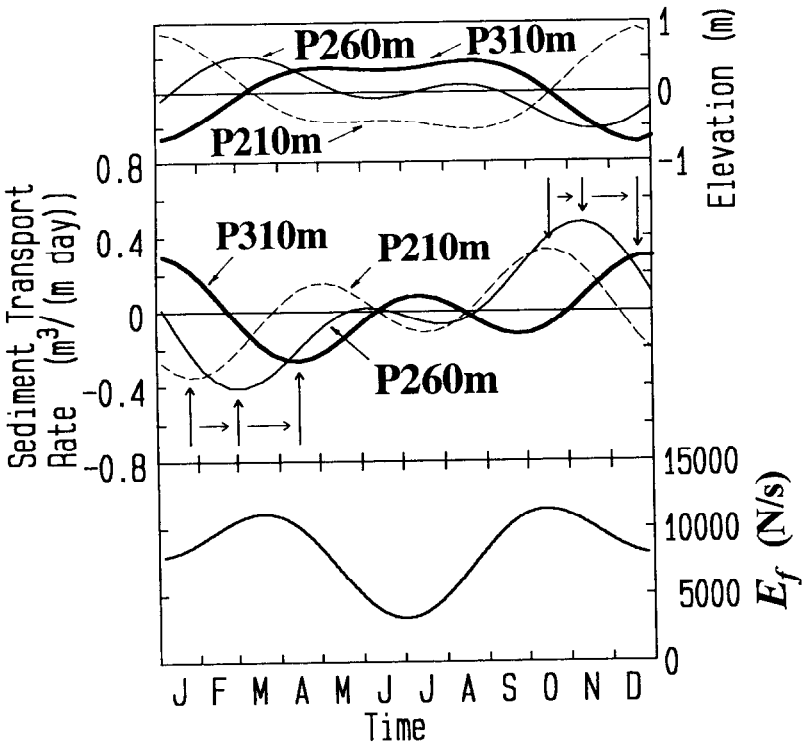

Figure 2.21 Seasonal variations in the low frequency components of the sediment transport rates at P210m, P260m and P310m (the middle panel), and E_f (the lower panel) as well as those in the elevations at the points (the upper panel); the shoreward sediment transport is defined to be positive.

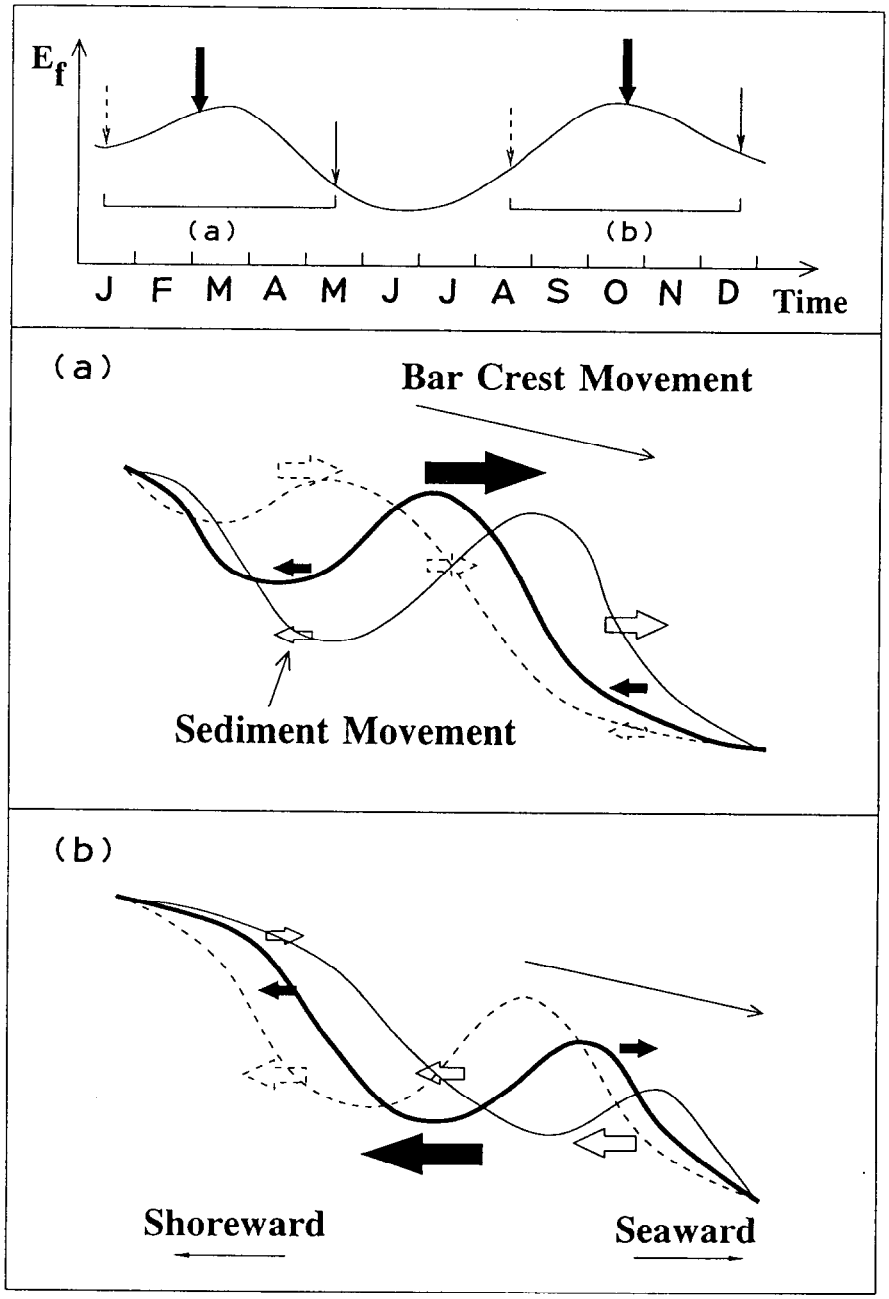

Figure 2.22 Schematic diagram showing the bar crest migration and the sediment movement at Hasaki.

Table 2.1 Duration time of bar crest migration, and morphological and wave characteristics

Location	Duration Time (year)	Nearshore Slope	Foreshore Slope	Mean Wave Height (m)	Mean Wave Period (s)	Wave Height in Storm (m)
The Netherlands	6 ~20	0.004~ 0.008	0.015~ 0.02	1.35	6.0	4.1~4.3
Duck, USA	4	0.0097	0.052~ 0.060	1.10	6.4	3.05
Wanganui, New Zealand	2 ~ 5	0.0083~ 0.0092	0.029~ 0.031	1.20	7.8	3.20
Hasaki, Japan	1	0.008	0.02	1.37	8.0	4.36

3. Field measurements and modeling of wave height and the fraction of breaking waves

3.1 Introduction

Various phenomena in the nearshore zone such as nearshore currents, sediment suspension, and morphological variation are caused by turbulence, mass flux and momentum flux. Those phenomena induced by breaking waves are much greater than those induced by non-breaking waves. Hence, to predict longshore current and undertow velocities, suspended sediment concentrations and topographic variations, it is essential to accurately estimate the conditions for wave breaking and wave reforming.

Several models have been proposed to estimate wave height H and the fraction of breaking waves Q_b, which is the ratio of the number of breaking waves to the total number of waves. Battjes and Janssen (1978) simulated variations in H within the surf zone, assuming a modified Rayleigh distribution truncated at the breaking wave height H_b, where breaking waves all have the same value of H_b. They estimated the time-averaged dissipation rate of wave energy by a periodic bore model incorporating H_b and Q_b; the value of Q_b was estimated by

$$\frac{1-Q_b}{-\ln Q_b} = \left(\frac{H_{rms}}{H_b} \right)^2, \tag{3.1}$$

where H_{rms} is the root-mean-square wave height.

Battjes and Stive (1985), Roelvink (1993) and Southgate and Nairn (1993) compared Q_b estimated by Eq. (3.1) with results of field measurements and experiments on planar beaches. Although the estimated values of Q_b were comparatively smaller than the measured values, the estimated cross-shore distributions of Q_b qualitatively agreed with those measured.

Thornton and Guza (1983) improved Battjes and Janssen's (1978) model by assuming an unmodified Rayleigh distribution, which is not truncated at the breaking wave height, at any location inside and outside the surf zone, and that wave breaking occurs at any wave height with a probability of $P_b(H)$. The time-averaged dissipation rate of wave energy was estimated by another periodic bore model, in which one equation is slightly different from that in Battjes and Janssen's (1978) model. The value of Q_b was estimated using Eq. (3.2) with a weighting function $W(H)$ and the Rayleigh wave height probability density function $p(H)$.

$$Q_b = \int_0^\infty P_b(H)dH,\ \ P_b(H) = W(H)p(H),$$
$$W(H) = \left(\frac{H_{rms}}{\gamma h}\right)^2\left[1-\exp\left\{-\left(\frac{H}{\gamma h}\right)^2\right\}\right],\ \gamma = 0.42, \tag{3.2}$$
$$p(H) = \frac{2H}{H_{rms}^2}\exp\left[-\left(\frac{H}{H_{rms}}\right)^2\right].$$

They measured Q_b on a planar beach in the field, and found that Q_b calculated from Eq. (3.2) agreed well with the measured values.

Dally (1992) simulated variations in wave height by applying another algorithm, a wave-by-wave approach, where the shoaling, breaking and reforming of an individual wave are calculated. Because the mode of wave breaking, i.e., breaking or non-breaking, of an individual wave is clarified at any point through the calculation for the individual wave, Q_b can be directly estimated as the ratio of the number of breaking waves to the total number of waves. By comparing calculated results with those measured on a longshore bar in the field by Ebersole (1987), Dally (1992) showed that Q_b calculated at the seaward slope of the bar correlated well with measured values, though the calculated values were comparatively smaller than the measured values. He hypothesized that this underestimation was due to seaward winds.

Southgate and Wallace (1994) introduced the "persistence length" into Battjes and Janssen's (1978) model. Beyond the persistence length, a breaking wave reforms regardless of the wave condition. This length was assumed to be proportional to H_b, and the proportional coefficient was determined so that the model results fitted the values of Q_b measured in large-scale experiments.

The models reviewed above provide good quantitative or at least qualitative predictions of the cross-shore distributions of Q_b on planar beaches and on the seaward slopes of longshore bars. However, the models could not even qualitatively predict the distributions of Q_b at troughs. Rivero et al. (1994) as well as Southgate and Nairn (1993) compared Q_b estimated by Battjes and Janssen's (1978) model with those measured in experiments, and showed that Battjes and Janssen's (1978) model considerably underestimated Q_b at troughs. Dally's (1992) model also significantly underestimated Q_b at troughs (Dally, 1992; Nishi, 1994). Although use of the "persistence length" improved the accuracy of determining Q_b at a trough (Southgate

and Wallace, 1994), the application of their model is thought to be limited because the coefficient for calculating the persistence length was determined without physical basis; i.e., the persistence length itself was not investigated. Consequently, development of a more reliable model requires more emphasis to be directed at investigating wave reforming and the associated fraction of breaking waves at a trough.

The conditions for wave reforming on flat beds were investigated by Dally et al. (1985) as well as Kweon and Goda (1994). They defined "the stable wave height" the wave height at which wave energy dissipation ceases. This definition of wave stabilization is almost identical to that of wave reforming. The investigation of Dally et al. (1985) is based on the experiment conducted by Horikawa and Kuo (1966), and that of Kweon and Goda (1994) is based on their own experiment. Both of Horikawa and Kuo (1966), and Kweon and Goda (1994) conducted experiments of wave decay on shelf beaches with upward sloping bottoms and flat bottoms. The criterion for the stable wave height H_s obtained by Dally et al. (1985) and that by Kweon and Goda (1994) are expressed as

$$H_s/h_s = 0.4, \tag{3.3}$$

and

$$H_s/h_s = 0.128(h_s/L_0)^{-1}\left[1-\exp(-1.5\pi h_s/L_0)\right], \tag{3.4}$$

where h_s is the water depth at which the wave height reaches H_s, and L_0 is the offshore wavelength.

Because the validity of these criteria is not clear from the field evidence, field measurements of wave breaking and wave reforming were performed over longshore bars and troughs at HORS, and the conditions for wave reforming were investigated. Then, on the basis of the conditions for wave reforming, a model for wave height and the fraction of breaking waves was developed and verified with field and large-scale experimental data.

3.2 Field measurements and analysis

3.2.1 Field measurements

Field measurements for investigations on wave reforming and the variations in H and Q_b over longshore bars and troughs were conducted during the period from March 1, 1994 to January 31, 1995. Figure 3.1 shows the mean beach profile during this period;

the short vertical lines on the mean beach profile show the standard deviations in elevation. From March 1994 to January 1995, bars frequently formed around P200m and troughs formed around P160m.

Water surface elevations and modes of wave breaking of individual waves (breaking or non-breaking) were simultaneously measured for 20 minutes at two points located over a longshore bar and trough. Water surface elevations were measured at a sampling frequency of 2 Hz with ultrasonic wave gages installed on a side of the HORS pier deck. Modes of wave breaking were visually observed. When foam was observed on a wave crest, the wave was judged to be a breaking wave, and a pulse signal was manually input; the pulse signal was recorded with corresponding water surface elevation data. When a pulse signal is included in the data set of a wave, the wave is judged as a breaking wave.

The variations in H and Q_b over longshore bars were obtained by three sets of the measurements taken at different locations. Corresponding wind speeds and directions were also measured with an anemometer installed at the tip of HORS (P385m).

3.2.2 Data analysis

For investigating the conditions for wave reforming, the following parameters were required: individual wave height H_r and period T_r, and water depth h_r at wave reforming. These data, however, are very difficult to directly obtain in the field, and hence these values were estimated using the data from waves that are breaking at the seaward measurement points and non-breaking at the shoreward measurement points. For this procedure, it is essential to collect the sea/shoreward data from the same wave. This was accomplished by first extracting a sequence of water surface elevations of a wave measured at a seaward point, and then extracting such elevations measured at the shoreward point of what is thought to be the same wave. Next, a correlation coefficient between the seaward and shoreward extracted data sets was calculated. If the calculated correlation coefficient was greater than 0.85, the data sets were judged to belong to the same wave. A detailed description of this procedure is shown in the appendix.

3.3 Wave condition at wave reforming

Eleven measurements with maximum Q_b greater than 0.4 were chosen for the

investigation of the conditions for wave reforming. Table 3.1 lists the corresponding wave and wind conditions: the significant wave heights in deep water $(H_{1/3})_0$, the significant wave periods in deep water $(T_{1/3})_0$, the wave directions visually observed at bar crests θ_b, and the cross-shore and longshore wind velocities, W_c and W_l.

The data sets of waves that were breaking at seaward points and non-breaking at shoreward points were analyzed. The values of H_r and h_r are estimated as the means of the values at the seaward and shoreward points, and L_0 is estimated using the mean of the wave periods at the seaward and shoreward points. In estimating h_r, the time-averaged water level of the low frequency components is considered.

Figure 3.2 shows H_r/h_r against h_r/L_0. The mean value of H_r/h_r in the measurements was 0.35 (thick broken line), and the standard deviation was 0.09. As shown in the figure, the value of H_r/h_r is weakly correlated with the logarithmic value of h_r/L_0 (r=-0.48). The correlation obtained by the least squares method (thick solid line) is expressed as

$$H_r/h_r = -0.0624\ln(h_r/L_0) + 0.142. \tag{3.5}$$

The root-mean-square value of the difference between H_r/h_r that were measured and those estimated with Eq. (3.5) was 0.08.

The thin dash-dotted line and the thin dashed line are the experimentally determined criterion for wave stabilization proposed by Dally et al. (1985), expressed by Eq. (3.3), and that proposed by Kweon and Goda (1994), expressed by Eq. (3.4), respectively. Most H_r/h_r in the field were smaller than the experimentally obtained criteria on H_s/h_s.

Although the relationship between H_r/h_r and cross-shore wind speed was also examined, the correlation was very weak (r=0.15).

3.4 Model for wave height and the fraction of breaking waves

3.4.1 Formulation of model

A model developed here for predicting wave height and the fraction of breaking waves employs a wave-by-wave approach as proposed by Dally (1992); the shoaling, breaking and reforming of individual waves are calculated. The values of significant wave height $H_{1/3}$ and Q_b are estimated with the simulation results of individual waves.

Shoaling of a wave is calculated with the shoaling coefficient proposed by Shuto (1974), which considers wave nonlinearity.

As a criterion for wave breaking, a formula proposed by Seyama and Kimura (1988), who modified Goda's formula (1970), was adopted. They experimentally investigated the wave height-water depth ratio at wave breaking H_b/h_b for individual irregular waves as a function of: (1) the beach slope $\tan\beta$, and (2) the ratio of breaking water depth to the offshore wavelength h_b/L_0. The relation between H_b/h_b versus $\tan\beta$ and h_b/L_0, and the standard deviation δ of H_b/h_b are expressed as

$$\frac{H_b}{h_b} = 0.16\frac{L_0}{h_b}\left[1-\exp\left\{-0.8\pi\frac{h_b}{L_0}\left(1+15\tan^{4/3}\beta\right)\right\}\right] - 0.96\tan\beta + 0.2, \tag{3.6}$$

and

$$\delta = 0.08 H_b/h_b. \tag{3.7}$$

In the model, the values of H_b/h_b are assumed to distribute around Eq. (3.6) with a normal distribution having the standard deviation estimated by Eq. (3.7).

After wave breaking, the energy dissipation of a wave is estimated; the calculation of the wave energy dissipation is explained later.

Wave reforming is evaluated using two criteria: one is H_r/h_r=0.35 and the other is Eq. (3.5). With consideration of the scatter in the data shown in Figure 3.2, H_r/h_r is assumed to distribute around the criteria with a normal distribution. After wave reforming, wave shoaling is calculated again naturally.

The energy dissipation of a wave is evaluated with a periodic bore dissipation sub-model used by Thornton and Guza (1983). The sub-model is expressed as

$$\frac{\partial\left(E_w C_g\right)}{\partial x} = \frac{1}{4}\rho g f\frac{(BH)^3}{h}, \tag{3.8}$$

where E_w is the wave energy, C_g is the group velocity, f is the frequency, ρ is the density of sea water, g is the acceleration of gravity, and B is a dimensionless coefficient.

Thornton and Guza (1983) used Eq. (3.8) to calculate the total wave energy dissipation applying the same value of B to all waves, which have different wave heights. By comparing H_{rms} measured in the field and those estimated by Eq. (3.8), they determined B = 1.5. In the present model, however, variations in H of individual waves are predicted; for individual waves, B = 1.5 has not been proven to be the optimum value. The optimum B value for individual waves was therefore investigated with experimental results reported by Seyama and Kimura (1988).

Seyama and Kimura (1988) experimentally investigated variations in H of individual waves in the surf zone, and showed that the variations consist of three phases: an increase in H immediately after wave breaking, a sharp decrease in H after reaching the maximum and a moderate decrease in H from the middle of the surf zone to the shoreline. The corresponding formulae representing these phases, proposed by Seyama and Kimura (1988), are utilized for obtaining the optimum B value. However, because Seyama and Kimura (1988) defined wave breaking differently than its definition in the present model, where wave breaking point is defined as the point where the maximum wave height occurs, their formulae were slightly modified so that the maximum wave height occurs at the wave breaking point. The modified formula is given by

$$\begin{aligned} H/H_b &= \alpha_1(h/h_b)+\alpha_2, \quad h/h_b \geq \alpha_3, \\ H/H_b &= \alpha_4(h/h_b)+\alpha_5, \quad h/h_b < \alpha_3, \end{aligned} \tag{3.9}$$

where h is the water depth, and h_b is the water depth at wave breaking. The values of coefficients α_1 to α_5 are listed in Table 3.2.

The optimum B value was obtained so that the wave heights estimated by Eq. (3.8) for four waves (H_0/L_0=0.005, 0.01, 0.025 and 0.05) on four beach slopes ($\tan\beta$ =1/10, 1/20, 1/30, and 1/50) agree with those estimated by Eq. (3.9). The optimum B value obtained is

$$B = 1.6 - 0.12\ln(H_0/L_0) + 0.28\ln(\tan\beta). \tag{3.10}$$

Figure 3.3 shows examples of wave heights estimated by Eq. (3.9) and by Eq. (3.8) with the optimum B (Eq. (3.10)). The thick solid lines show the wave heights estimated by Eq. (3.9), and the thin solid lines and the dashed lines show those estimated by Eq. (3.8) at H_0/L_0=0.005 and 0.07, respectively. Note that the present model accurately predicts variation in H on planar beaches.

The model is also verified against experimental data of wave decay on a flat bed (Kweon and Goda, 1994). Figure 3.4 shows comparisons of wave heights estimated by Eq. (3.8) and those measured at H_0/L_0 from 0.006 to 0.07; the closed circles are the measured values and the solid lines are the estimated values. Although there are some discrepancies, the model is suitable for predicting the wave decay on a flat bed.

3.4.2 Comparison with measurements

(1) HORS

The model was compared with the eleven measurements at HORS; the conditions of the measurements are listed in Table 3.1. The input wave data at the offshore boundaries are the wave heights and periods of individual waves, which are estimated from the wave data obtained at the boundaries. The offshore boundaries are set at the most seaward measurement points, which are P320m in Cases 1 and 2, P380m in Cases 3 – 8, and P230m in Cases 9 – 11. Supplementary simple visual observations confirmed that the offshore boundaries were not included in the surf zones, and therefore all individual waves at the offshore boundaries are set as non-breaking.

Figure 3.5 shows comparisons of $H_{1/3}$ and Q_b for six out of eleven cases, when the wave heights were large. The solid circles show $H_{1/3}$ measured in the field, and the thick solid line and the thick dashed line show those estimated by the model with Eq. (3.5) and with H_r/h_r=0.35, respectively. The thin solid line shows the values estimated with a dissipation sub-model proposed by Dally et al. (1985) instead of Eq. (3.8). The sub-model is expressed as

$$\frac{\partial(E_w C_g)}{\partial x} = (E_w C_g - E_s C_g)\frac{K}{h}, \qquad (3.11)$$
$$E_s = \rho g H_s^2/8, \quad H_s = \Gamma h,$$

where K and Γ are dimensionless coefficients. Dally et al. (1985) showed that use of K=0.15 and Γ=0.4 provide estimates of H that are in good agreement with experimental data reported by Horikawa and Kuo (1966).

The thin dashed line shows H_{rms} and Q_b estimated with the model proposed by Thornton and Guza (1983), and the open circles represent measured values of H_{rms}.

There are only small differences between $H_{1/3}$ and Q_b predicted by the present model using H_r/h_r=0.35 and those using Eq. (3.5). There is close agreement between the results from the models and the measured values although the predicted values are smaller than the measured values at troughs.

The values of $H_{1/3}$ predicted with the sub-model of Dally et al. (1985) are almost equal to those predicted by the present model with H_r/h_r=0.35, whereas Q_b at troughs predicted with the sub-model of Dally et al. (1985) are naturally smaller than those predicted by the present model.

The values of H_{rms} and Q_b predicted by Thornton and Guza's (1983) model are smaller than those measured.

(2) Delta Flume

The model for predicting wave height and the fraction of breaking waves was next compared with large-scale experimental data of the Delta Flume '93 Experiments (Rivero et al., 1994). The data shown by Rivero et al. (1994) are Q_b and H_{m0}, defined as

$$H_{m0} = 4.004\eta_{rms}. \tag{3.12}$$

The present model cannot predict H_{m0} because H_{m0} is estimated from a series of water surface elevation, which the present model cannot predict. For comparing the present model with the large-scale experiments, an assumption was required regarding the relationship between the root-mean-square value of water surface elevation η_{rms} and $H_{1/3}$.

Using field data outside the surf zone, Goda (1983) has investigated the relationship between $H_{1/3}/\eta_{rms}$ and a wave nonlinearity parameter $\Pi_{1/3}$, which is defined as

$$\Pi_{1/3} = \frac{H_{1/3}}{L}\left(\tanh\frac{2\pi h}{L}\right)^{-3}, \tag{3.13}$$

where L is the wavelength at a water depth of h. Goda (1983) reported that $H_{1/3}/\eta_{rms}$ increases with the increase of $\Pi_{1/3}$ when $\Pi_{1/3} \geqq 0.1$, whereas $H_{1/3}/\eta_{rms}$ is constant and about equal to 3.8 when $\Pi_{1/3} < 0.1$.

Although the relationship between $H_{1/3}$ and η_{rms} outside the surf zone was investigated, no relationship between $H_{1/3}$ and η_{rms} in the surf zone was reported. Hence, the relationship was investigated with the field data from the eleven cases. The relationship is shown in Figure 3.6, where the solid line shows the relationship obtained with the method of least squares, and the dashed line shows $H_{1/3}/\eta_{rms}=3.8$. The value of $H_{1/3}/\eta_{rms}$ in the surf zone increases with the increase of $\Pi_{1/3}$ when $\Pi_{1/3} \geqq 0.1$, whereas $H_{1/3}/\eta_{rms}$ is about 3.8 when $\Pi_{1/3} < 0.1$. The relation is expressed as

$$\begin{aligned} H_{1/3}/\eta_{rms} &= 0.349\ln\Pi_{1/3} + 4.648, \quad \Pi_{1/3} \geq 0.1, \\ H_{1/3}/\eta_{rms} &= 3.8, \qquad\qquad\qquad\quad \Pi_{1/3} < 0.1. \end{aligned} \tag{3.14}$$

With the relation expressed as Eq. (3.14), $H_{1/3}$ predicted by the model are translated to H_{m0}, and the translated H_{m0} and the predicted Q_b are compared with the values measured in cases 1A, 1B, and 1C of the Delta Flume '93 Experiments (Rivero et al., 1994).

The comparisons are shown in Figure 3.7. On the planar beach for case 1A, the predicted values of Q_b and H_{m0} agree with the measured values, whereas the predicted values of Q_b are smaller than the measured ones. On the barred beaches for cases 1B and 1C, predicted values of $H_{1/3}$ are slightly smaller than those measured in the surf zone. The model overestimated Q_b on the seaward slopes of the bars, and underestimated Q_b at the troughs.

3.5 Discussion

As mentioned in Introduction, the stable wave height can be considered as the wave height critical to wave reforming. If so, most values of H_r/h_r in the field were smaller than experimentally obtained values of H_r/h_r reported by Horikawa and Kuo (1966), expressed by Eq. (3.3), and by Kweon and Goda (1994), expressed by Eq. (3.4) (Figure 3.2). This means that waves in the field likely continue breaking longer than those in the experiments.

The cross-shore wind velocity, which ranged from -8.0 m/s to 2.8 m/s in the measurements, had little influence on H_r/h_r. The influence of wind on wave breaking, however, was demonstrated in the field by Galloway et al. (1989) and Dally (1992). Thus, probably wind has some effect on H_r/h_r. The relation between wind velocity and H_r/h_r should be investigated further with data including a wide range of wind velocities.

The weak correlation between H_r/h_r and h_r/L_0 (Figure 3.3) was also observed by Dally (1992) on the basis of the experimental data from Horikawa and Kuo (1966). The experimental data of Kweon and Goda (1994) also show a similar weak correlation. However, the differences between the calculations of H and Q_b with H_r/h_r=0.35 and with Eq. (3.5) are small (Figure 3.6). Hence, as the criterion for wave reforming, H_r/h_r=0.35 is considered to be appropriate.

Although the model that includes the dissipation sub-model of Dally et al. (1985) (with H_r/h_r=0.4) underestimated Q_b at the troughs to a greater degree than the present model (with H_r/h_r=0.35), the differences between H predicted by the models were small. However, there is a possibility that the difference in H increases when the beach slope gets milder or the water depth gets larger. The difference between the performances of the models with H_r/h_r=0.35 and H_r/h_r=0.4 in the estimation of H should be further investigated.

The values of H_{rms} and Q_b predicted by the model by Thornton and Guza (1983) are smaller than those measured. One reason is thought to be that their model does not consider the wave nonlinearity in the calculation of wave shoaling.

The values of $H_{1/3}$, H_{m0} and Q_b predicted by the present model with H_r/h_r=0.35 agree with the measured values. However, the predicted values of $H_{1/3}$ and H_{m0} are slightly smaller than those measured after wave breaking both at HORS and in Delta Flume '93 Experiments, and so are the predicted Q_b in trough regions. In the present model, the wave energy dissipation is estimated with Eqs. (3.8) and (3.10), which were obtained on the basis of small-scale experimental data. The result seems to show that the wave dissipation rate relative to the wave height is smaller in the field than that in small-scale experiments.

Some cross-shore distributions of Q_b show that Q_b increased shoreward of the bar crests. These distributions were observed in six cases (Cases 4, 5, 7, 9, 10, and 11) at HORS out of eight cases where Q_b were measured at the bar crests. Moreover, similar observations were also made during the Delta Flume '93 Experiments (Rivero et al., 1994; Southgate and Wallace, 1994). One possible cause of this distribution is as follows. A wave undergoing wave breaking at a bar crest in the field or in an experiment starts to overturn so that the overturned crest plunges shoreward of the bar crest. Although this wave is counted as a breaking wave shoreward of the bar crest, it is counted as a non-breaking at the bar crest. As a result, Q_b shoreward of the bar crest is greater than that at the crest. Because the present model does not consider this phenomenon, the model cannot predict the distribution.

The present model, which employs the wave-by-wave approach, has a serious limitation; the model cannot predict the change in wave period due to wave decomposition because the model assumes the number of waves is constant. Wave decomposition frequently occurs over longshore bars, and results in a decrease in the wave period. Future improvement of the model is required.

3.6 Conclusions

Field measurements of wave height and the fraction of breaking waves on longshore bars and troughs were carried out at HORS. Water surface elevations were measured with ultrasonic wave gages, and modes of wave breaking (i.e., breaking or broken or

non-breaking) were visually observed.

The wave height-water depth ratio at wave reforming H_r/h_r was estimated to be equal to 0.35. Although H_r/h_r had a weak correlation with h_r/L_0, expressed by Eq. (3.5), the differences between the results of the calculations of H and Q_b with H_r/h_r=0.35 and with Eq. (3.5) are small. As a result, H_r/h_r=0.35 is concluded to be an appropriate criterion for wave reforming. The result that most H_r/h_r in the field are smaller than those in small-scale experiments indicates that waves in the field are likely to keep breaking over longer distances than those in experiments.

A model for $H_{1/3}$ and Q_b that employs the wave-by-wave approach was developed. In the model, the criterion for wave reforming is H_r/h_r=0.35, and that for wave breaking is Eqs. (3.8) and (3.10), which were calibrated with small-scale experimental data. Comparisons between the model, and field and large-scale experimental data showed that the model almost agree with the measurements, whereas the predicted values of $H_{1/3}$, H_{m0} and Q_b are smaller than those measured at troughs in the field. This seems to show that the wave dissipation rate relative to the wave height is smaller in the field than in the experiments.

Appendix

The procedure used to identify the same wave at a seaward and the shoreward measurement points is as follows.

a) The extracted seaward water surface elevations of a wave are a sequence of elevations starting from the minimum elevation preceding the maximum elevation in the wave and ending at the first minus elevation after the maximum. Figure 3.8 shows an example of simultaneously obtained seaward and shoreward water surface elevation data; the vertical dashed lines indicate the zero-down crossing points. Here, let us focus on the wave "A" measured at the seaward point. The extracted data of wave "A" are shown by the bold line in the upper figure.

b) Next, several sets of shoreward data having various time lags behind the extracted seaward data are extracted; the number of the extracted shoreward data points in each set is equal to that of the extracted seaward data. The time lags are from T_l-3 s to T_l+3 s at 0.5 s intervals (13 sets); T_l is the period in which a wave with the mean wave period travels from the seaward point to the shoreward point. Even though an individual wave

period is different from the mean wave period, T_l can still be used because field measurements of Thornton and Guza (1982) show that wave celerities in the surf zone are nearly independent of wave period.

c) The correlation coefficients between the extracted seaward and shoreward data are calculated, and if the maximum correlation coefficient is greater than 0.85, then the shoreward data set having the maximum coefficient is considered to belong to the same wave as the extracted seaward data set. If the extracted shoreward data belong to more than two waves, the wave having the maximum elevation in the extracted shoreward data is designated to be identical to the seaward wave. In the lower figure of Figure 3.8, the shoreward data set having the maximum correlation coefficient, 0.96, is indicated by the solid bold line, and the extracted seaward data set superimposed on it is indicated by the dashed bold line. The shoreward wave "C" is designated to be identical to the seaward wave "A".

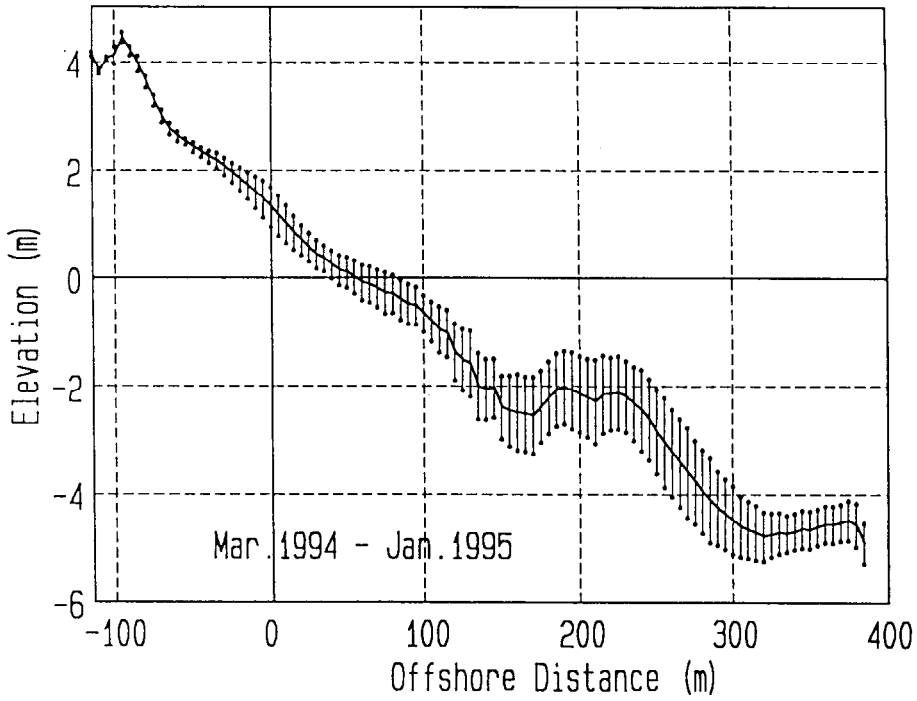

Figure 3.1 Mean beach profile and the standard deviation in elevation from March, 1994 to January 31, 1995.

Table 3.1 Wave and wind conditions during the field measurements

Case	Time	$(H_{1/3})_0$ (m)	$(T_{1/3})_0$ (s)	θ_b (deg.)	W_c (m/s)	W_l (m/s)
1	Mar. 3, 1994, 13:20-14:50	1.28	11.2	10	-3.9	-3.3
2	Mar. 10, 1994, 13:10-14:40	2.27	9.5	5	-8.0	7.4
3	May 13, 1994, 10:20-11:45	0.95	6.2	-5	-5.6	0.1
4	June 13, 1994, 11:35-13:05	0.98	7.9	-20	-0.8	1.8
5	June 14, 1994, 13:20-14:40	1.50	9.2	-5	-2.3	-0.4
6	June 22, 1994, 9:40-11:05	1.00	7.8	15	-0.6	2.8
7	June 28, 1994, 13:20-14:40	1.25	5.6	20	-6.1	3.4
8	Nov. 22, 1994, 10:10-11:40	1.68	7.0	0	-3.2	2.4
9	Jan. 25, 1995, 11:00-12:30	2.37	11.1	15	1.7	6.0
10	Jan. 25, 1995, 14:00-15:30	2.40	11.8	15	0.4	-4.7
11	Jan. 26, 1995, 10:40-12:00	2.38*	13.2*	5	2.8	1.4

* obtained about three hours before the measurement

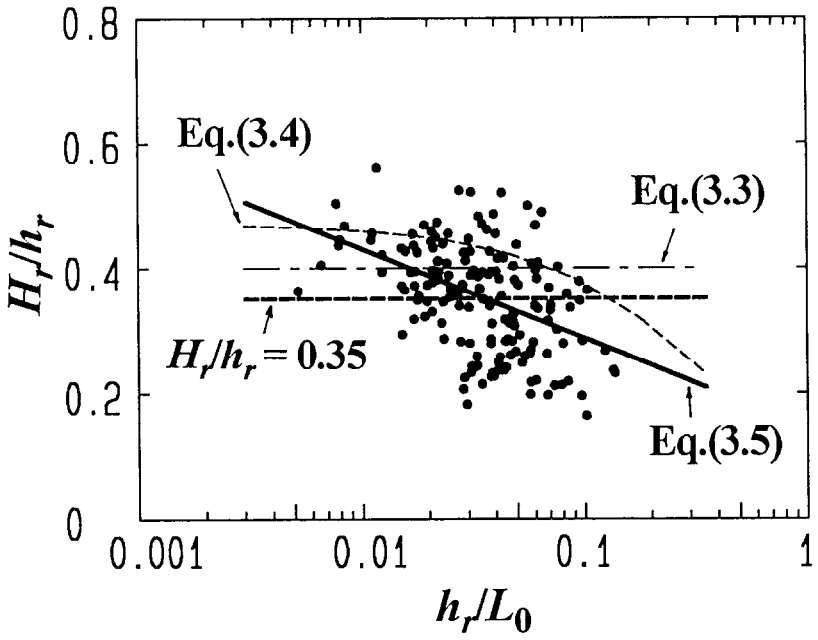

Figure 3.2 Relationship between H_r/h_r and h_r/L_0.

Table 3.2 The values of the coefficients in Eq. (3.9)

$\tan\beta$	α_1	α_2	α_3	α_4	α_5
1/10	0.977	0.0242	0.444	0.988	0.0186
1/20	1.248	-0.249	0.641	0.829	0.0192
1/30	1.397	-0.396	0.706	0.807	0.0195
1/50	1.556	-0.550	0.759	0.803	0.0200

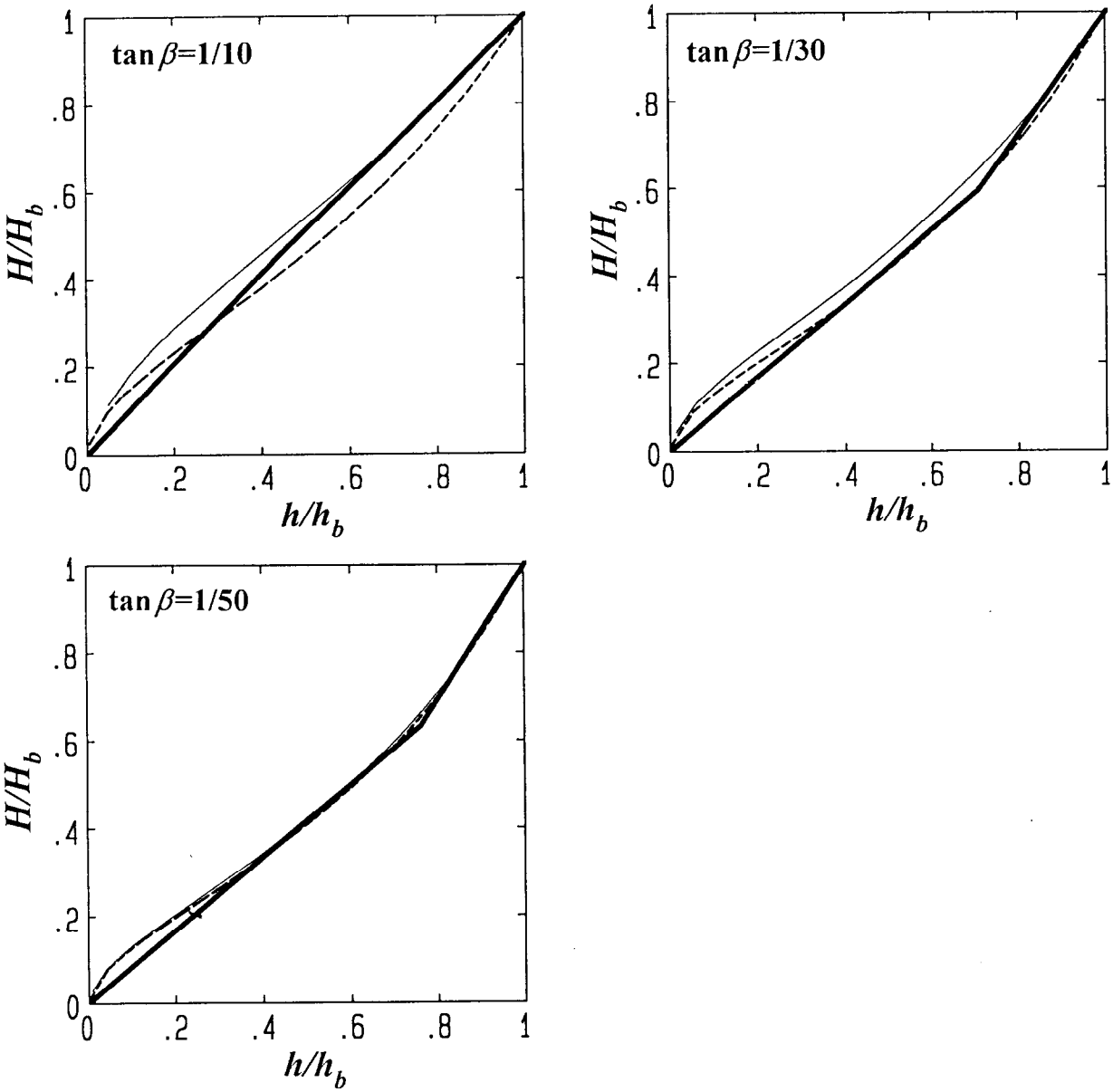

Figure 3.3 Comparisons of H/H_b estimated from Eqs. (3.9) and (3.8). The thick solid lines show the values estimated using Eq. (3.9). The thin solid lines and the broken lines show the values estimated using Eq. (3.8) at H_0/L_0=0.005 and H_0/L_0=0.07, respectively.

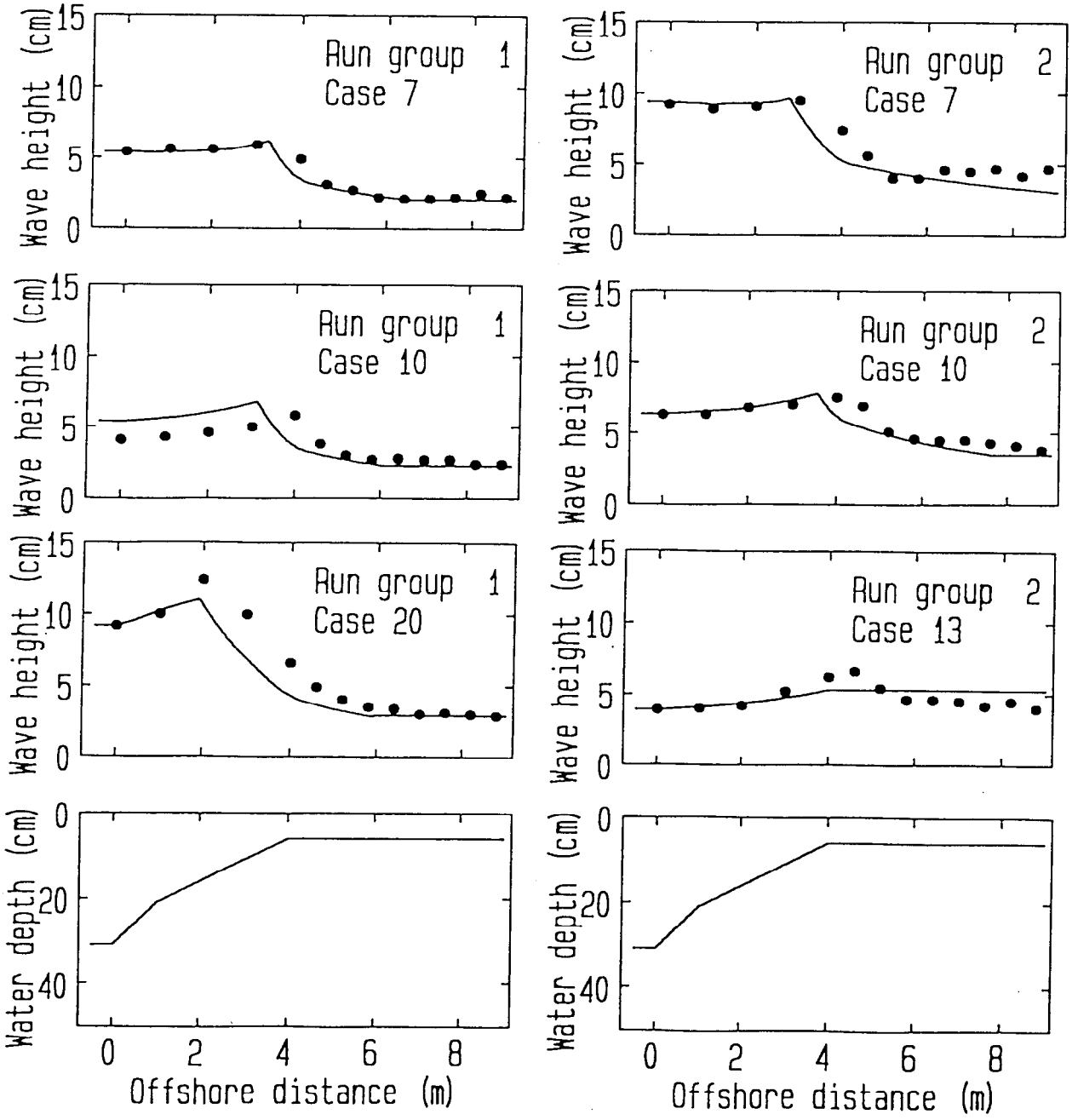

Figure 3.4 Comparisons of wave heights on a flat bed measured in experiments (solid circles) and predicted by Eq. (3.8) (solid lines).

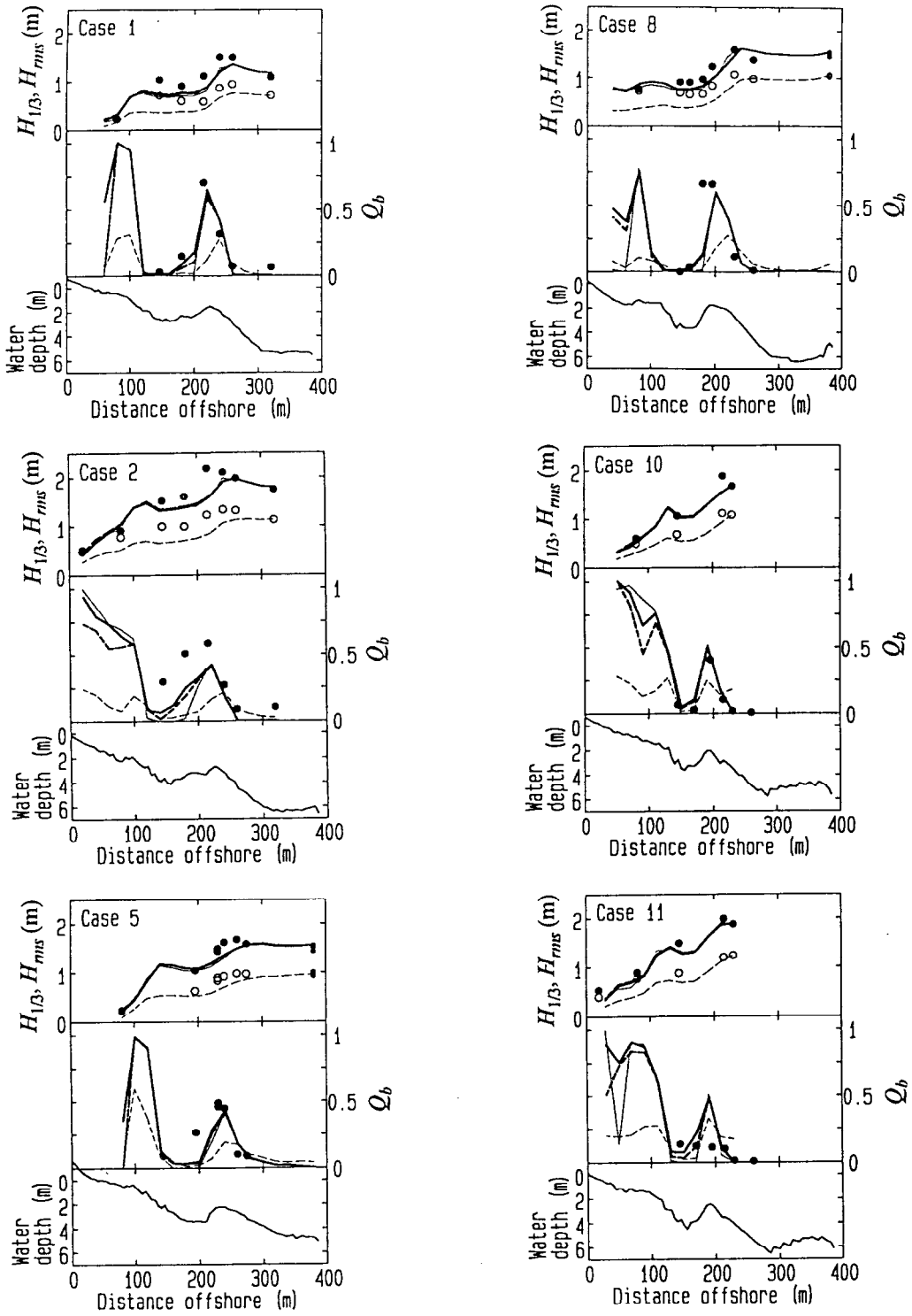

Figure 3.5 Comparisons of measured and predicted values of $H_{1/3}$, H_{rms} and Q_b. The solid circles show $H_{1/3}$ and Q_b measured in the field, and the open circles show H_{rms} measured. The thick solid lines, the thick broken lines and the thin broken lines show $H_{1/3}$ and Q_b predicted by the model with H_r/h_r=0.35, with Eq. (3.5), and with the wave energy dissipation sub-model of Dally et al.(1985), respectively. The thin broken lines show H_{rms} predicted by the model of Thornton and Guza (1983).

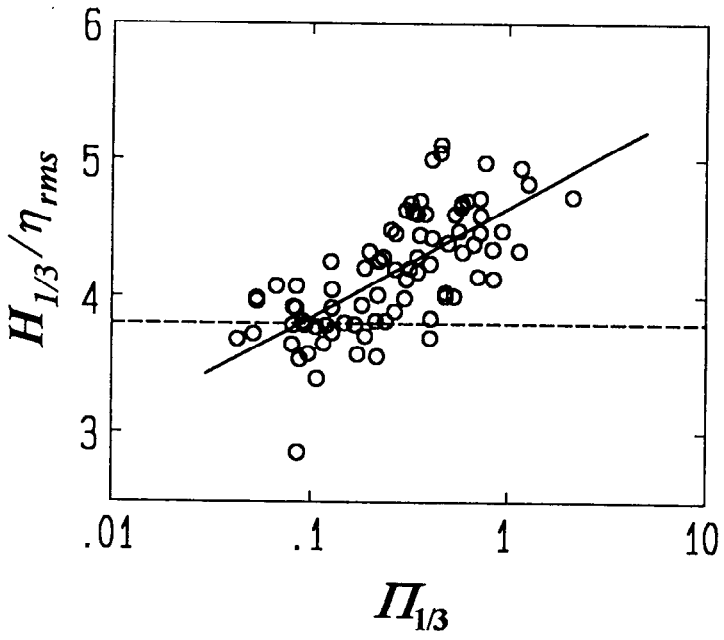

Figure 3.6 Relationship between $H_{1/3}/\eta rms$ and $\Pi_{1/3}$.

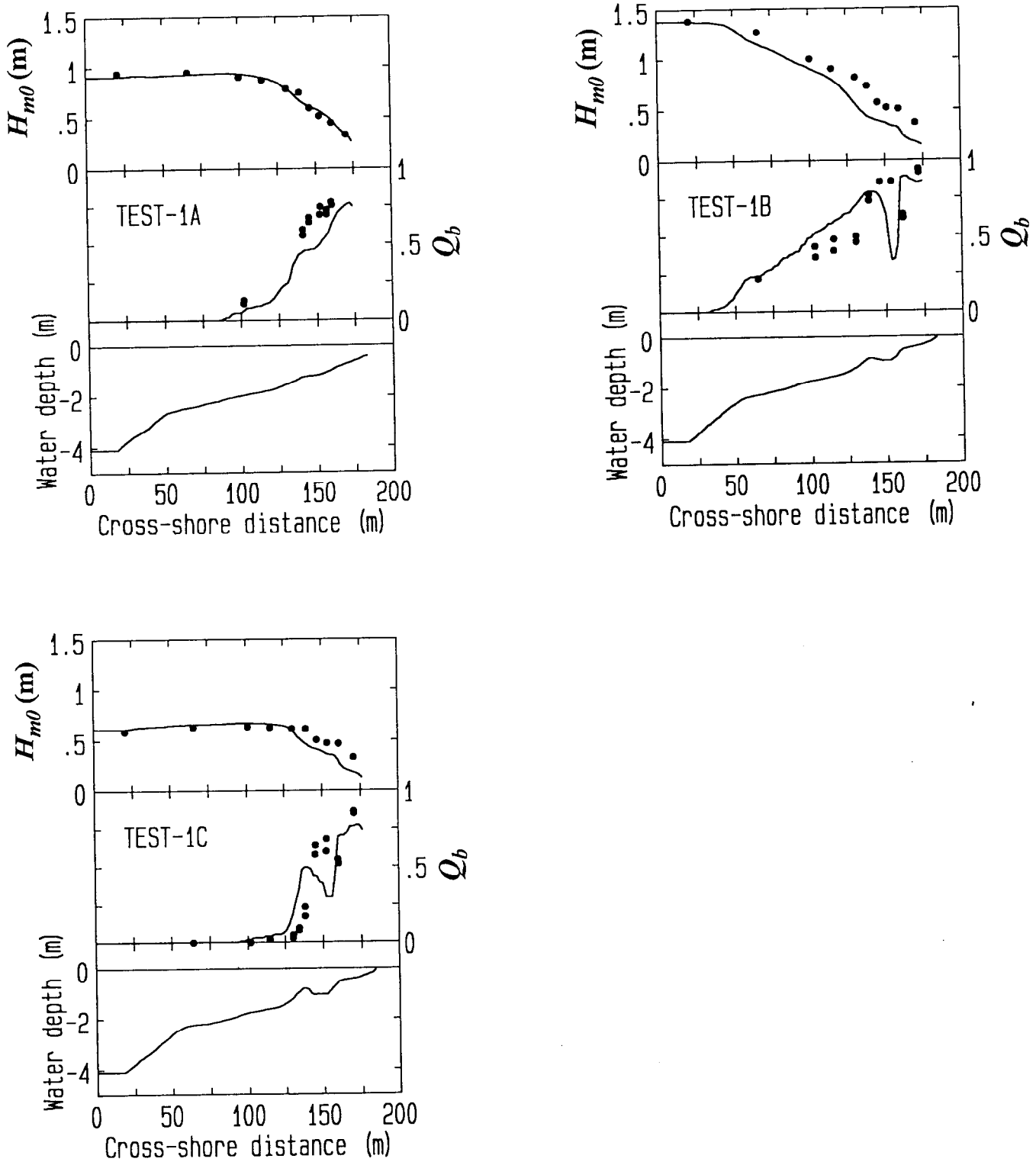

Figure 3.7 Comparisons of H_{m0} and Q_b measured in Delta Flume '93 Experiments (the solid circles) and predicted by the present model with H_r/h_r=0.35 (the solid lines).

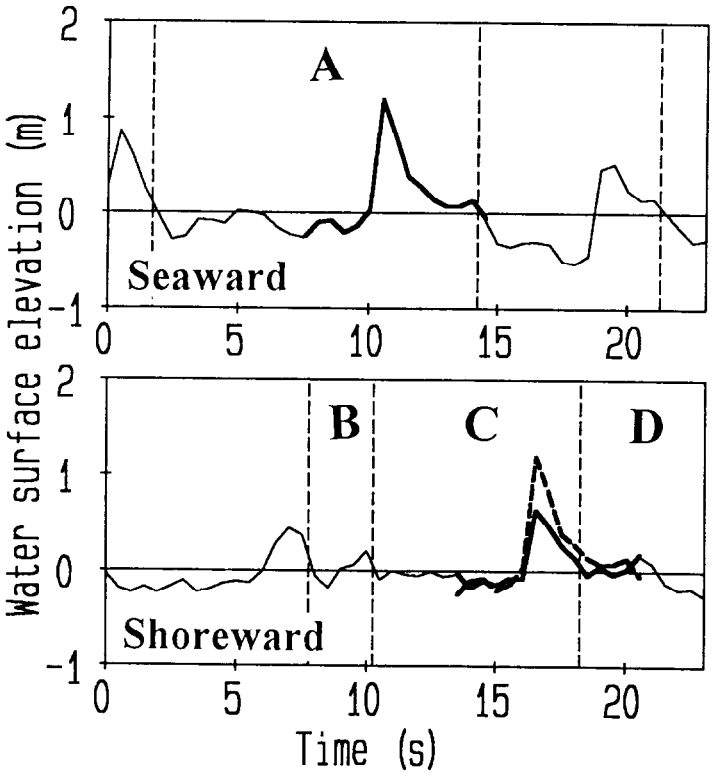

Figure 3.8 Example of seaward (upper panel) and shoreward (lower panel) data of water surface elevation that were obtained simultaneously. The wave "C" is recognized to be identical to the wave "A".

4. Cross-shore distribution of the longshore current

4.1 Introduction

Two types of cross-shore distributions of the time-averaged longshore current velocity have been observed; one type has a peak velocity seaward of the bar crest, and the other type has a peak shoreward of the bar crest. Whitford and Thornton (1988) measured the former distribution in the field. Allender and Ditmars (1981) and Greenwood and Sherman (1986), on the other hand, measured both types. The latter distribution was also measured by Symonds and Huntley (1980) and Church and Thornton (1992).

Although these two types of the cross-shore distributions of the longshore current velocity on barred beaches were shown in previous investigations, the frequencies of the two distributions were not discussed owing to the limited data on the distributions of the longshore current velocity on barred beaches. One objective of this chapter is to discuss the characteristics of the cross-shore distribution of the longshore current velocity on barred beaches on the basis of field data. For this purpose, field measurements of the longshore current velocity on a barred beach were carried out over four years. Then, the cross-shore distributions measured in the field are compared with calculations from a nearshore current model.

4.2 Field measurements

4.2.1 Measurement method

Field measurements at HORS of the longshore current velocity and wave height and period were carried out over four years commencing on January 5, 1987. Figure 4.1 shows the mean beach profile during the four years. The short vertical lines on the beach profile indicate the standard deviations in elevation. During the period, bars were mainly located at around P300m. The arrows in the upper part of the figure show the measurement points of the longshore current velocity and those with "USW" show the measurement points of wave height and period.

A spherical float having a diameter of 0.2 m shown in Figure 4.2 was used in the measurements. Nearshore current velocities at 1 m below the water surface were measured to avoid the effects of winds and waves. This was achieved by making the density of the float slightly greater than that of sea water. The float was connected to an

identification buoy by a 1 m long rope as shown in Figure 4.2. The length of the rope was adequately shortened when the mean water depth was small.

During the measurements, the float was attached to a 30 m line and released from the HORS pier. The time for full extension of the line was measured with a stopwatch. The current velocity was calculated using the time and the length of the line. The transport direction of the float due to nearshore currents was measured with a protractor. At each point, nearshore currents were measured three times.

To measure the nearshore currents along HORS took about 90 minutes. The wave breaking position and the breaking wave direction were visually observed. Water surface elevations were measured with the ultrasonic wave gages for twenty minutes every hour at a sampling frequency of 2 Hz.

4.2.2 Calibration of the measurement method

Longshore current velocities measured with the float were compared with those measured with an electromagnetic current meter to check the accuracy of the measurement method with the float. The electromagnetic current meter was installed at P145m by using a ladder as shown in Figure 4.3. When the distance between the sensor of the current meter and the mean water level was about 1 m, longshore current velocities were measured with the float and with the current meter simultaneously.

Figure 4.4 shows the relationship between the time-averaged longshore current velocities measured with the float U_{FLOAT} and those measured with the current meter U_{EMC}; triangles show the data obtained when the longshore components of the wind velocities were over 8 m/s. Although the velocities measured with the float are larger than those measured with the current meter, there is very strong correlation between them. Furthermore, the effects of winds on the longshore current velocities measured with the float were small. Through this calibration, the float was confirmed to be a simple but useful tool for the measurement of the longshore current velocity.

The relationship between U_{EMC} and U_{FLOAT} is expressed as

$$U_{EMC} = 0.81 U_{FLOAT}. \tag{4.1}$$

In the following analysis, the values of U_{EMC} are used.

As shown in Figure 4.4, the velocities measured with the float were larger than those measured with the current meter. The reason is probably related to the effect of waves

on the identification buoy. The identification buoy is easily transported by waves in the direction of wave propagation because the buoy is on the water surface, where the mass flux due to waves is concentrated. The float is consequently transported in the same direction as the buoy. Because the longshore direction of the wave propagation is usually identical to the direction of the longshore current, the velocities measured with the float were larger than those measured with the current meter.

4.3 Location of a peak velocity of the longshore current over a bar and a trough

Data showing cross-shore distributions of the longshore current velocity measured over longshore bars and troughs obtained at the time when waves were breaking over the bars were analyzed. When the wave height or the incident wave angle is small, the longshore current is usually small and is easily affected by alongshore topographic inhomogeneities. Thus, data sets were eliminated if the peak longshore current velocities over bars and troughs were below 0.25 m/s. The remaining fifty-two cross-shore distributions of the longshore current velocity, obtained during the period from 1987 to 1991, were chosen for the following analysis.

The frequency distributions of the offshore significant wave height H_0 and period T_0, the offshore wave steepness H_0/L_0, and the absolute value of the incident wave angle θ_{tip} for the fifty-two measurements are shown in Figures 4.5 (1) to (4). The values of H_0 and T_0 were estimated on the basis of the offshore wave data at a water depth of 23.4 m. The value of θ_{tip} is the incident wave angle visually observed at the tip of the HORS; the error of θ_{tip} is expected to be ±5°. The ranges of H_0 and T_0 are from 1 m to 3.6 m, and from 5 s to 13 s; the mean values of H_0 and T_0 are 1.9 m and 7.7 s. Accordingly, the range and the mean value of H_0/L_0 are from 0.007 to 0.04, and 0.022, respectively. The absolute value of θ_{tip} varies from 0° to 30°.

Figures 4.6 (1) and (2) show the relationship between the offshore distance of the bar crest y_{bar} and that of the trough y_{trough}, as well as that between the water depth at the bar crest h_{bar} and that at the trough h_{trough}, along with their frequency distributions. The bar crests are formed around P290m, whereas the troughs are formed around P220m. The values of h_{bar} and h_{trough} range from 2.4 m to 4.5 m, and from 3.7 m to 6.0 m, respectively; the mean values of h_{bar} and h_{trough} are 3.4 m and 4.7 m, respectively.

The relationship between the peak longshore current velocity in the area from the tip

of HORS to the trough U_{peak} and the mean longshore current velocity in the area U_{ave} is shown in Figure 4.7 with their frequency distributions. The values of U_{peak} are larger than U_{ave} by 0.05 m/s to 0.25 m/s. Although the values of U_{peak} are widely distributed from 0.25 m/s to 1.1 m/s, most of the values are below 0.6 m/s.

The fifty-two distributions measured at HORS are classified into two groups based on the location of the peak velocity of the longshore current over the bar and trough. The distribution in the first group has a peak velocity shoreward of the bar crest, and that in the second group has a peak velocity seaward of the bar crest.

Three examples of the cross-shore distributions of the longshore current velocity are shown in Figures 4.8 (1) to (3). Two examples belong to the first group, and the other belongs to the second one. Figure 4.8 (1) shows a distribution that has a peak velocity shoreward of the bar crest. Note that the signs of the longshore current velocities are changed from minus to plus in this figure. This distribution was measured on March 28, 1989. Horizontal arrows indicate the breaker zones, and a vertical arrow indicates the location of the peak velocity over the bar and the trough. Waves broke over the bar, reformed over the trough and broke again around P145m. The longshore current velocity increased in the shoreward direction from the tip of HORS. After reaching maximum slightly shoreward of the bar crest, the longshore current velocity decreased. Then, the velocity increased again in the secondary surf zone.

Another example of the cross-shore distribution of the longshore current velocity that has a peak velocity shoreward of the bar crest is shown in Figure 4.8 (2). This distribution was measured on November 28, 1987. Waves broke not only seaward of the bar crest but also shoreward of the bar crest. After reforming over the trough, waves broke again between P140m and P80m. The longshore current velocity slightly increased from the tip of HORS, and reached maximum at the trough. From P220m to P190m, the velocity decreased, and increased again in the secondary breaker zone between P140m and P80m.

In contrast to the previous two examples, Figure 4.8 (3) shows an example of the longshore current distribution that has a peak velocity seaward of the bar crest. The distribution was measured on May 12, 1989. After breaking over the bar, waves reformed over the trough and broke again around P140m. The longshore current velocity increased from P380m to P350m. After reaching peak at P350m, the longshore

current velocity gradually decreased over the bar and the trough, and increased again in the secondary breaker zone.

The relationship between y_{bar} and the offshore distance of the location of the peak longshore current velocity over the bar and the trough y_{peak} is shown in Figure 4.9 (1) along with their frequency distributions. Though the values of y_{bar} are concentrated in the area from P280m to P320m, the values of y_{peak} are widely distributed from P180m to P340m.

Figure 4.9 (2) shows the frequency distribution of the seaward distance from y_{bar} to y_{peak}. Although cross-shore distributions of the longshore current velocity calculated using one-dimensional models of the longshore current velocity have peak velocities seaward of the bar crests (Ebersole and Dalrymple, 1980; Symonds and Huntley, 1980; Larson and Kraus, 1991), 85 percent of the distributions measured at HORS had peaks shoreward of the bar crests.

4.4 Model comparisons with measurements

Symonds and Huntley (1980) and Allender and Ditmars (1981) assumed that the cross-shore distribution of the longshore current velocity with peaks shoreward of the bar crest is caused by the longshore gradient in wave setup. At HORS, however, the distribution was sometimes observed even when no rip currents were observed near HORS. The absence of rip currents probably indicates that the longshore gradient in the wave setup was very small. Hence, cross-shore distributions of the longshore current velocity measured at HORS are compared with those predicted with a horizontally two-dimensional nearshore current model.

4.4.1 Model

The model consists of two computationally distinct numerical models, a wave height transformation model and a nearshore current model.

(1) Wave height transformation model

The basic equation and the procedure of the present model for wave height transformation are based on the model for directional random waves proposed by Takayama et al. (1991). Eq. (4.2) expresses the energy equation of a wave component.

$$
\begin{aligned}
&\frac{\partial(D_s V_x)}{\partial x}-\frac{\partial(D_s V_y)}{\partial y}+\frac{\partial(D_s V_\theta)}{\partial \theta}=-D', \\
&D_s = S(f,\theta)\delta f \delta\theta, \\
&V_x = C_g \sin\theta,\ V_y = C_g \cos\theta, \\
&V_\theta = \frac{C_g}{C}\left(-\cos\theta\frac{\partial C}{\partial x}-\sin\theta\frac{\partial C}{\partial y}\right),
\end{aligned}
\tag{4.2}
$$

where D_s is the wave energy, S is the directional wave spectral density, δf is the frequency band width, $\delta\theta$ is the directional band width, C_g is the group velocity, θ is the wave direction, C is the celerity, and D' is the wave energy dissipation rate.

Takayama et al. (1991) introduced a wave energy dissipation term into Karlsson's model (1969), which is based on the balance of wave energy. The wave dissipation rate calculated from their model is proportional to the beach slope. Thus, the calculated wave dissipation rate on a bar crest, where the beach slope is equal to zero, becomes zero. However, in the field, wave energy is evidently dissipated even on a bar crest because waves break on bar crests. Consequently, the wave dissipation term of Takayama et al. (1991) was not adopted in the present model.

In Chapter 3, a wave dissipation sub-model was proposed using Eq. (3.8) with H_r/h_r=0.35 for the wave reforming criterion. However, in this chapter, the sub-model of Dally et al. (1985), expressed as Eq. (3.11), was adopted after some improvements because it was easily introduced into the wave energy equation expressed by Eq. (4.2).

Modification of Eq. (4.2) with Eq. (3.11) yields Eq. (4.3) for directional random waves.

$$
\begin{aligned}
&\frac{\partial(D_s V_x)}{\partial x}-\frac{\partial(D_s V_y)}{\partial y}+\frac{\partial(D_s V_\theta)}{\partial \theta}=-\frac{K}{h}\left(D_s C_g - D_s\frac{E_s}{E}C_g\right), \\
&E_s=\frac{1}{16}\rho g\left(H_{1/3}\right)_s^2,\quad \left(H_{1/3}\right)_s=\Gamma\cdot h,
\end{aligned}
\tag{4.3}
$$

where $(H_{1/3})_s$ is the stable significant wave height.

Although Dally et al. (1985) assumed that K and Γ are constant in Eq. (3.11) (see Chapter 3), wave energy dissipation in the surf zone is affected by the beach slope as they mentioned. Hence, the influences of the beach slope $\tan\beta$ on the coefficients K and Γ were examined on the basis of the calculations of the wave height transformation in the surf zone for offshore wave steepness of 0.02 reported by Goda (1975). As a result, K and Γ are expressed as

$$K = 1.7 \cdot 10^{a}, \qquad a = -0.857 \log_{10}(1/\tan\beta) + 0.219, \tag{4.4}$$

and

$$\Gamma = -0.141 \log_{10}(1/\tan\beta) + 0.56. \tag{4.5}$$

The significant wave height $H_{1/3}$ and the principal wave direction θ_p are calculated by

$$H_{1/3} = 4.0\sqrt{m_0}, \qquad m_0 = \int_0^{\infty}\int_{-\pi/2}^{\pi/2} D_s \, d\theta \, df, \tag{4.6}$$

and

$$\theta_p = \int_0^{\infty}\int_{-\pi/2}^{\pi/2} \theta \cdot D_s \, d\theta \, df / m_0. \tag{4.7}$$

(2) Nearshore current model

a. Basic equations

A typical model for nearshore current (e.g., Nishimura, 1988) was used. The basic equations of the model are expressed as

$$\frac{\partial \overline{\eta}}{\partial t} + \frac{\partial (h+\overline{\eta})U}{\partial x} + \frac{\partial (h+\overline{\eta})V}{\partial y} = 0, \tag{4.8}$$

$$\frac{\partial U}{\partial t} + U\frac{\partial U}{\partial x} + V\frac{\partial U}{\partial y} + F_x - L_x + R_x + g\frac{\partial \overline{\eta}}{\partial x} = 0, \tag{4.9}$$

$$\frac{\partial V}{\partial t} + U\frac{\partial V}{\partial x} + V\frac{\partial V}{\partial y} + F_y - L_y + R_y + g\frac{\partial \overline{\eta}}{\partial y} = 0, \tag{4.10}$$

$$R_x = \frac{1}{\rho(h+\overline{\eta})}\left(\frac{\partial S_{xx}}{\partial x} + \frac{\partial S_{yx}}{\partial y}\right), \quad R_y = \frac{1}{\rho(h+\overline{\eta})}\left(\frac{\partial S_{xy}}{\partial x} + \frac{\partial S_{yy}}{\partial y}\right), \tag{4.11}$$

$$L_x = \frac{\partial}{\partial x}\left(\varepsilon\frac{\partial U}{\partial x}\right) + \frac{\partial}{\partial y}\left(\varepsilon\frac{\partial U}{\partial y}\right), \quad L_y = \frac{\partial}{\partial x}\left(\varepsilon\frac{\partial V}{\partial x}\right) + \frac{\partial}{\partial y}\left(\varepsilon\frac{\partial V}{\partial y}\right). \tag{4.12}$$

where $\overline{\eta}$ is the elevation of the mean water level, t is time, and U and V are the depth and time-averaged velocities in the x-direction and the y-direction, respectively. The values of F_x and F_y are the bottom friction terms, L_x and L_y are the lateral mixing terms, ρ is the density of the sea water, S_{xx}, S_{xy} and S_{yy} are the radiation stress components, and ε is the lateral mixing coefficient. Subscripts x and y denote the values in the x-direction

and the y-direction, respectively.

b. Radiation stress, bottom shear stress and lateral mixing

Radiation stresses of directional random waves are calculated by Eq. (4.13) proposed by Yamaguchi(1988).

$$
\begin{aligned}
S_{xx} &= \int_0^{\infty}\int_{-\pi/2}^{\pi/2} \rho g\{\frac{C_g}{C}\sin^2\theta+(\frac{C_g}{C}-\frac{1}{2})\}D_s d\theta df,\\
S_{xy} &= S_{yx} = \int_0^{\infty}\int_{-\pi/2}^{\pi/2} \rho g\frac{C_g}{C}\cos\theta\sin\theta D_s d\theta df,\\
S_{yy} &= \int_0^{\infty}\int_{-\pi/2}^{\pi/2} \rho g\{\frac{C_g}{C}\cos^2\theta+(\frac{C_g}{C}-\frac{1}{2})\}D_s d\theta df.
\end{aligned}
\tag{4.13}
$$

Eqs. (4.14) to (4.16), which were proposed by Nishimura(1982), are used for the calculation of bottom shear stresses, F_x and F_y. The value of 0.005 is used as the friction coefficient C_f as used previously by Kuriyama and Ozaki (1993). The value of 0.005 was originally determined by Kuriyama et al. (1992) to give a best fit to the longshore current velocities in the 162 cases measured with the float at HORS.

$$
F_x=\rho C_f\{(W+\frac{wb^2}{W}\sin^2\theta_p)U-\frac{wb^2}{W}\sin\theta_p\cos\theta_p V\}. \tag{4.14}
$$

$$
F_y=\rho C_f\{\frac{wb^2}{W}\sin\theta_p\cos\theta_p U-(W+\frac{wb^2}{W}\cos^2\theta_p)V\}. \tag{4.15}
$$

$$
\begin{aligned}
W = \{&\sqrt{U^2+V^2+w_b^2+2(U\sin\theta_p-V\cos\theta_p)w_b}\\
&+\sqrt{U^2+V^2+w_b^2+2(U\sin\theta_p-V\cos\theta_p)w_b}\}/2,
\end{aligned}
\tag{4.16}
$$

$$
w_b = 2\cdot v_m(-h)/\pi, \quad v_m(-h)=\frac{\pi\cdot H_{1/3}}{T\sinh(2\pi h/L)}.
$$

The lateral mixing coefficient proposed by Battjes (1975) is used in the present model. This coefficient is given by

$$
\varepsilon = Mh\left(\frac{D}{\rho}\right)^{1/3}, \tag{4.17}
$$

where D is the total wave energy dissipation rate and M is a dimensionless coefficient.

Lateral mixing is probably related to the turbulence in the water; the turbulence due to breaking waves is much larger than that due to non-breaking waves. Although the lateral mixing coefficient proposed by Longuet-Higgins (1970) is widely used, he did

not consider wave breaking. Thus, the coefficient proposed by Longuet-Higgins is considered to indicate the upper limit as mentioned by Battjes (1975). In a trough, the actual rate of lateral mixing is likely to be much smaller than that calculated with the coefficient proposed by Longuet-Higgins (1970). In contrast, the lateral mixing rate calculated with the coefficient proposed by Battjes probably agrees with the actual values because it is based on the wave energy dissipation caused by wave breaking. Thus, the lateral mixing coefficient proposed by Battjes (1975) was adopted in the present model.

Nearshore currents are calculated with M = 2, 5 and 10, and are compared with the measured values because the dimensionless coefficient M has not been thoroughly investigated, and the optimal M value for nearshore current is unknown.

(3) Calculation conditions

Nearshore currents measured on March 24, 28 and April 4, 1989 were chosen to compare with the longshore current velocities calculated from the model for the following reasons:

(a) Bars and troughs were formed.

(b) Waves broke over the bars.

(c) A topographic survey near HORS was conducted on March 31, 1989. Beach profile changes during March 24 and April 4 are interpreted to be small owing to the relatively small wave heights during this period.

Figure 4.10 (1) shows a topographic map on March 31, 1989, and Figure 4.10 (2) shows the beach profile along HORS (thick line) and the mean beach profile in the region 100m to 300m from HORS alongshore (thin line). The short vertical lines indicate the standard deviations in elevation in the region at a distance from HORS. The location of the bar crest, the water depth at the bar crest and the location of the trough in the beach profile along HORS agree with those of the mean beach profile in the region at a distance from HORS, although scours occurred around the tip of HORS and P200m, where pilings are concentrated.

The calculation areas extend from the shorelines to y = 650 m, and from x = -320 m to x = 320 m.

a. Wave height transformation

The grid distances in the x-direction and the y-direction for the calculation of wave height transformation are 10 m. The numbers of the frequency components and the directional components are 10 and 35, respectively.

The wave heights $(H_{1/3})_{ob}$ and periods $(T_{1/3})_{ob}$, the principal wave directions $(\theta_p)_{ob}$, and the spreading parameters $(s_{max})_{ob}$ at the offshore boundaries are listed in Table 4.1. The values of $(H_{1/3})_{ob}$ were estimated on the basis of the offshore wave data at a water depth of 23.4 m, and the values of $(T_{1/3})_{ob}$ were assumed to be equal to the offshore values. The principal wave directions $(\theta_p)_{ob}$ were estimated on the basis of the visual observations at the tip of HORS using the graph of the wave direction of random waves due to refraction by Goda and Suzuki (1975). The spreading parameters in deep water were assumed to be 10; the values of $(s_{max})_{ob}$ were obtained with the graph of spreading parameter in shallow water by Goda and Suzuki (1975).

The Bretschneider-Mitsuyasu frequency spectrum and the Mitsuyasu-type spreading function were given at the offshore boundaries.

A beach slope below 1/100 and that over 1/10 were replaced by 1/100 and 1/10, respectively, because Eqs. (4.4) and (4.5) are valid for beach slopes in the range from 1/100 to 1/10.

b. Nearshore current

The nearshore currents in the surf zone were calculated by the ADI (Alternating Direction Implicit) method (e.g., Horie et al., 1977; Nishimura, 1988). The grid distances in the x-direction and the y-direction are 10 m, which are the same values used in the wave transformation calculation. The time step was set to be 0.4 s. The number of iterations was determined to be 4000.

The nearshore current velocities were assumed to be equal to zero at the offshore boundaries and at the shorelines. The nearshore current velocities and the mean water levels at the side boundaries were assumed to be equal to the values at internal grid points next to the side boundaries.

4.4.2 Comparisons

(1) Wave height

Figures 4.11 (1) to (3) show the significant wave heights that were predicted (solid lines) and measured (closed circles) on March 24, 28 and April 4. The predicted values agree well with the measured values except for the data near the shorelines on March 28 and on April 4 .

Causes of the small disagreement between the measured and calculated values near the shorelines are likely to be wave setup and infragravity waves. When the offshore wave height is large, the amount of wave setup and the infragravity wave height are large near the shoreline; these phenomena were observed at HORS by Yanagishima and Katoh (1990) and by Nakamura et al. (1992). Infragravity waves and wave setup, however, are not taken into account in the model. Disregarding these two factors results in the disagreement between the calculated values and the measured values near the shorelines.

Although the model does not consider the effect of the offshore wave steepness on the wave energy dissipation in the surf zone, the calculated values agree well with the measured values. The values of the offshore wave steepness on March 24, 28 and April 4 are between 0.013 and 0.022; the scattering of the offshore wave steepness around 0.02, which was used for the improvements of K and Γ, is small. Thus, the calculated values agree reasonably well with the measured values.

(2) Nearshore current

Figure 4.12 (1) shows the nearshore current on March 24, 1989, predicted by the present model with M = 5, which is the optimal value for the nearshore current on this date. The right part of the figure shows the beach profile along HORS (solid line) and that in the region at a distance from HORS (broken line). Although the direction of the nearshore current veers slightly seaward at x = -50 m between y = 200 m and y = 300 m, where the trough is located, the nearshore current is almost uniform alongshore.

Figure 4.12 (2) compares the measured (solid circles) and the predicted (solid line) longshore current velocities along HORS. The model prediction of the cross-shore distribution of the longshore current velocity over the bar and the trough disagrees with the measured distribution especially at the trough. The measured distribution has a peak that lies shoreward of the bar crest, whereas the model predicts a peak seaward of the bar crest.

Figure 4.13 (1) shows the nearshore current on March 28, 1989, predicted by the present model with M = 5. This nearshore current is also almost uniform alongshore although the direction of the nearshore current at the trough changes slightly at x = -50 m.

Figure 4.13 (2) shows the measured and predicted longshore current velocities along HORS. Seaward of the bar crest, the values predicted by the model increase toward the shore, and are in reasonable agreement with the measured values. Shoreward of the bar crest, on the other hand, the measured values increase toward the shore although the predicted values decrease. Consequently, the longshore current velocities over the trough predicted by the model disagree with the measured values.

Figure 4.14 (1) shows the nearshore current on April 4, 1989, predicted by the present model with M = 10; the predicted current is almost uniform alongshore. Figure 4.14 (2) shows that the difference between the predicted and measured longshore current velocities is small. However, the predicted values are smaller than those measured at the trough.

4.5 Discussion

Eighty-five percent of the cross-shore distributions of the longshore current velocity measured at HORS had peak velocities shoreward of the bar crests as shown in Figure 4.9 (2). In contrast, such velocities predicted using previously proposed one-dimensional models for the longshore current velocity have peaks seaward of the bar crests (Ebersole and Dalrymple, 1980; Symonds and Huntley, 1980; Larson and Kraus, 1991). In the one-dimensional models, the driving force of the longshore current is the cross-shore gradient of the radiation stress. This gradient is largest seaward of a bar crest owing to the large dissipation of wave energy due to wave breaking. Hence, the predicted longshore current velocity has a peak velocity seaward of the bar crest, not shoreward of the bar crest.

Symonds and Huntley (1980) and Allender and Ditmars (1981) assumed that peak velocities of the longshore current that lie shoreward of bar crests are caused by the longshore gradient of wave setup. However, the comparisons between the cross-shore distributions of the longshore current velocity measured at HORS and those predicted with the 2D-horizontal nearshore current model (Figures 4.11 to 4.13) indicate that peak

velocities shoreward of bar crests are generated even when the alongshore inhomogeneity in nearshore current is small.

Mass and momentum fluxes due to bores are thought to be significant for the longshore current velocity with a peak shoreward of a bar crest. Mass transport due to waves was usually neglected in previous nearshore current models. This is because the effect of the mass flux on nearshore current is considered to be small on the basis of calculations using a formula for unbroken waves (Yamaguchi et al., 1983). However, the mass flux due to bores in the surf zone is several times that calculated with a formula for unbroken waves (Nadaoka and Kondoh, 1982). This means that momentum flux due to bores is much greater than that due to unbroken waves because the momentum flux is proportional to the square of the mass transport velocity.

Shoreward of bar crests, the cross-shore flux of the longshore momentum due to bores decreases toward the shore owing to bore decay. This decrease means that the cross-shore flux of the longshore momentum transported into a unit volume is larger than that transported out of the volume. Consequently, the longshore current velocities calculated with the momentum flux due to bores are larger than those calculated without the flux. In contrast, seaward of bar crests, the cross-shore flux of the longshore momentum due to bores increases toward the shore owing to bore development, and hence the longshore current velocities calculated with the flux are smaller than those calculated without the flux. As a result, the cross-shore distribution of the longshore current calculated with the momentum flux due to bores would have a peak shoreward of the bar crest.

Although eighty-five percent of the cross-shore distributions of the longshore current velocity measured at HORS had peak velocities shoreward of the bar crests, fifteen percent had peak velocities seaward of the bar crests. A possible cause of the latter distribution is bore decay seaward of the bar crest. When Whitford and Thornton (1988) measured the latter distribution, the fraction of breaking waves decreased toward the shore even seaward of the bar crest. The decrease of the fraction of the breaking waves was probably attributed to bore decay. The cross-shore flux of the longshore momentum due to bores in the area where bores decay induces a large longshore current velocity as mentioned above, and results in the cross-shore distribution of the longshore current with a peak seaward of the bar crest.

4.6 Conclusions

Field measurements of longshore current were carried out at HORS when waves broke over bars. A spherical float having a diameter of 0.2 m was used to measure nearshore current velocities 1 m below the water surface. This measurement method with the float was confirmed to be useful by comparison with an electromagnetic current meter.

Eighty-five percent of the measured distributions of the longshore current velocity had peak velocities shoreward of the bar crests, while the remaining fifteen percent of the measured distributions had peak velocities seaward of the bar crests.

Although eighty-five percent of the distributions had peaks shoreward of the bar crests, previously proposed one-dimensional models for the longshore current velocity can reproduce only peak velocities seaward of bar crests, not peaks shoreward of bar crests. The calculations of the nearshore current around HORS with a 2D-horizontal model showed that a peak velocity of the longshore current shoreward of a bar crest is generated even when the alongshore inhomogeneity in the nearshore current is small. This result suggests that the alongshore gradient in the mean water level, which corresponds to the alongshore inhomogeneity in the nearshore current, is not the only cause of peak velocities shoreward of bar crests. Mass and momentum fluxes due to bores, which are neglected in previous models, are considered to play a significant role for the longshore current with peaks shoreward of bar crests because mass flux due to bores in the surf zone is several times that calculated with a formula for unbroken waves.

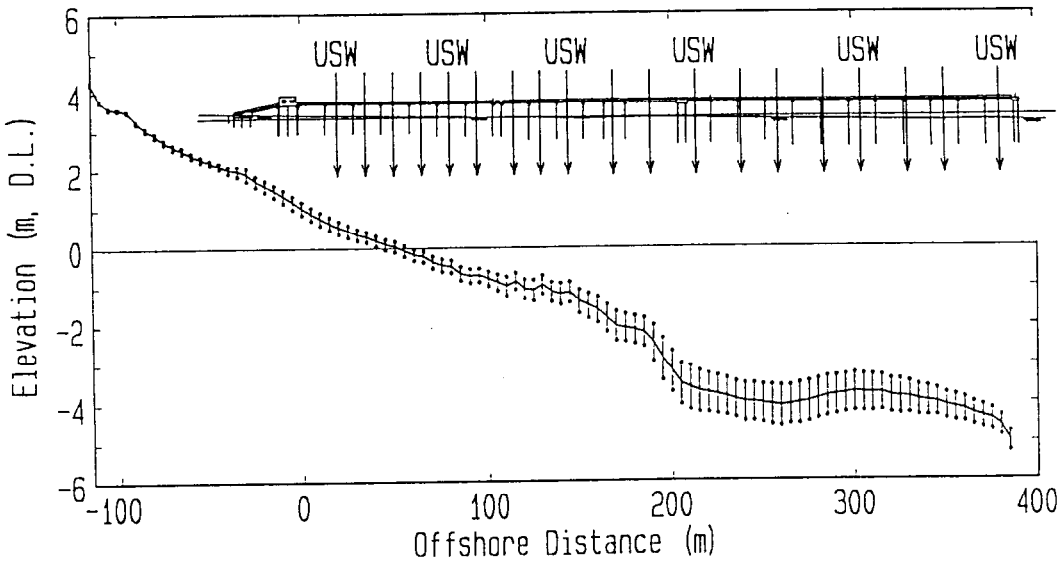

Figure 4.1 Mean beach profile over the course of the four year investigation, showing the measurement points.

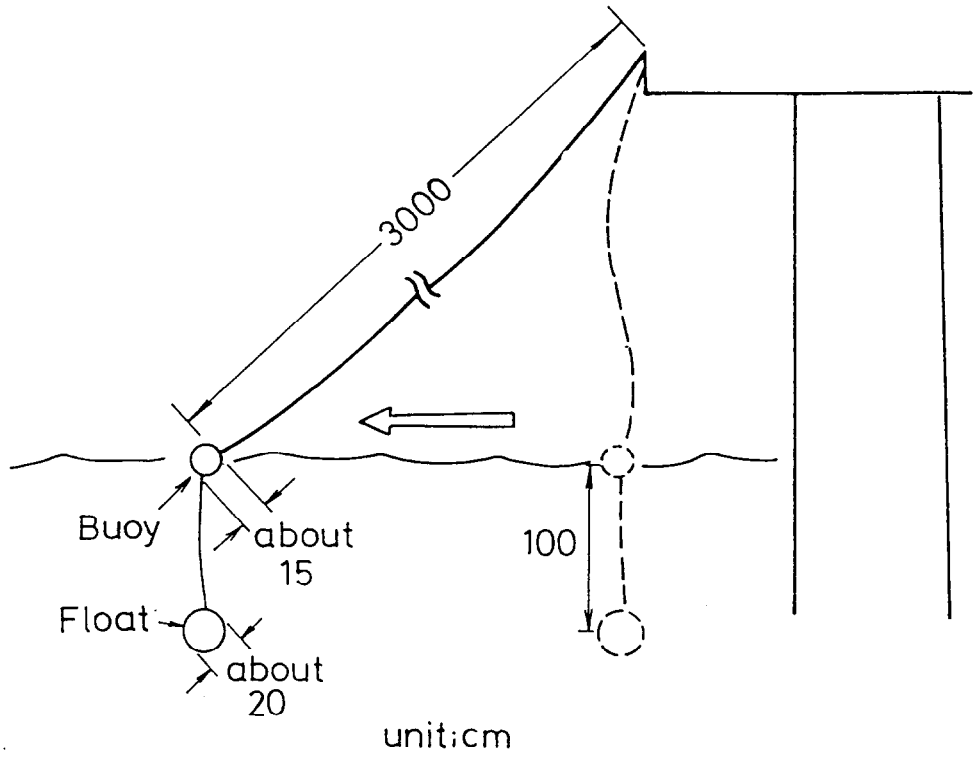

Figure 4.2 Schematic diagram of float used for measurements of longshore current velocity.

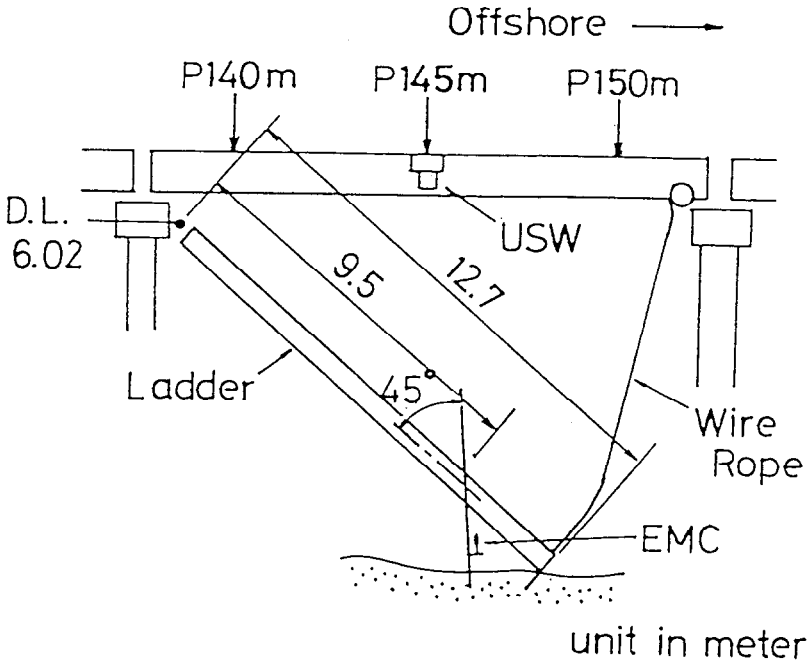

Figure 4.3 Diagram showing installation of an electromagnetic current meter at P145m.

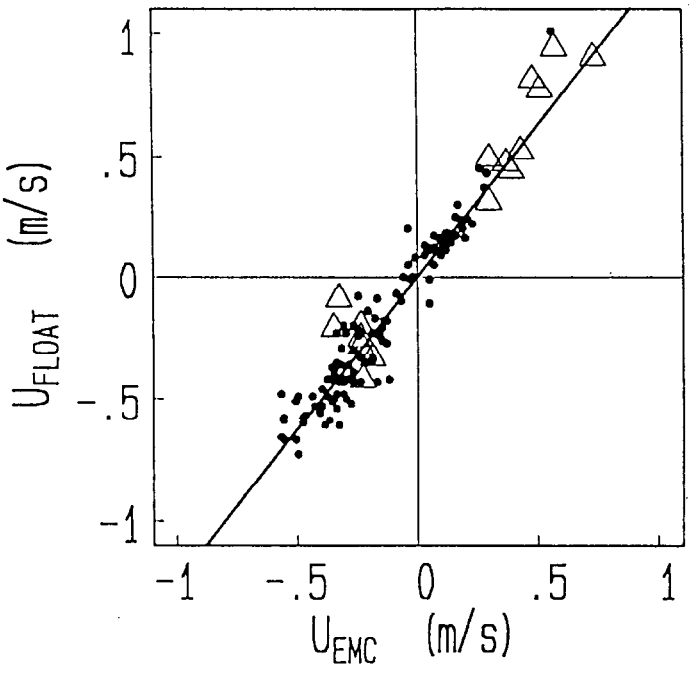

Figure 4.4 Relationship between U_{EMC} and U_{FLOAT}.

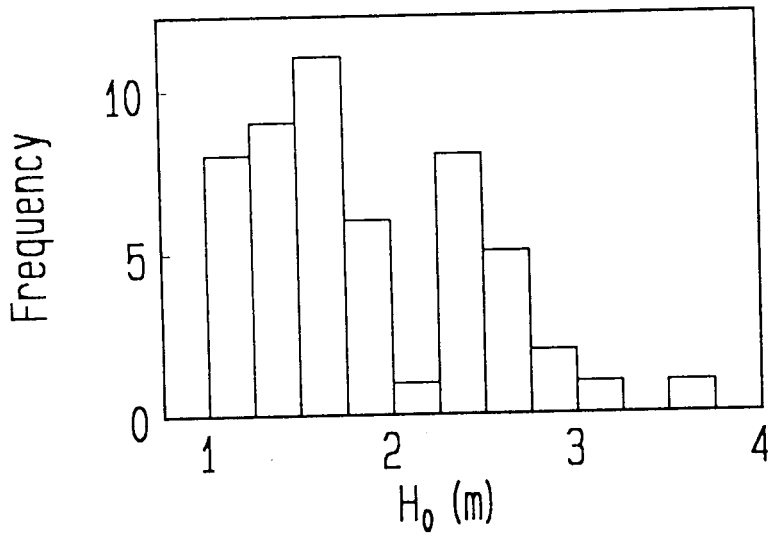

Figure 4.5 (1) Frequency distribution of H_0.

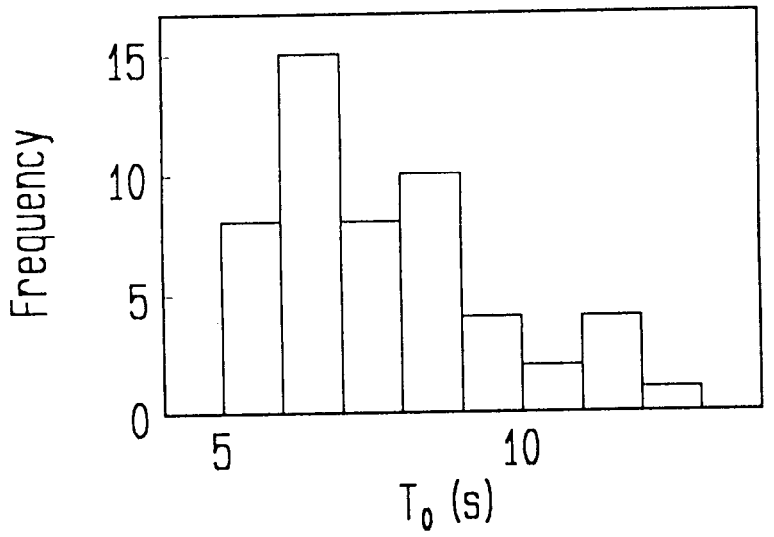

Figure 4.5 (2) Frequency distribution of T_0.

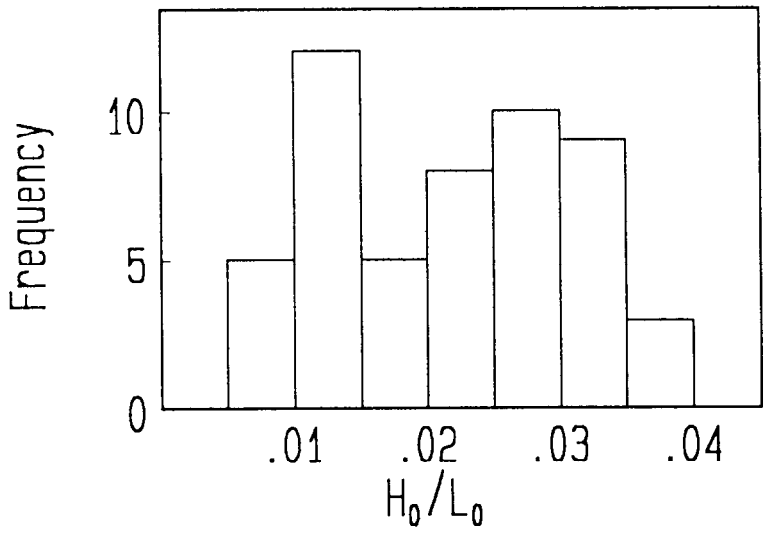

Figure 4.5 (3) Frequency distribution of H_0/L_0.

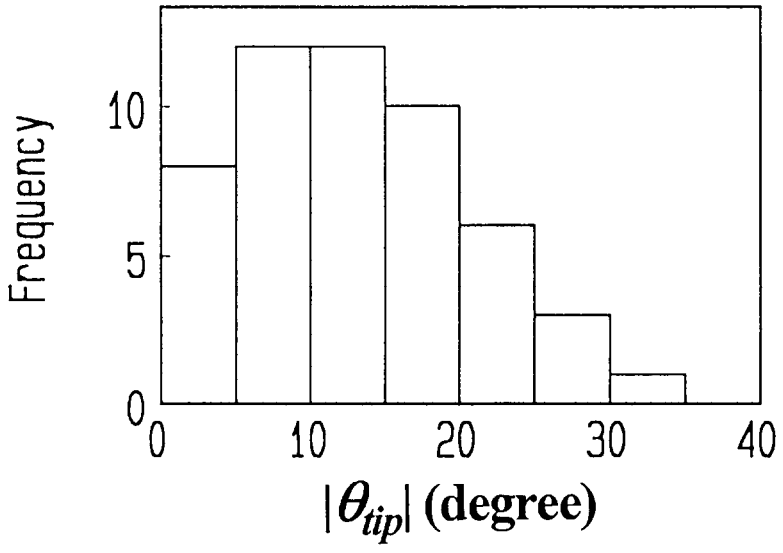

Figure 4.5 (4) Frequency distribution of the absolute value of θ_{tip}.

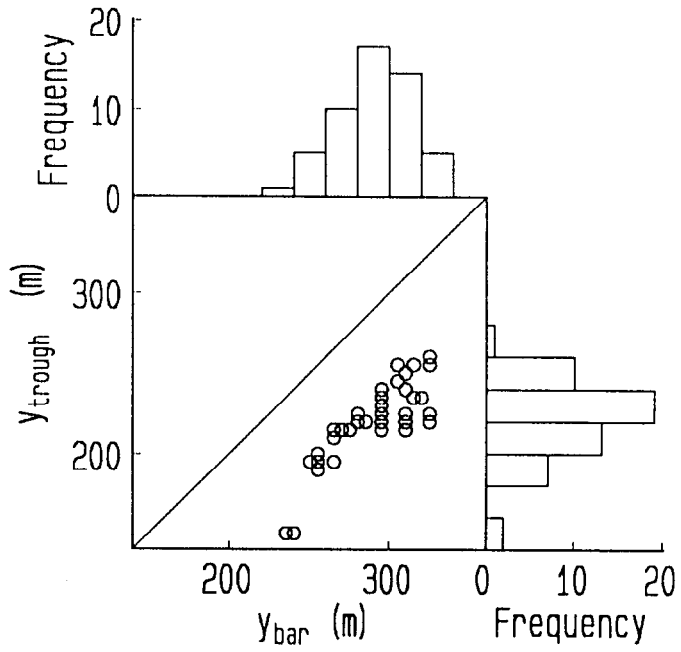

Figure 4.6 (1) Relationship between y_{bar} and y_{trough}, and their distributions.

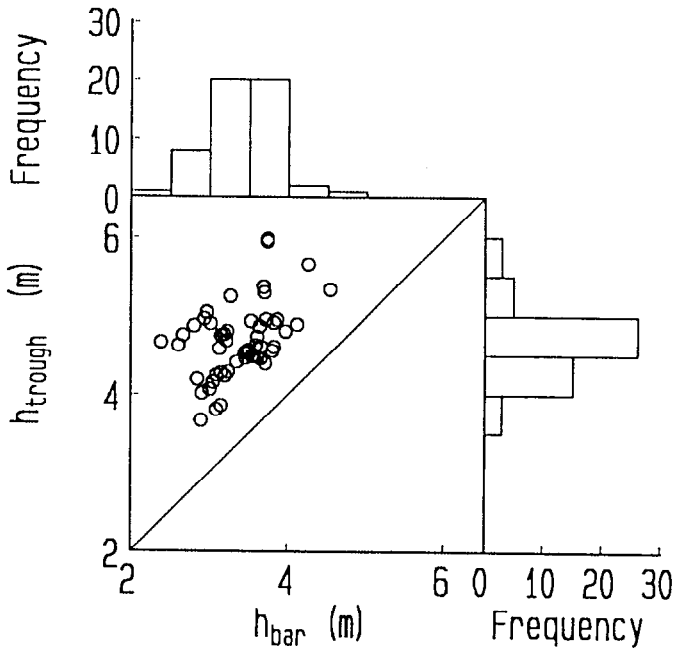

Figure 4.6 (2) Relationship between h_{bar} and h_{trough}, and their distributions.

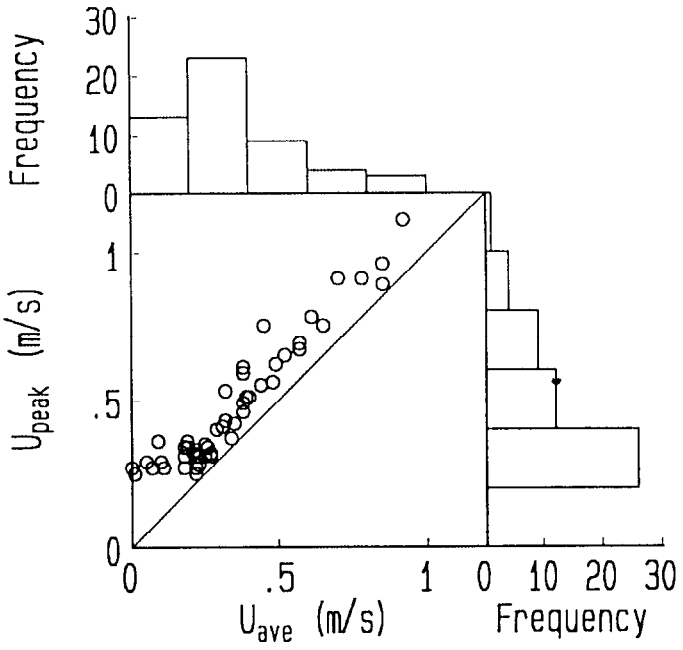

Figure 4.7 Relationship between U_{ave} and U_{peak}, and their distributions.

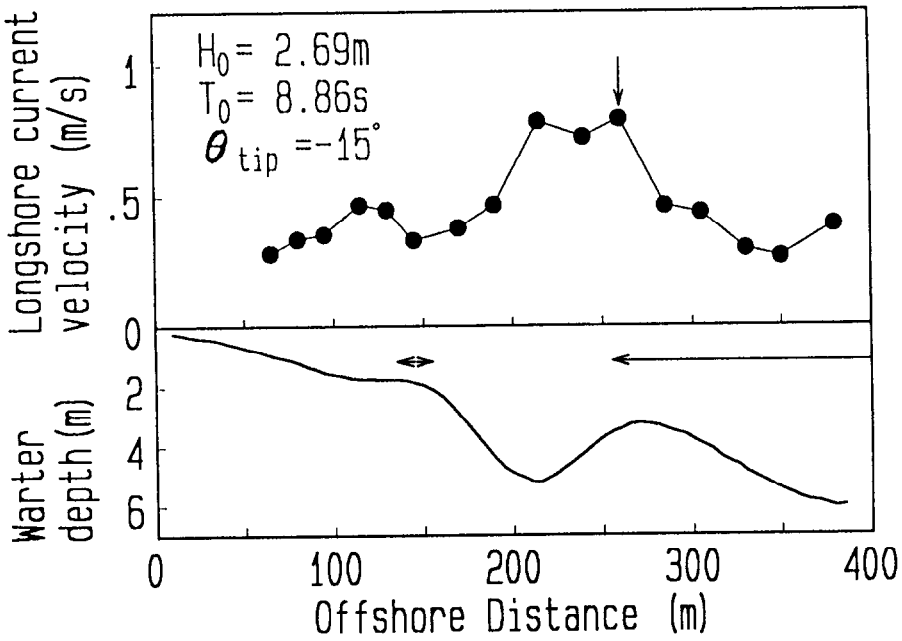

Figure 4.8 (1) Longshore current distribution and beach profile on March 28, 1989.

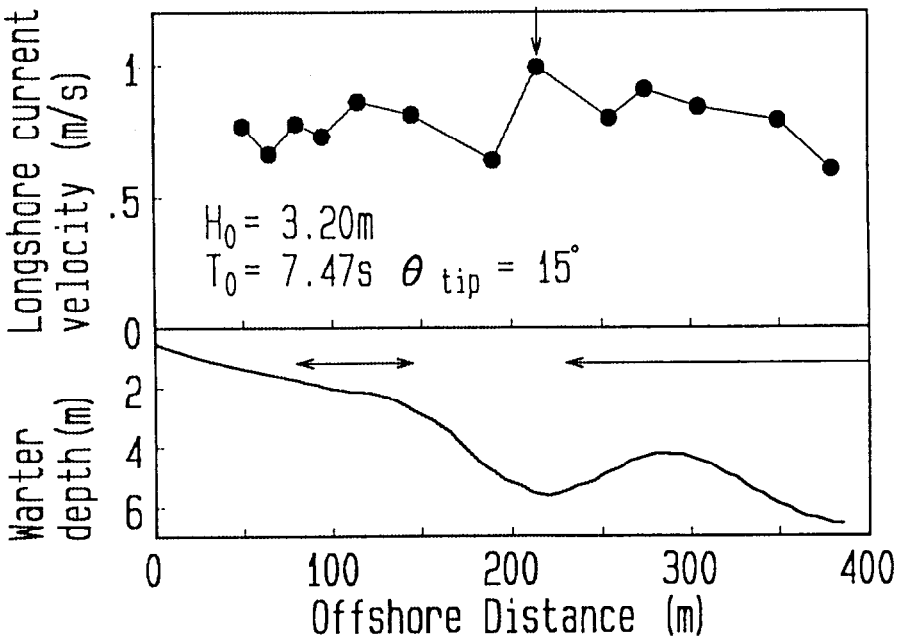

Figure 4.8 (2) Longshore current distribution and beach profile on November 28, 1987.

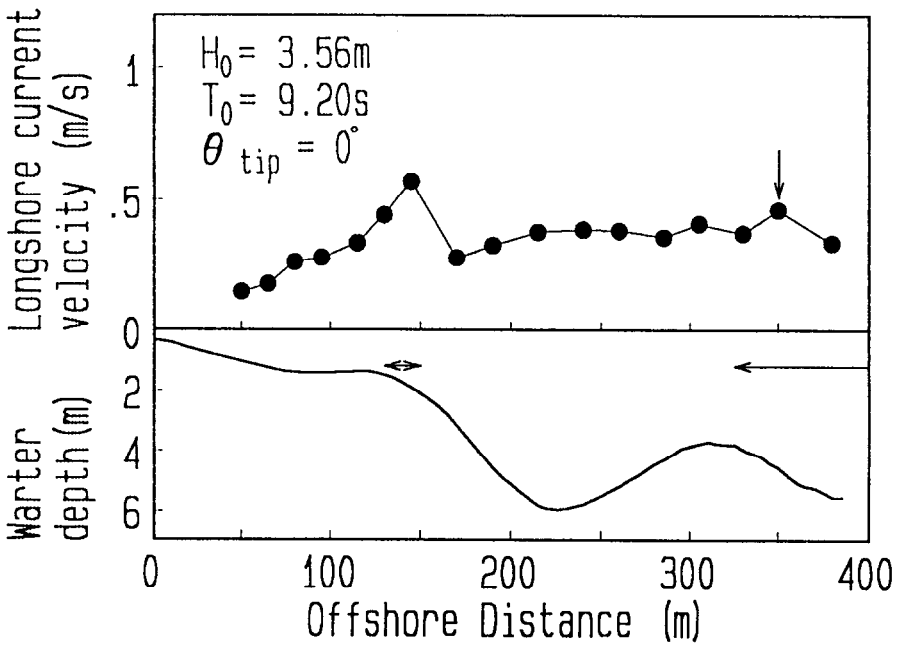

Figure 4.8 (3) Longshore current distribution and beach profile on May 12,1989.

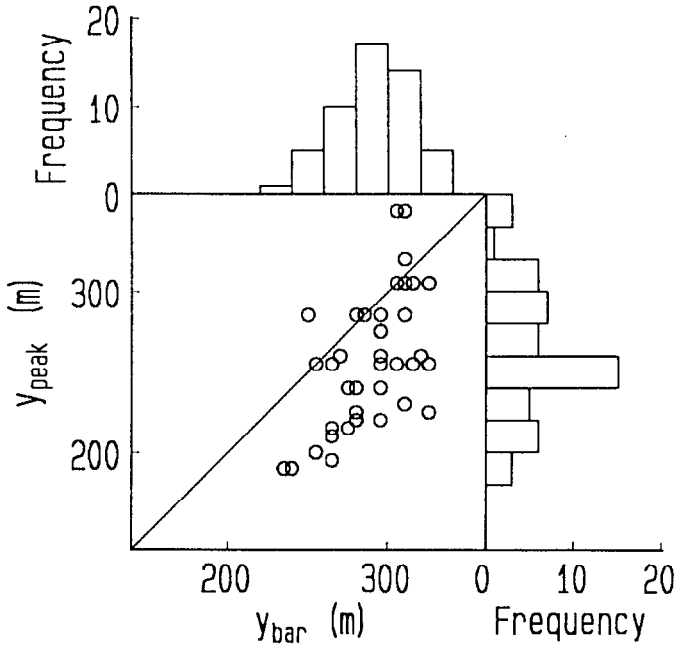

Figure 4.9 (1) Relationship between y_{bar} and y_{peak}, and their distributions.

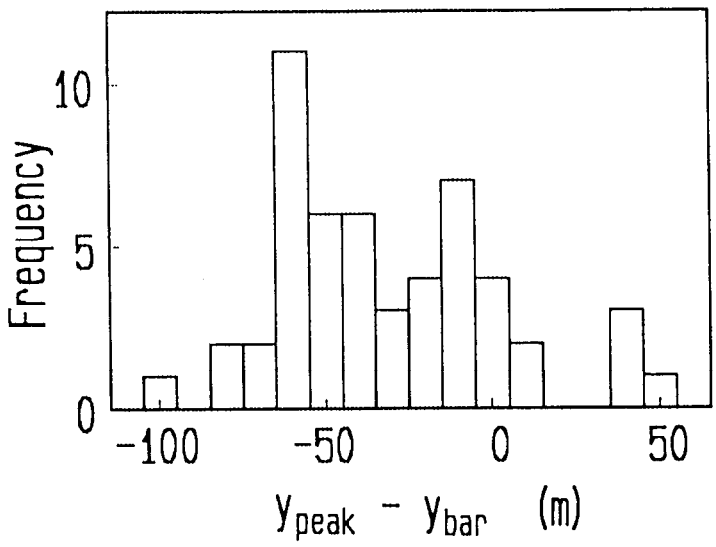

Figure 4.9 (2) Frequency distribution of the seaward distance from y_{bar} to y_{peak}.

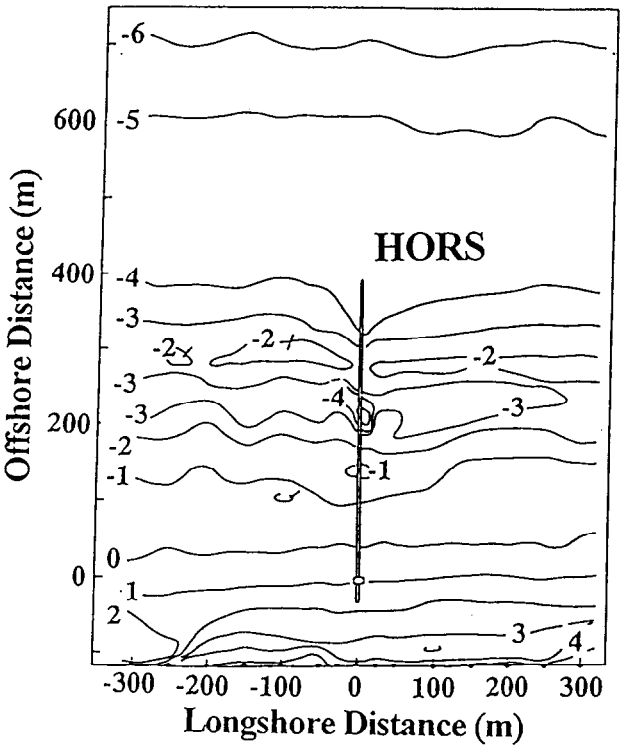

Figure 4.10 (1) Topographic map near HORS on March 31, 1989.

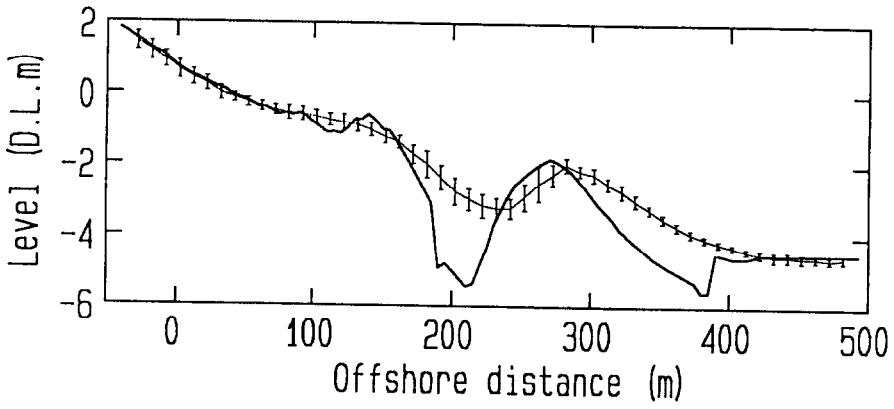

Figure 4.10 (2) Beach profile along HORS and the mean beach profile in the region between 100m to 300m from HORS.

Table 4.1 Offshore boundary conditions

Calculation date in 1989	$(H_{1/3})_{ob}$ (m)	$(T_{1/3})_{ob}$ (s)	θ_{ob} (degree)	$(S_{max})_{ob}$
March 24	3.20	11.20	-20.0	90
March 28	2.47	8.86	-25.0	40
April 4	2.03	8.40	-10.0	45

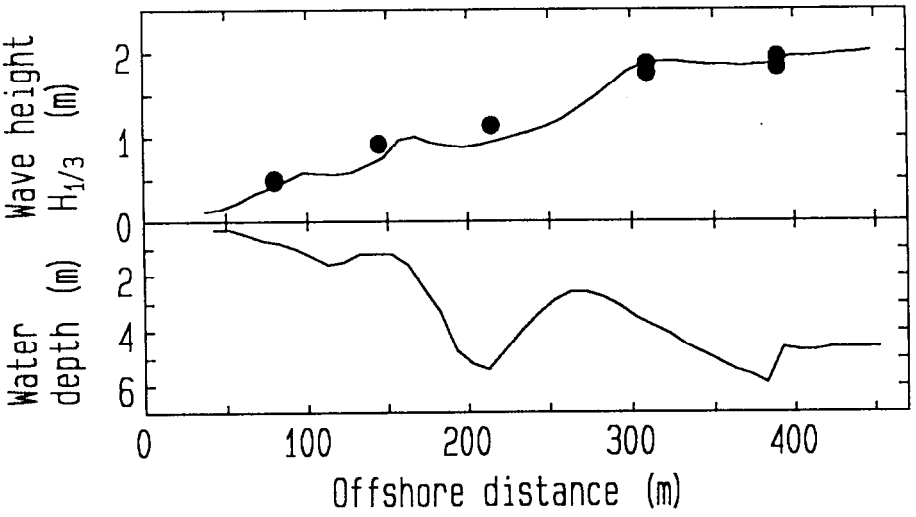

Figure 4.11 (1) Comparison between significant wave heights predicted by the present model and the values measured on March 24, 1989.

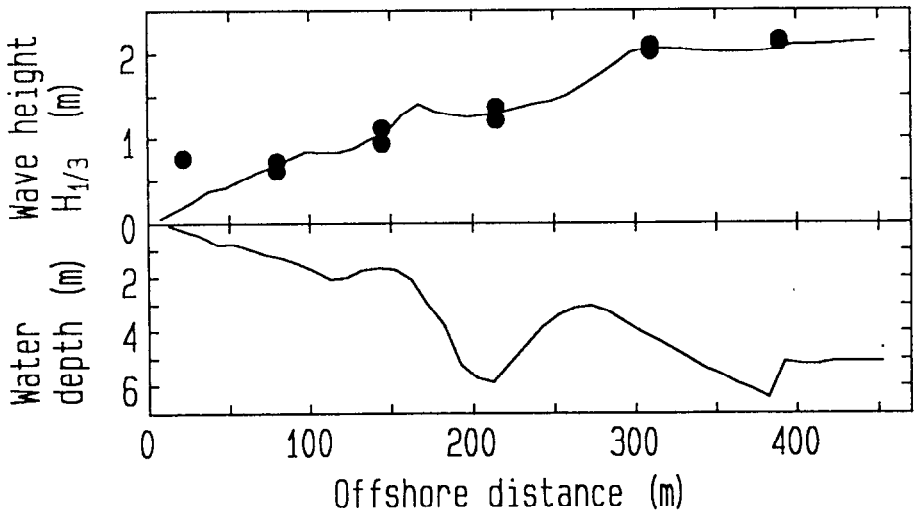

Figure 4.11 (2) Comparison between significant wave heights predicted by the present model and the values measured on March 28, 1989.

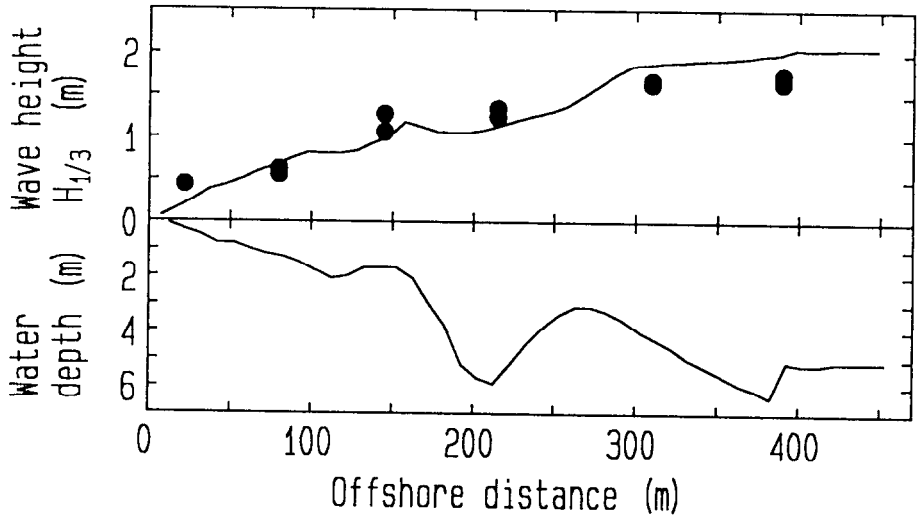

Figure 4.11 (3) Comparison between significant wave heights predicted by the present model and the values measured on April 4, 1989.

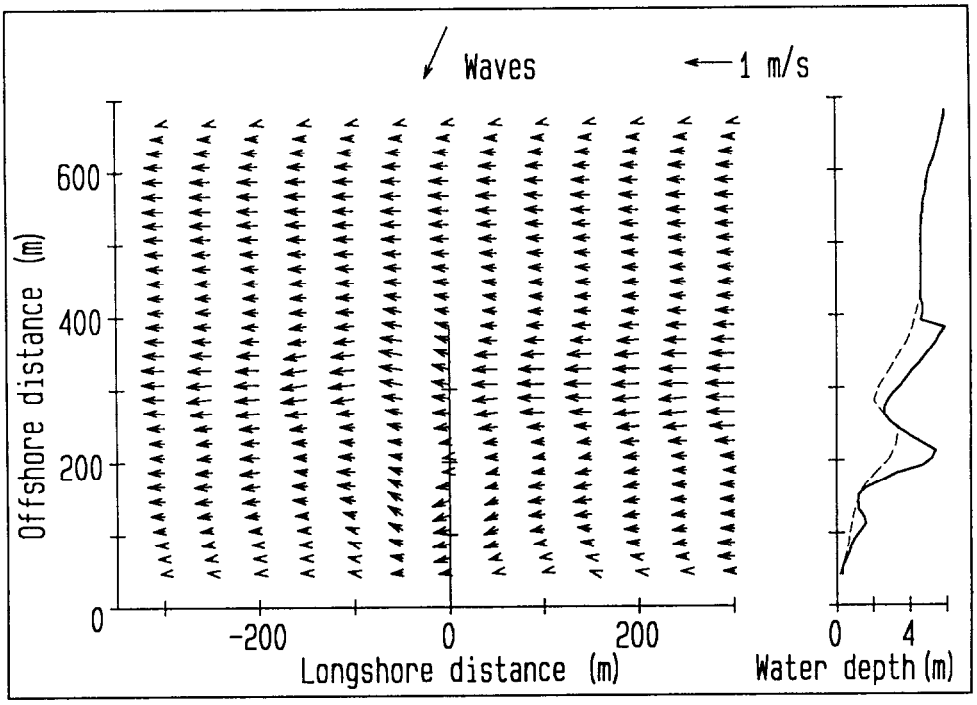

Figure 4.12 (1) Nearshore current on March 24, 1989, predicted by the present model with $M = 5$.

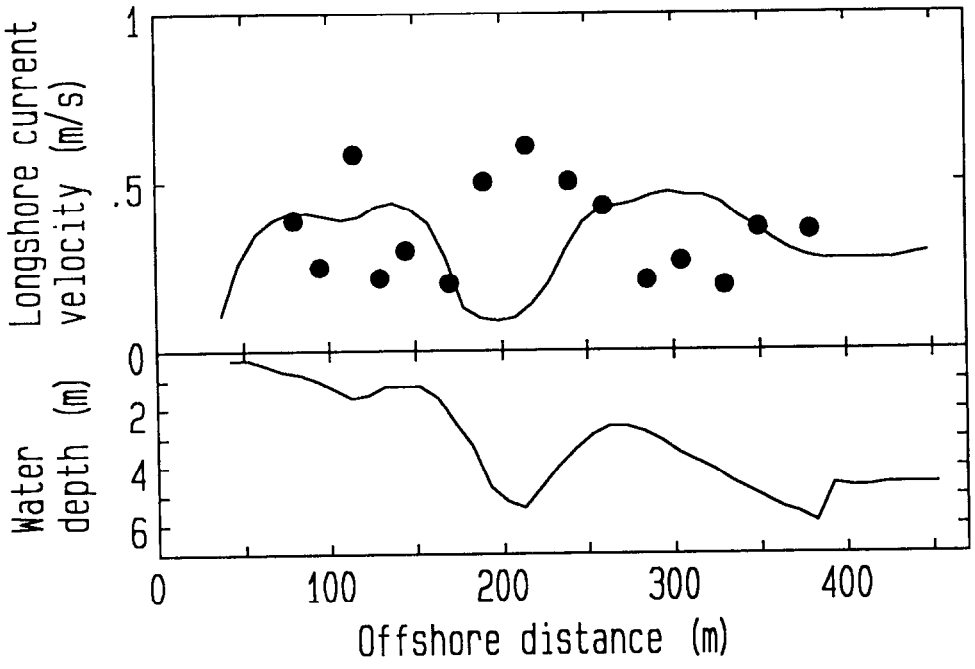

Figure 4.12 (2) Comparisons between the longshore current velocities measured on March 24, 1989, and those predicted by the present model.

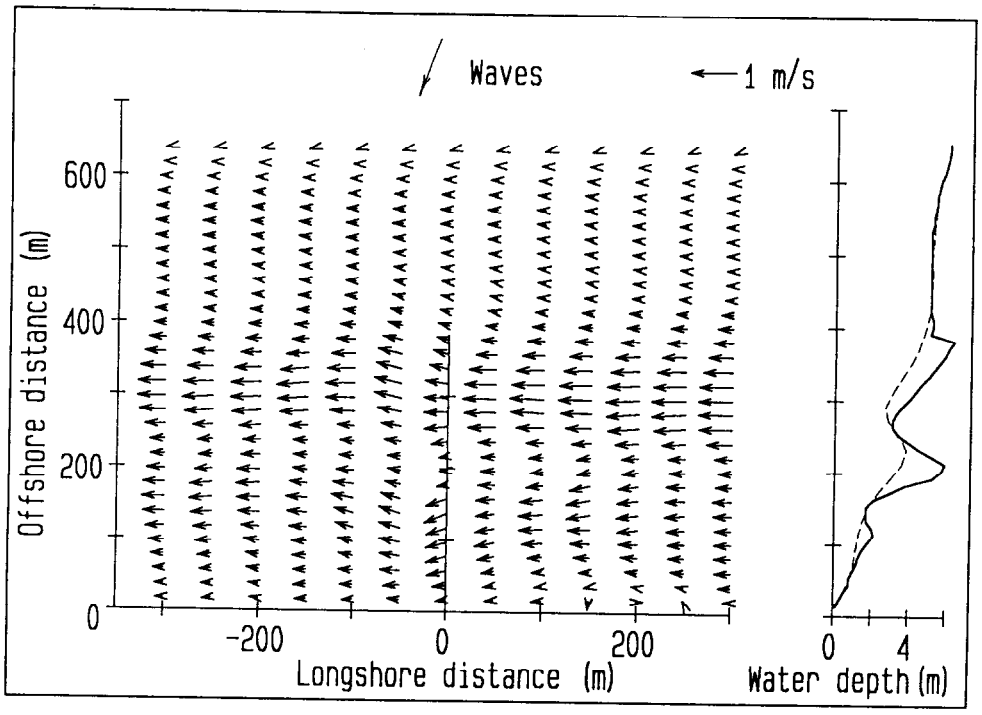

Figure 4.13 (1) Nearshore current on March 28, 1989, predicted by the present model with $M = 5$.

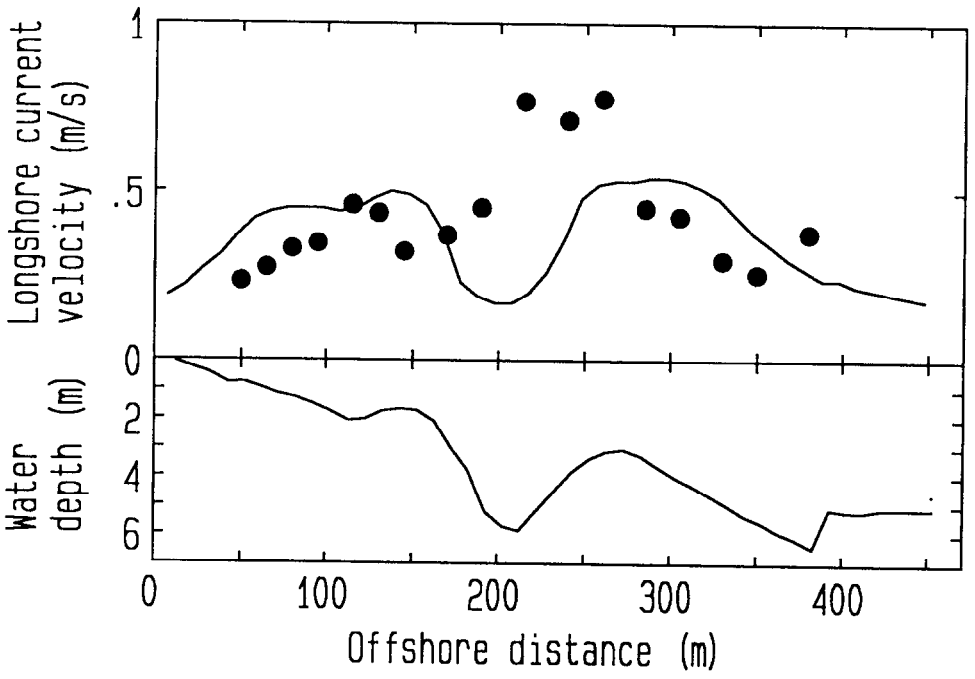

Figure 4.13 (2) Comparisons between the longshore current velocities measured on March 28, 1989, and those predicted by the present model.

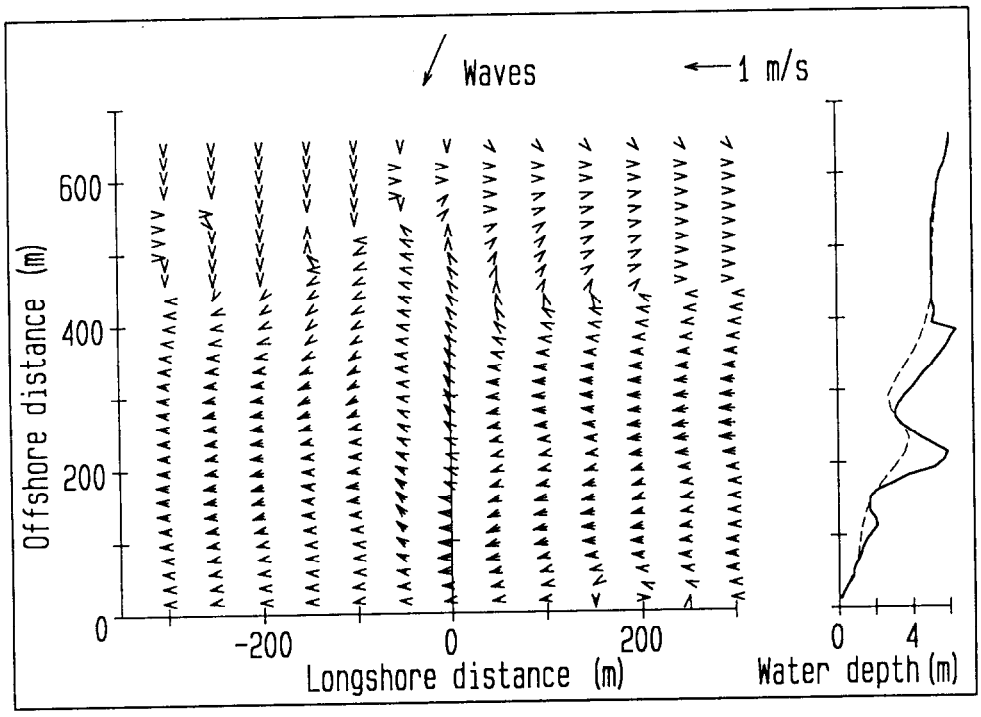

Figure 4.14 (1) Nearshore current on April 4, 1989, predicted by the present model with $M = 10$.

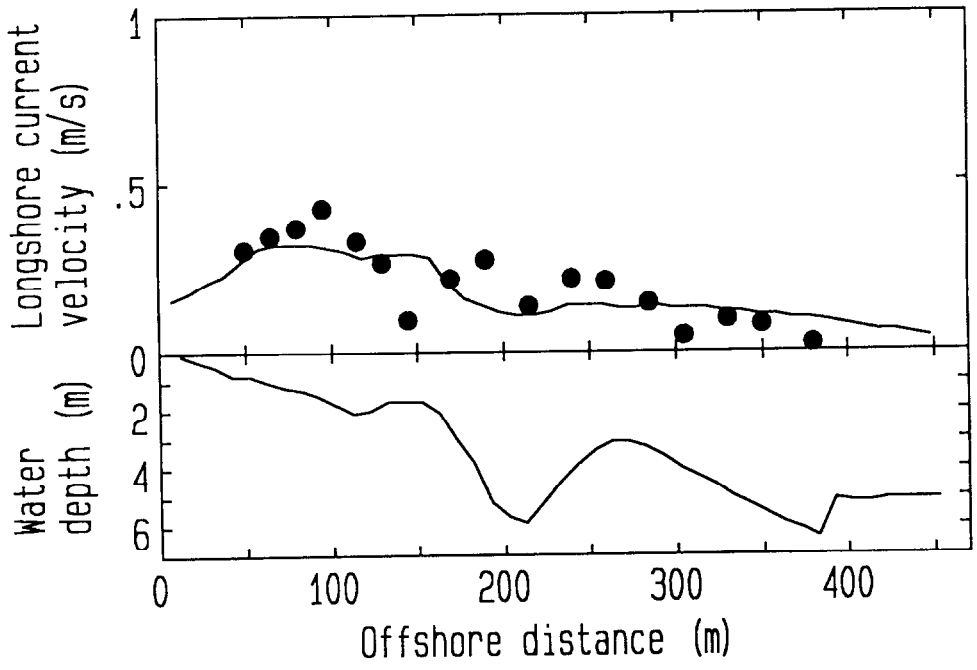

Figure 4.14 (2) Comparisons between the longshore current velocities measured on April 4, 1989, and those predicted by the present model.

5. Modeling of undertow and longshore current

5.1 Introduction

Nearshore currents below the wave trough level on barred beaches are often estimated with a conventional 2DH nearshore current model (e.g., Nishimura, 1988). In these models, the gradient of the radiation stress is the driving force of the nearshore current and the mass flux or the momentum flux due to bore, i.e., the surface roller, is not included. Church and Thornton (1993), Smith et al. (1993), Kuriyama and Ozaki (1993) and the investigation in Chapter 4, however, showed that the conventional model could not reproduce the cross-shore variation of the longshore current on a barred beach frequently observed in the field, which has a peak velocity shoreward of the bar crest.

De Vriend and Stive (1987) developed a quasi-3D nearshore current model, in which the surface roller effect is considered in the prediction of undertow velocity. The roller effect, however, is not included in the prediction of the horizontal current, and hence the model is unlikely to reproduce a maximum longshore current velocity located shoreward of the bar crest.

The roller effect has been included in predictive models for longshore current and nearshore current developed by Nadaoka et al. (1992), Okayasu et al. (1994), Kuriyama (1994), Reniers et al. (1995), Osiecki and Dally (1996), and Reniers and Battjes (1997). Kuriyama (1994) assumed in his 2DH model that the time-averaged cross-shore velocity in the roller is equal to the wave celerity and that the area of the roller is proportional to the square of the wave height as was also proposed by Svendsen (1984). Comparing the model with field measurements, Kuriyama (1994) showed that the model reproduced the typically observed cross-shore distributions of the longshore current velocity on a barred beach, in which peak velocities lie shoreward of the bar crests. The assumption used to estimate the roller area, however, was not directly verified with undertow velocity or wave setup data. Reniers et al. (1995) developed a longshore current model that includes the momentum flux due to the surface roller, and compared the model with experimental data and field data of the longshore current velocity. Although the model agreed well with the experimental data, the agreement between the model and the field data was poor. However, taking the alongshore gradient in the mean water level into account improved the agreement between the model results and the field data.

Reniers and Battjes (1997) calibrated the roller development model proposed by Stive and De Vriend (1994) with experimental data of wave setup, and incorporated it into their one-dimensional model for longshore current. They verified the longshore current model with data obtained in experiments that were designed not to generate a longshore gradient in the mean water level. On the basis of their simulation with and without the roller effect, they concluded that the surface roller contributes little to the production of a maximum velocity shoreward of the bar crest. They inferred that the maximum is mainly caused by the longshore gradient in the mean water level.

Okayasu et al. (1994) developed a quasi-3D nearshore current model based on the roller model developed by Okayasu et al. (1990), and confirmed the validity of the model by comparing it with an experiment on a planar beach. Osiecki and Dally (1996) used Dally and Brown's roller model (1995) to develop a one-dimensional longshore current model, which was verified with experimental data on a planar beach.

Although many models for nearshore current have been developed and verified with experimental data as described above, few models have been verified with field data. Furthermore, causes of the cross-shore variation of the longshore current on a barred beach in the field are not discussed on the basis of models verified with field data. In this Chapter, a one-dimensional model for undertow and longshore current is developed to predict the time- and depth-averaged current velocities below the wave trough level for the case where there is alongshore uniformity in depth, waves and current. The model is calibrated with field data obtained over longshore bars at HORS, and is verified with data from large-scale experiments and other field measurements.

5.2 Field measurements

Field measurements were conducted at HORS from January 29 to February 3, 1997. Cross-shore and longshore current velocities were measured with electro-magnetic current meters for thirty minutes every two hours at a sampling frequency of 5 Hz, and water surface elevations were measured with ultrasonic wave gages. Wave breaking positions and types, and the locations of rip currents were visually observed several times a day.

The locations of the measurement points are shown in Figure 5.1 with the beach profiles measured on January 31 and February 1. Seaward bar migration occurred on

January 31, when the bar crest moved seaward about 50 m. Except for the bar migration, no significant beach profile changes occurred during the measurements. The measurement point at P230m was located shoreward of the bar crest, while the measurement point of P290m was located seaward of the bar crest. The measurement point of P260m was located just seaward of the bar crest before the bar migration and shoreward of the bar crest after the bar migration.

The seaward bar migration on January 31 damaged the supporting systems of the current meters at all measurement points, and current velocities were temporarily not measured. At P260m, two current meters were installed on January 29 at D.L. -0.87 m and D.L. -1.37 m, and were reinstalled on February 1 after the damage at D.L. -1.09 m and D.L. -1.59 m. At P230m, one current meter was installed at D.L. -1.99 m and reinstalled at D.L. -1.90 m. At P290m, a current meter was installed at D.L. -1.72 m, but the support system of the current meter was completely destroyed at 7 a.m. on January 31. Consequently, current velocity measurements ceased at this locality.

Figure 5.2 shows time series of significant wave heights $H_{1/3}$, significant wave periods $T_{1/3}$, the mean undertow velocities V and the mean longshore current velocities U. The significant wave height at the tip of HORS (P380m), where the water depth was approximately 6 m, increased from 1.5 m at 11 p.m. on January 30 to about 2.6 m at 8 a.m. on January 31, and then gradually decreased. The undertow velocities increased as the wave heights increased, and after February 1 they fluctuated independently of the wave height variations.

The nearshore currents are considered to be uniform alongshore during the time that the measurements were made for two reasons. First, during the visual observations, which were conducted several times a day during the measurements, no rip currents were observed, and the breaker lines were linear alongshore. Second, the low-frequency components of the cross-shore current velocities $v_{rms,l}$ (<0.04 Hz) were not correlated with the undertow velocities as shown in Figure 5.3. Instead, the low-frequency components were relatively constant, whereas the undertow velocities changed significantly. Some previous field measurements revealed that rip currents are intermittent events (Wright and Short, 1983; Short, 1985, Smith and Largier, 1995), and hence the low-frequency component of the cross-shore current in or in the vicinity of a rip current is expected to be large. The constant low-frequency components of the

cross-shore currents in Figure 5.3 suggest a low probability of rip current generation during the measurements.

5.3 Numerical model

The model developed in this chapter consists of a wave transformation model, an undertow model and a longshore current model, and adopts a wave-by-wave approach. In this approach, wave heights, undertow velocities and longshore current velocities are calculated for individual waves.

5.3.1 Wave transformation model

The wave transformation model is based on the model developed in Chapter 3, which calculates the shoaling, breaking and reforming of individual waves. The shoaling of a wave is estimated with a shoaling coefficient proposed by Shuto (1974) with consideration for wave nonlinearity. The criterion for wave breaking is based on Eq. (3.6), which was proposed by Seyama and Kimura (1988). Energy dissipation of the organized wave motion in the surf zone, which is the source of the energy of the surface roller described in section 5.3.2, is estimated with the periodic bore model used by Thornton and Guza (1983), expressed by Eq. (3.8). The location of wave reforming, where the wave energy dissipation stops and a breaking wave becomes the non-breaking wave, is determined using $H_r/h_r = 0.35$.

For a given significant wave height and period at an offshore boundary, a ten minutes time series of water surface elevation having the JONSWAP type spectrum is numerically simulated using a peak enhancement factor γ of 3.3. With the zero-down crossing method, the time series is divided into individual waves, which are then used in the calculation.

The incident directions of individual waves at the offshore boundary are determined using the given principal wave direction, the directional spreading function of Mitsuyasu-type and the spreading parameter estimated with the method of Goda and Suzuki (1975). When the spreading parameter exceeds 100, the individual waves are treated as uni-directional waves.

In all calculations in this chapter, in order to minimize the error in the prediction of undertow and longshore current velocities caused by the error in the prediction of wave

height, coefficients C_{br} and C_B were included in Eq. (3.6) for wave breaking and Eq. (3.8) for energy dissipation, respectively. Their values are those that allow the predicted significant wave heights to equal the measured values. The modified forms of Eqs. (3.6) and (3.8) are Eqs. (5.1) and (5.2), respectively. The fitting resulted in values of C_{br} ranging from 0.7 to 1.2 and C_B ranging from 0.7 to 1.1.

$$\frac{H_b}{h_b}=C_{br}\left[0.16\frac{L_0}{h_b}\left[1-\exp\left\{-0.8\pi\frac{h_b}{L_0}(1+15\tan^{4/3}\beta)\right\}\right]-0.96\tan\beta+0.2\right] \tag{5.1}$$

$$B=C_B\{1.6-0.12\ln(H_0/L_0)+0.28\ln(\tan\beta)\} \tag{5.2}$$

5.3.2 Undertow model

The time- and depth-averaged undertow velocity of an individual wave V_{ind} is estimated with the volume flux due to the organized wave motion Q_w and that due to the surface roller Q_r.

$$V_{ind}=-(Q_w+Q_r)/d_{tr}, \tag{5.3}$$

where d_{tr} is the distance between the wave trough level and the bottom, and is simply determined as $d_{tr} = h - H/2$.

The volume flux due to the organized wave motion Q_w is calculated with the wave celerity C, the water depth h, and the root-mean-square of water surface elevation of an individual wave ζ_{rms} by the following equation proposed by Svendsen (1984).

$$Q_w=-(C/h)\zeta_{rms}^2. \tag{5.4}$$

The value of ζ_{rms} is estimated with consideration for the wave nonlinearity. With the parameter Π expressing nonlinearity of an individual wave proposed by Goda (1983), the relationship between ζ_{rms} and H was obtained on the basis of experimental data shown by Goda (1983); the parameter Π and the relationship obtained are expressed by

$$\Pi = H/L\coth^3(2\pi h/L), \tag{5.5}$$

and

$$\zeta_{rms} = \frac{1}{2\sqrt{2}} H, \qquad \Pi < 0.15,$$

$$\zeta_{rms} = \frac{1}{1.668 \log \Pi + 4.204} H, \quad 0.15 \le \Pi < 3, \tag{5.6}$$

$$\zeta_{rms} = \frac{1}{5} H, \qquad \Pi \ge 3.$$

In the estimation of Q_r, it was assumed that the vertical distribution of the time-averaged cross-shore velocity was like that shown in the middle of Figure 5.4. In previously proposed models (e.g., Svendsen, 1984), the vertical distribution shown in the left of Figure 5.4 was assumed; the time-averaged velocity in the surface roller is equal to C. The justification for the choice of vertical distribution used in this study is as follows: just behind the front of the surface roller, the cross-shore velocity near the wave trough level sharply changes from a shoreward velocity equal to C to a seaward undertow velocity. However, the cross-shore velocity in the middle of the surface roller probably changes gradually from the top to the wave trough level owing to large eddies reported by Nadaoka et al. (1989). These eddies have shoreward velocity near the surface and seaward velocity near the wave trough. Hence, the vertical distribution shown in the middle of Figure 5.4 is assumed in the present model, and accordingly the volume flux due to the surface roller is obtained from

$$Q_r = -A_r C / (2L), \tag{5.7}$$

where A_r is the area of the surface roller.

For estimating the area of the surface roller, two methods have been proposed. One method assumes that the area of the surface roller is proportional to the square of the wave height (e.g., Svendsen, 1984; Okayasu et al., 1988). The other assumes that the energy of the organized wave motion is transferred without any loss to the energy of the surface roller owing to wave breaking, and then the surface roller energy is dissipated (e.g., Okayasu et al., 1990; Dally and Brown, 1995); the area of the surface roller is estimated with the following equation.

$$\frac{\partial (E_w C_g)}{\partial y} + \frac{\partial (E_r C)}{\partial y} = D_p, \tag{5.8}$$

where E_r is the energy of the surface roller, and D_p is the dissipation term of the surface roller energy.

In the present model, the area of the surface roller is estimated using a combination of

the two methods on the basis of assumptions described below.

(a) The area of the surface roller is basically assumed to be proportional to the square of the wave height. The area A_{r1} is estimated with a dimensionless coefficient C_A from

$$A_{r1} = C_A H^2. \tag{5.9}$$

(b) The energy of the surface roller, however, should not exceed the energy transferred from the organized wave motion. The roller area is therefore determined not to exceed the roller area A_{r2} that is from the following equation estimated without considering energy dissipation of the surface roller.

$$\begin{aligned} &\frac{\partial(E_w C_g)}{\partial y} + \frac{\partial(W_r C)}{\partial y} = 0, \\ &W_r = \frac{1}{8}\rho C^2 \frac{A_{r2}}{L}, \end{aligned} \tag{5.10}$$

where W_r is the energy of the roller having the triangle-shaped distribution of the time-averaged velocity above the wave trough level shown in Figure 5.4. The decrease of the wave energy E_w is estimated with Eq. (3.8).

(c) The surface roller diminishes at the wave reforming point.

In the actual calculation, A_{r1} and A_{r2} are estimated and the smaller value is assumed to be the area of the surface roller.

5.3.3 Longshore current model

The time- and depth-averaged longshore current velocity of an individual wave U_{ind} is estimated on the basis of the balance among the bottom friction F_{x1}, the lateral mixing force L_{x1}, the gradient of the radiation stress R_{x1}, and the gradient of the momentum flux due to the surface roller M_{x1}; the balance is expressed by

$$F_{x1} - L_{x1} + R_{x1} + M_{x1} = 0. \tag{5.11}$$

The bottom friction is estimated with the following equation, which is proposed by Nishimura (1988), as in Chapter 4.

$$\begin{aligned} &F_{x1} = \frac{C_f}{h}\left(W + \frac{{w_b}^2}{W}\sin 2\theta\right)U_{ind}, \\ &W = \left(\sqrt{U_{ind}^2 + w_b^2 + 2U_{ind}w_b\sin\theta} + \sqrt{U_{ind}^2 + w_b^2 - 2U_{ind}w_b\sin\theta}\right)/2, \\ &w_b = 2v_m/\pi, v_m = \pi H/(T\sinh(2\pi h/L)), \end{aligned} \tag{5.12}$$

where C_f is a friction coefficient, and is set to equal to 0.005 as in Kuriyama and Ozaki

(1993).

The lateral mixing term L_{x1} is estimated using

$$L_{x1} = \frac{\partial}{\partial y}(\varepsilon_1 \frac{\partial U_{ind}}{\partial y}),$$
$$\varepsilon_1 = Mh(\frac{D_1}{\rho})^{1/3}, \quad D_1 = \frac{\partial(E_w C_g)}{\partial y} + \frac{\partial(E_r C)}{\partial y}, \tag{5.13}$$

where ε_1 is the lateral mixing coefficient defined as Battjes (1975) and M is a dimensionless coefficient, which is set to equal to 5 as in Kuriyama and Ozaki (1993) and in Chapter 4. The value of ε was estimated using the total energy dissipation, which is the sum of the energy dissipation of the organized wave motion and that of the surface roller.

The radiation stress term R_{x1} is estimated on the basis of the small amplitude theory by

$$R_{x1} = \frac{1}{\rho h}(\frac{\partial S_{yx1}}{\partial y}), \quad S_{yx1} = \rho g \frac{C_g}{C}\frac{1}{8}H^2 \cos\theta \sin\theta. \tag{5.14}$$

The gradient of the momentum flux M_{x1} is expressed by Eq. (5.15), in which M_{r1} is the momentum flux due to the surface roller having the triangle-shaped distribution of time-averaged velocity.

$$M_{x1} = \frac{1}{\rho h}(\frac{\partial M_{r1}}{\partial y}), \quad M_{r1} = -\frac{1}{3}\rho C^2 \frac{A_r}{L}\cos\theta \sin\theta. \tag{5.15}$$

5.4 Calibration

In the present model, C_A in Eq. (5.9) is a key coefficient for estimating the area of the surface roller. Hence, the model was calibrated with the field data from fourteen cases obtained at HORS from 11 p.m. on January 30 to 10 a.m. on February 2 in 1997, when the wave heights were large.

The offshore boundary was set at P640m. The beach profiles used in this calibration consist of two parts: the beach profiles shoreward and seaward of the tip of HORS (P380m). For shoreward ones, the beach profiles measured daily along HORS were used, and for seaward ones, the beach profile surveyed on January 16, 1997 shown in Figure 5.5 was used. According to Kuriyama (1996) and as was discussed in Chapter 2, the amount of beach profile changes seaward of the tip of HORS is considered to be small.

The wave heights at the offshore boundary were estimated from the offshore wave data, which were obtained at a water depth of about 23.4 m offshore of Kashima Port. The wave directions at the offshore boundary were calculated with the Snell's law from the principal wave directions measured at P260m.

The value of C_A optimal for all cases was 7. On the other hand, the value of C_A optimal in each case was related to the surf similarity parameter at the wave breaking position ξ_b. The parameter ξ_b is estimated by

$$\xi_b = \tan\beta / (H_{1/3,b} / L_{1/3,0})^{1/2}, \tag{5.16}$$

where $H_{1/3,b}$ is the significant wave height at the wave breaking position and $L_{1/3,0}$ is the offshore wavelength corresponding to the significant wave period. The value of $H_{1/3,b}$ was defined as the maximum of the significant wave heights over a longshore bar, and was obtained from the calculation results of wave transformation. The beach slope used in Eq. (5.16) is the value at the point where $H_{1/3,b}$ is defined.

Figure 5.6 shows the relationship between ξ_b and the optimal value of C_A for each case. As reported by Dibajnia et al. (1994), there is a positive correlation between these parameters with a correlation coefficient of 0.61. The value of C_A increases as ξ_b increases, meaning that the coefficient increases as more waves break in plunging breakers.

The relationship between C_A and ξ_b obtained with the least squares method is given by

$$C_A = 17.0 \log \xi_b + 24.7, \tag{5.17}$$

and is shown by a solid line in Figure 5.6.

Undertow velocities predicted with C_A given by Eq. (5.17) and with C_A=7 were compared with the values measured at HORS; the cross-shore interval in the calculations was 10 m. Because ξ_b in the measurements ranged from 0.3 to 0.5, the values of C_A larger than 12 and those smaller than 4 were set equal 12 and 4, respectively. The values predicted with a model that has been proposed by Stive and De Vriend (1994) and calibrated by Reniers and Battjes (1997) were also compared with the measurements; the model of Stive and De Vriend will be referred to as the S&DV model.

Figure 5.7 shows comparisons for six out of the fourteen cases used in the calibration.

The significant wave heights, periods, principal wave directions θ, water depths and mean water levels $\bar{\eta}$ at the offshore boundary, and ξ_b in the cases are listed in Table 5.1. Note that the values of s_{max} at the offshore boundary exceeded 100. As shown in Figure 5.7, the S&DV model, which has been calibrated with experimental data, underestimated the undertow velocities. Both models with C_A agreed with the measurements, though the performance of the model with C_A given by Eq. (5.17) was better than that with the constant C_A.

Figure 5.8 shows the relationships between the undertow velocities measured V_{meas} and predicted V_{pred} for all cases. The upper figure shows the values predicted with the S&DV model, and the middle and lower figures show the values predicted with the present model having constant C_A and with the present model having C_A given by Eq. (5.17), respectively. The tendency of the S&DV model to underestimate the undertow velocities is also shown in the upper figure.

The root-mean-square errors defined by

$$\varepsilon_r = \left(\frac{\sum (V_{meas} - V_{pred})^2}{\sum (V_{meas})^2} \right)^{1/2}, \tag{5.18}$$

were calculated for the fourteen cases used in the calibration. The values of ε_r for the S&DV model and the present models with C_A =7 and C_A given by Eq. (5.17) were 52%, 41% and 35%, respectively

5.5 Verification

5.5.1 Undertow model

The undertow models with C_A given by Eq.(5.17) and with C_A =7, and the S&DV model were also compared with the field measurement of DELILAH (Smith et al., 1992) and the large-scale experiments of Delta Flume '93 Experiments (Sanchez-Arcilla et al., 1994; Rakha et al., 1996). The data on October 19, 1990 in DELILAH and cases 1-b and 1-c in the Delta Flume '93 Experiments were used for comparisons. The cross-shore intervals in the calculations were set to be 5 m for DELILAH and 1 m for Delta Flume '93 Experiments. The wave heights, periods, principal wave directions and water depths at the offshore boundaries are listed in Table 5.2, where T_p is the wave period at the spectral peak. The parameter s_{max} exceeded 100 on October 19 in

DELILAH.

Figure 5.9 shows the comparison between the models and the measurement from DELILAH. The S&DV model underestimated the velocities, but both of the models with C_A agreed with the field data. The comparisons between the models and the measurements in the Delta Flume '93 Experiments are shown in Figure 5.9. The S&DV model agreed with the measurements, whereas both models with C_A overestimated the undertow velocities. The performance of the model with C_A given by Eq. (5.17) was better than that of the model with the constant C_A.

5.5.2 Longshore current model

The longshore current model with C_A given by Eq. (5.17) was verified with the field data from the fourteen cases used in the calibration for the present undertow model. The measurements were also compared with two longshore current models: the first proposed by Reniers and Battjes (1997), where the surface roller development is estimated using Stive and De Vriend's model (1994), and the second that excludes the surface roller effect. The first and the second models will be referred to as the R&B model and the no-roller model, respectively. Figure 5.11 shows cross-shore variations of the longshore current velocities predicted with the present model, the R&B model and the no-roller model, and those measured at HORS. Although all the models agreed with the measurements over the longshore bars, the present model was not fully validated because the number of measurement points was limited; it is not clear whether the present model can reproduce the cross-shore variation of the longshore current velocity on a barred beach with a peak velocity shoreward of the bar crest. Hence, the present longshore current model was verified using the cross-shore distributions of the longshore current velocity measured at HORS on March 24, 28 and April 4 in 1989 (shown in Chapter 4) and the distribution measured at 1 a.m. on October 14 in the DELILAH project (Smith et al., 1993).

In the measurements at HORS in 1989, the longshore current velocities were measured with a float; the accuracy of the measurements with the float was verified with an electromagnetic current meter. Topography surveyed on March 31, 1989, near HORS was nearly uniform alongshore (Figure 4.10). The horizontal nearshore current near HORS calculated with a conventional nearshore current model was relatively

uniform alongshore and did not have a rip current (Figures 4.12 to 4.14). In the DELILAH project, topography in the investigation area on October 14 was also nearly uniform alongshore (Smith et al., 1993). Hence, the effect of the alongshore gradient in the mean water level on longshore current in those cases is considered to be small.

The cross-shore intervals in the calculations were 10 m for HORS and 5 m for DELILAH. The offshore boundary conditions in the measurements at HORS and in the DELILAH project are listed in Table 5.3; the parameter s_{max} exceeded 100 in the DELILAH measurement.

Figure 5.12 shows the comparisons of longshore current velocities measured at HORS in 1989 and those predicted with the present model, the R&B model and the no-roller model. The cross-shore variations of the longshore current velocity predicted with the R&B model and the no-roller model have peak velocities seaward of the bar crests, which disagree with the measured variations. The present model, however, agrees with the measurements and reproduces the cross-shore distributions of longshore current over longshore bars in the field, which have peak velocities shoreward of the bar crests. One possible reason for the discrepancies between the present model and the measurements near the shorelines in cases 89-1 and 89-2 is an error in the measurements. In a measurement of longshore current in shallow water area with a float, the float sometimes touches the bottom, causing the measured velocity to be smaller than the real value. This error is considered to be a cause of the discrepancies.

A comparison between the models and the measurement of DELILAH is shown in Figure 5.13; the predictions were conducted with $M = 5$. The present model reproduces the observed cross-shore variation of the longshore current velocity on the barred beach, which has a maximum velocity shoreward of the bar crest.

5.6 Discussion

Through the comparisons between the models and the measurements, it is evident that the model with C_A given by Eq. (5.17) provided better predictions than that with the constant C_A equal to 7 for undertow velocities on longshore bars in the field where water depth ranges from 2 to 4 m. The positive relationship between C_A and ξ_b, shown in Figure 5.5, was also reported by Deigaard et al. (1991) and Dibajnia et al. (1994). Deigaard et al. (1991) reported on the basis of the Engelund model that C_A increases as

the wave height-water depth ratio increases. The wave height-water depth ratio in the surf zone increases as the wave steepness in deep water decreases and as the beach slope gets steeper. Because ξ_b also increases as the wave steepness decreases and as the beach slope gets steeper, the relationship between C_A and the wave height-water depth ratio reported by Deigaard et al. (1991) is considered to be qualitatively the same as the relationship between C_A and ξ_b shown in this study. Dibajnia et al. (1994) also showed a positive correlation between C_A and ξ_b on the basis of undertow velocities obtained by Kuriyama (1991) in the secondary breaker zone at HORS, where water depth ranged from 1 to 4 m.

According to Eq. (5.17), the value of C_A ranges from 4 to 12 when ξ_b ranges from 0.3 to 0.5. When C_A' is defined as the dimensionless coefficient in Eq. (5.9) for the rectangular-shaped distribution of the time-averaged cross-shore velocity above the wave tough level, $C_A'=C_A/2$ yields the same undertow velocity as C_A. Hence, C_A ranging from 4 to 12 is equivalent to C_A' ranging from 2 to 6. Shimizu et al. (1994) conducted field measurements at a water depth of 5 m and showed that C_A' ranged from 4 to 7. On the basis of field data obtained by Kuriyama (1991), mentioned above, Dibajnia et al. (1994) found the relationship of $C_A'=22\xi_b$; for ξ_b ranging from 0.3 to 0.5, C_A' ranges from 6.6 to 11. The values of C_A' obtained on the basis of field data by Shimizu et al. (1994) and Dibajnia et al. (1994) are approximately equal to or larger than C_A' in this study. On the other hand, with data obtained in small-scale experiments and simulation results, Svendsen (1984), Okayasu et al. (1988) and Deigaard et al. (1991) showed smaller values of C_A': 0.9 by Svendsen (1984), 2.3 by Okayasu et al. (1988) and 0.6 to 1.4 with H/h ranging from 0.4 to 1.0 by Deigaard et al. (1991). The difference between the values of C_A' in the field and those in small-scale experiments seems to be attributable to scale effects; the relative size of the vortex and the development of the surface roller in the field are considered to be different from those in small-scale experiments. Chapter 3 discussed the wave height-water depth ratio at the wave reforming point in the field, and showed that the ratio in the field was smaller than that in the laboratory. This result means that the surface roller in the field exists longer than that in the laboratory, and this is likely caused by the difference between the development of the vortex generated by wave breaking in the field and in the laboratory.

The S&DV model sometimes underestimates the undertow velocities observed in the

field. Figure 5.14 shows a comparison among the measured undertow velocities in case 5, those predicted with the present model having C_A given by Eq. (5.17), and those predicted with a modified S&DV model which assumes no energy dissipation. The S&DV model with no energy dissipation still underestimated the undertow velocities. This result seems to suggest that the assumption of the rectangular-shaped distribution of the time-averaged velocity above the wave trough level, shown in the left of Figure 5.4, is inappropriate. However, undertow models based on the energy transfer from the organized wave motion to the surface roller and the rectangular-shaped distribution of the time-averaged velocity like the S&DV model agree well with experimental data (e.g., Dally and Brown, 1995). More investigations on the development of the surface roller and the vortex generated by wave breaking are required in the laboratory and in the field.

In the longshore current model, C_f is set to be 0.005 as in Kuriyama and Ozaki (1993) and in Chapter 4. As mentioned in Chapter 4, the value of 0.005 was determined by Kuriyama et al. (1992) to give a best fit to the longshore current velocities in the 162 cases measured at HORS. Smith et al. (1993) used the Manning friction coefficient estimated with

$$c_f = g(n^2 / h^{1/3}), \tag{5.19}$$

where n is the Manning resistance coefficient. When the Manning resistance coefficient is assumed to be 0.02 as in Smith et al. (1993), and the water depth is assumed to be 2 to 4 m, C_f estimated with Eq. (5.19) becomes 0.002 to 0.003. Faria et al. (1996) reported on the basis of vertical distributions of the longshore current velocity measured in the field that C_f was on the order of 0.001 on bar crests and about 0.005 on troughs. Since the value of 0.005 used in the present model is similar to C_f previously used and reported, the value of 0.005 is considered to be reasonable, though the accurate estimation of the cross-shore variation of C_f is still an unsolved problem.

Reniers and Battjes (1997) concluded that the cross-shore variation of the longshore current velocity on a barred beach having a peak velocity shoreward of the bar crest, which is frequently observed in the field (Chapter 4), is mainly caused by the longshore gradient in the mean water level, and not by the surface roller. This conclusion, however, has been derived on the basis of simulation results with a model verified only with experimental data. Although the longshore gradient in the mean water level is still one

of the causes of the cross-shore distribution with a peak shoreward of the crest, the present model, calibrated with field data, can produce a maximum velocity located shoreward of the bar crest even without the longshore gradient in the mean water level. This result shows that the surface roller can produce the cross-shore distribution often observed in the field.

In a longshore current model without the surface roller, the cross-shore gradient of the radiation stress is the only driving force of the longshore current, and hence the longshore current calculated with the model has a peak velocity seaward of the bar crest, where waves break and the cross-shore gradient of the radiation stress is large. On the other hand, in a longshore current model with the surface roller effect, the driving forces of the longshore current are the cross-shore gradient of the radiation stress and that of the momentum flux due to the surface roller. The energy of the organized wave motion is first transferred to the surface roller energy, and then the energy is dissipated. Accordingly, the peak of the cross-shore gradient of the momentum flux due to the surface roller is located shoreward of the peak of the gradient of the radiation stress as shown in Figure 5.15. As a result, when the cross-shore gradient of the momentum flux due to the surface roller is larger than that of the radiation stress, the peak of the longshore current velocity is shifted shoreward. The present model therefore has a peak shoreward of the bar crest.

5.7 Conclusions

A one-dimensional model for undertow and longshore current was developed and calibrated using the undertow velocities measured over longshore bars at HORS. In the calibration, the parameter C_A, which is the ratio of the area of the surface roller to the square of the wave height, was found to be positively correlated with the surf similarity parameter at the wave breaking position, as expressed by Eq. (5.17).

The model with C_A given by Eq. (5.17) was then compared with undertow and longshore current velocities measured in large-scale experiments and in the field. The present model yielded good predictions for the undertow velocities over the longshore bars, whereas a previous model calibrated with small-scale experimental data underestimated the velocities. The cross-shore distributions of the longshore current over the longshore bars predicted with the previous model had peak velocities seaward

of the bar crests and did not fit the distributions measured in the field. The distributions predicted with the present model, however, had peaks shoreward of the bar crests and fitted those in the field.

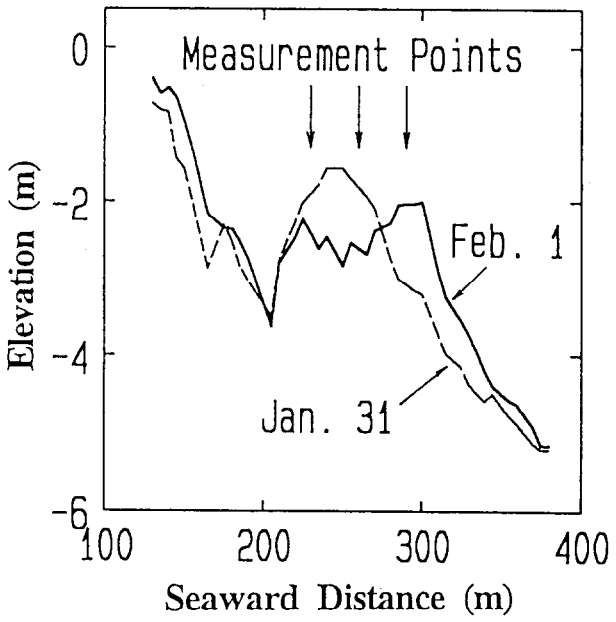

Figure 5.1 Locations of current meters and beach profiles on Jan. 31 and Feb. 1.

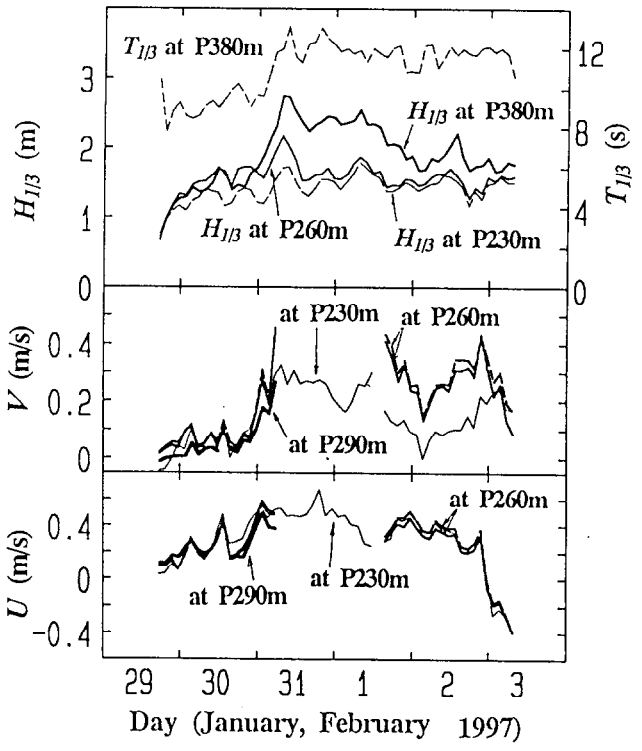

Figure 5.2 Time series of significant wave height $H_{1/3}$ and period $T_{1/3}$, undertow velocity V, and longshore current velocity U.

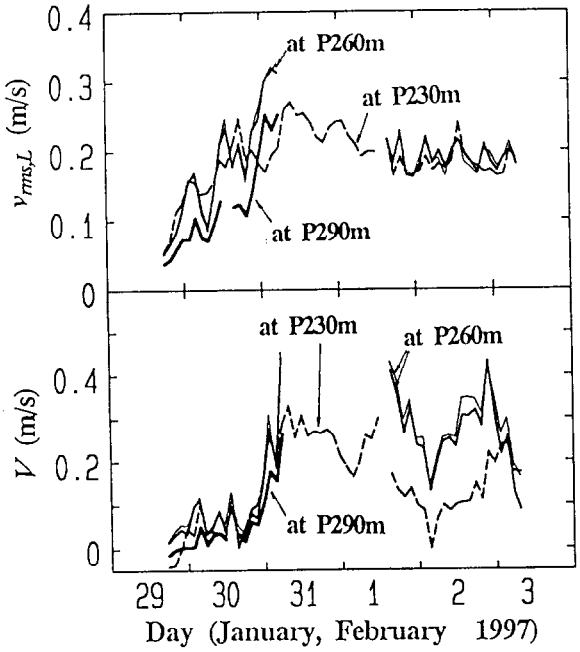

Figure 5.3 Time series of low-frequency component of cross-shore current velocity $v_{rms,l}$ and undertow velocity V.

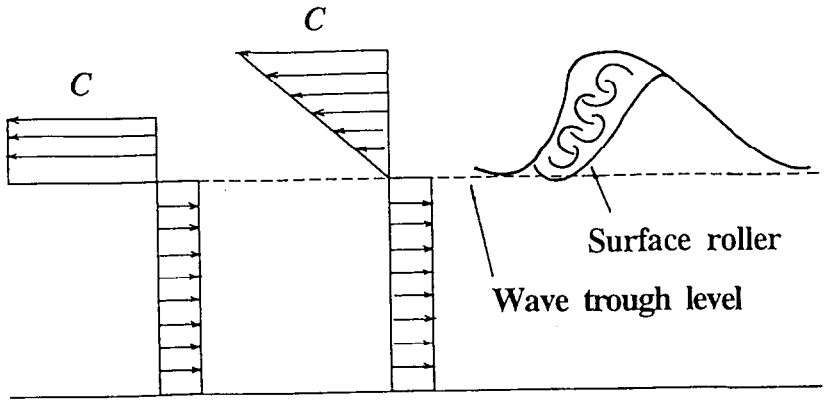

Figure 5.4 Vertical distribution of the time-averaged cross-shore current velocity assumed.

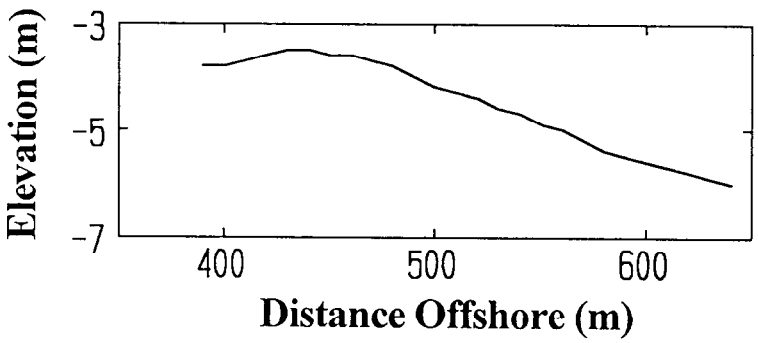

Figure 5.5 Beach profile seaward of the tip of HORS surveyed on Jan. 16, 1997.

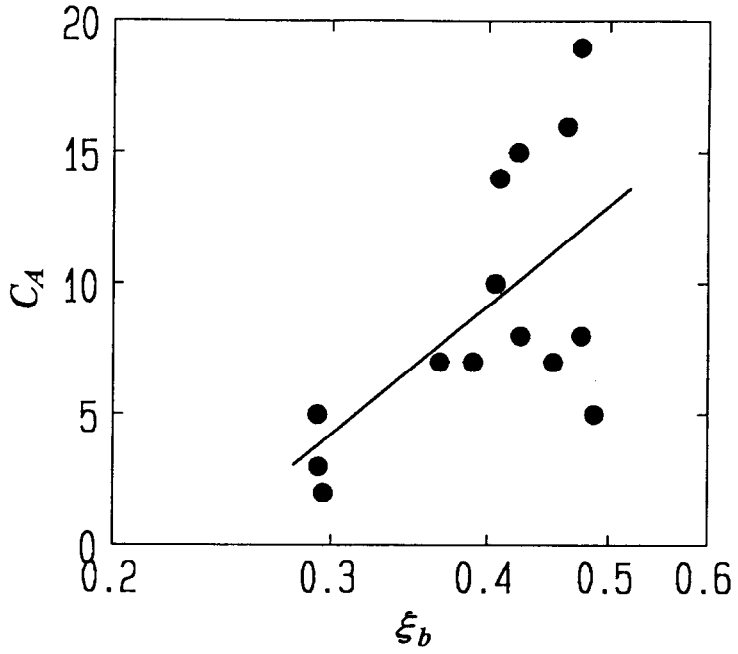

Figure 5.6 Relationship between C_A and ξ_β.

Table 5.1 Offshore boundary conditions and ξ_β in measurements at HORS in 1997

Case	$H_{1/3}$ (m)	$T_{1/3}$ (s)	θ	h (m)	η (m)	ξ_b
2	2.11	9.63	16.5	6.58	0.58	0.293
3	2.27	10.73	15.0	6.70	0.70	0.296
4	2.91	11.81	19.0	6.98	0.98	0.367
5	2.50	11.56	7.0	6.50	0.50	0.463
7	2.37	12.16	6.0	6.65	0.65	0.475
9	1.94	10.85	6.0	6.83	0.83	0.409

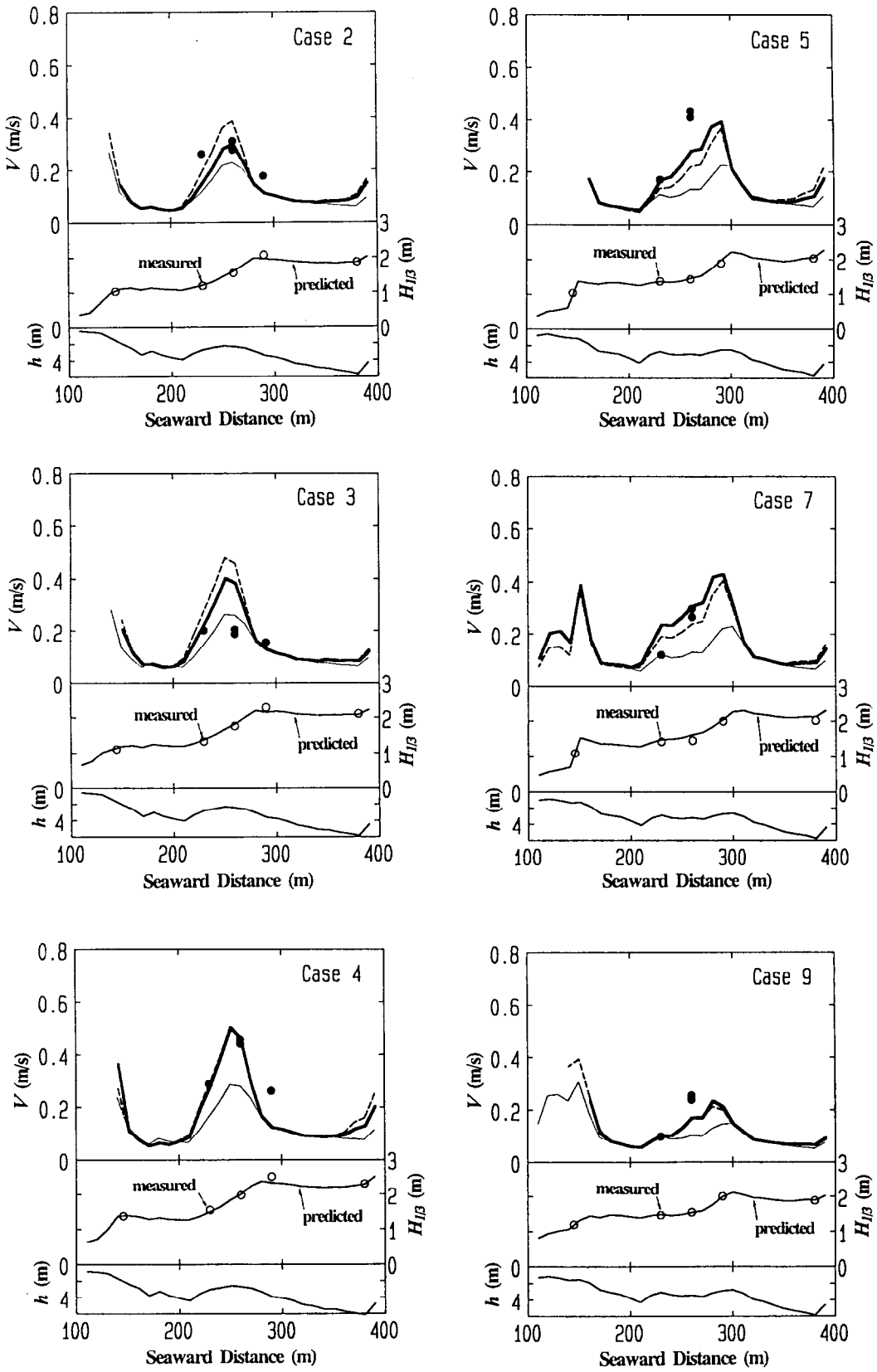

Figure 5.7 Comparisons of models with measurements at HORS in 1997. In the upper panels, the thick solid lines, the broken lines, and the thin solid lines show the values predicted using Eq. (5.17), C_A=7, and the S&DV model. The solid circles show the measured values.

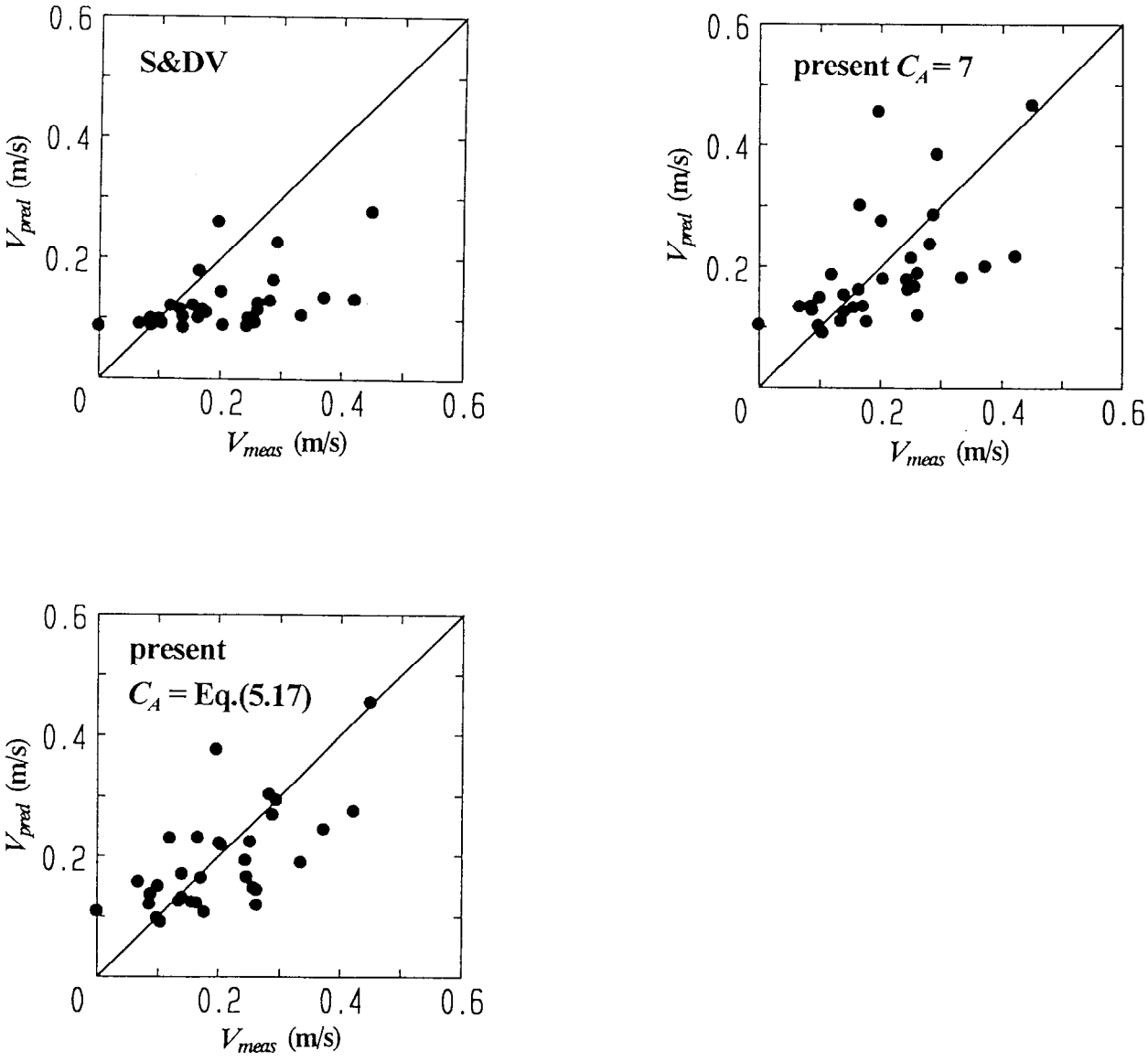

Figure 5.8 Comparisons of undertow velocities measured V_{meas} and predicted V_{pred}.

Table 5.2 Offshore boundary conditions in DELILAH and Delta Flume '93 Experiments

Case	H_{rms} (m)	T_p (s)	θ	H (m)
Oct. 19	0.75	7	15.1	2.63

Case	H_{m0} (m)	T_p (s)	h (m)
1b	1.40	5	4.1
1c	0.60	8	4.1

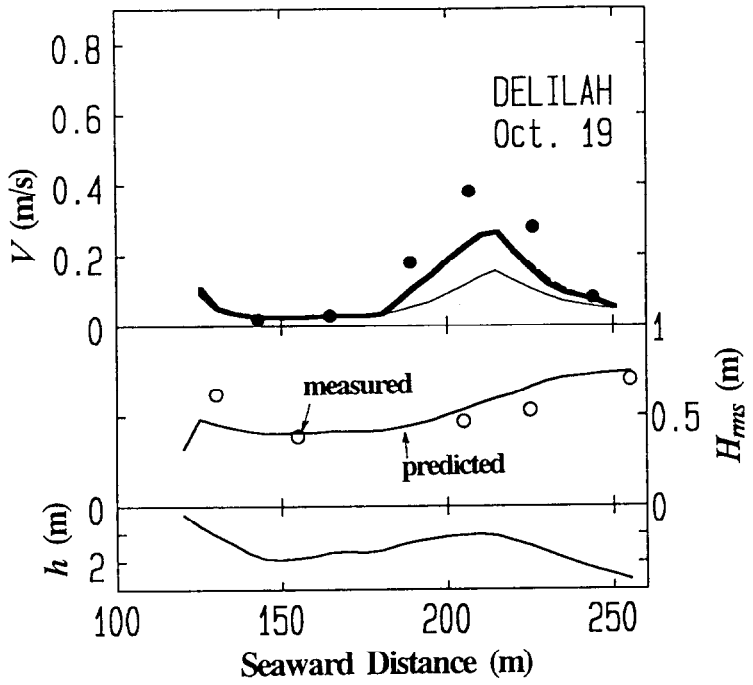

Figure 5.9 Comparison of undertow models with DELILAH measurement (Details are as in Figure 5.7).

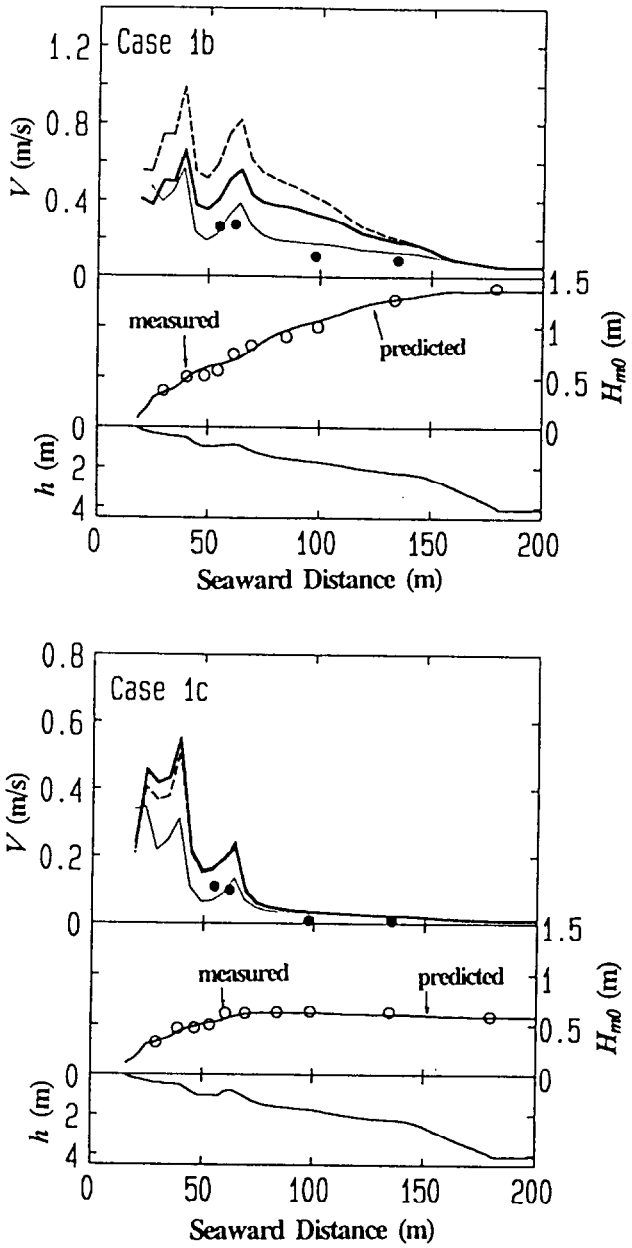

Figure 5.10 Comparisons of undertow models with Delta Flume '93 Experiments (Details are as in Figure 5.7).

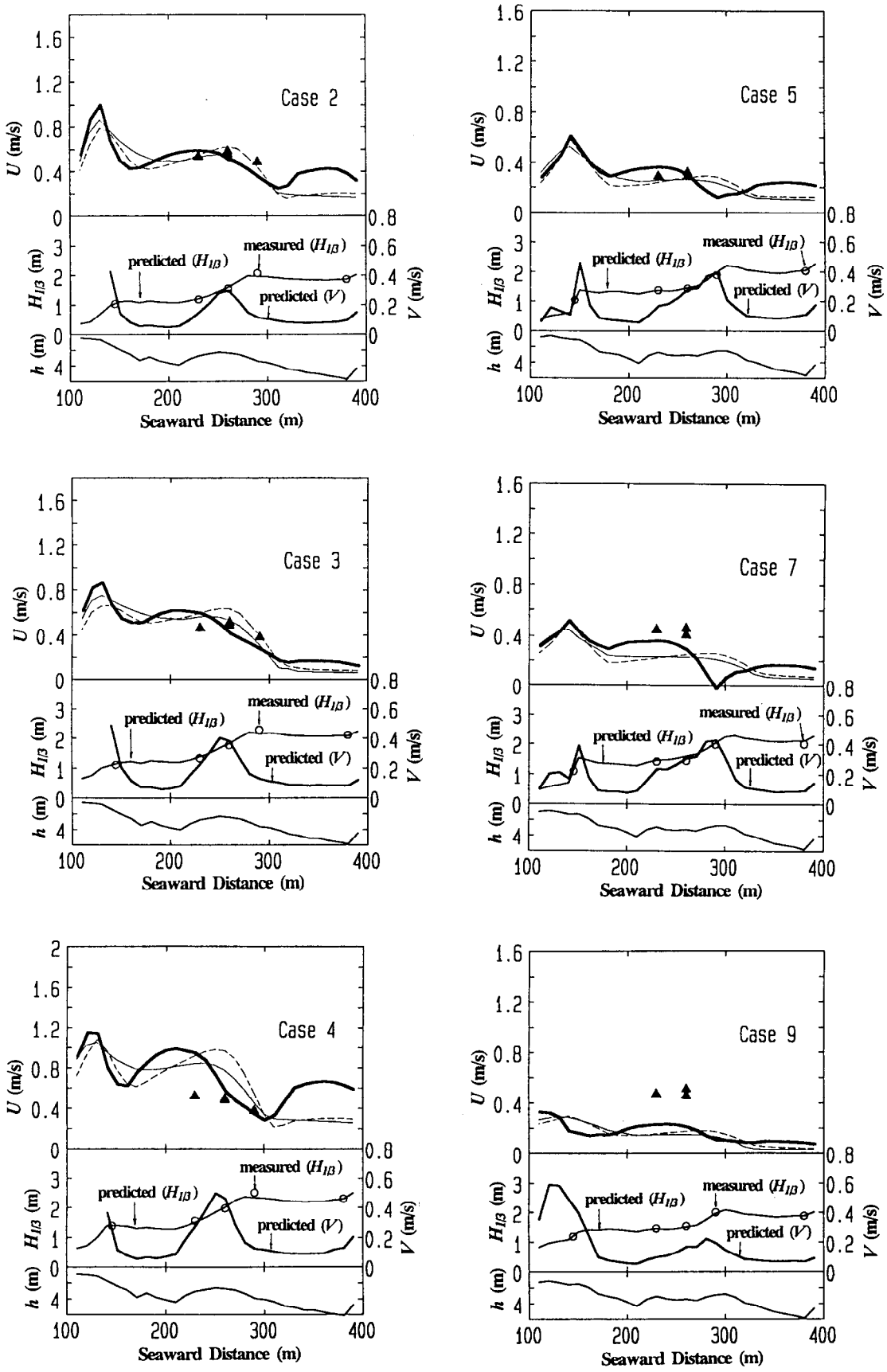

Figures 5.11 Comparisons of longshore current models with measurements at HORS in 1997. In the upper panels, the thick solid lines, the broken lines, and the thin solid lines show the values predicted with Eq. (5.17), the R&B model, and the no-roller model. The solid triangles represent the measured values.

Table 5.3 Offshore boundary conditions at HORS in 1989 and in DELILAH

Case	$H_{1/3}$ (m)	$T_{1/3}$ (s)	θ	S_{max}	h (m)
89-1	3.20	11.20	20	90	5.6
89-2	2.47	8.86	25	40	6.1
89-3	2.03	8.40	10	45	6.1

Case	H_{rms} (m)	T_p (s)	θ	h (m)
Oct. 14	1.03	9.7	24.8	4.85

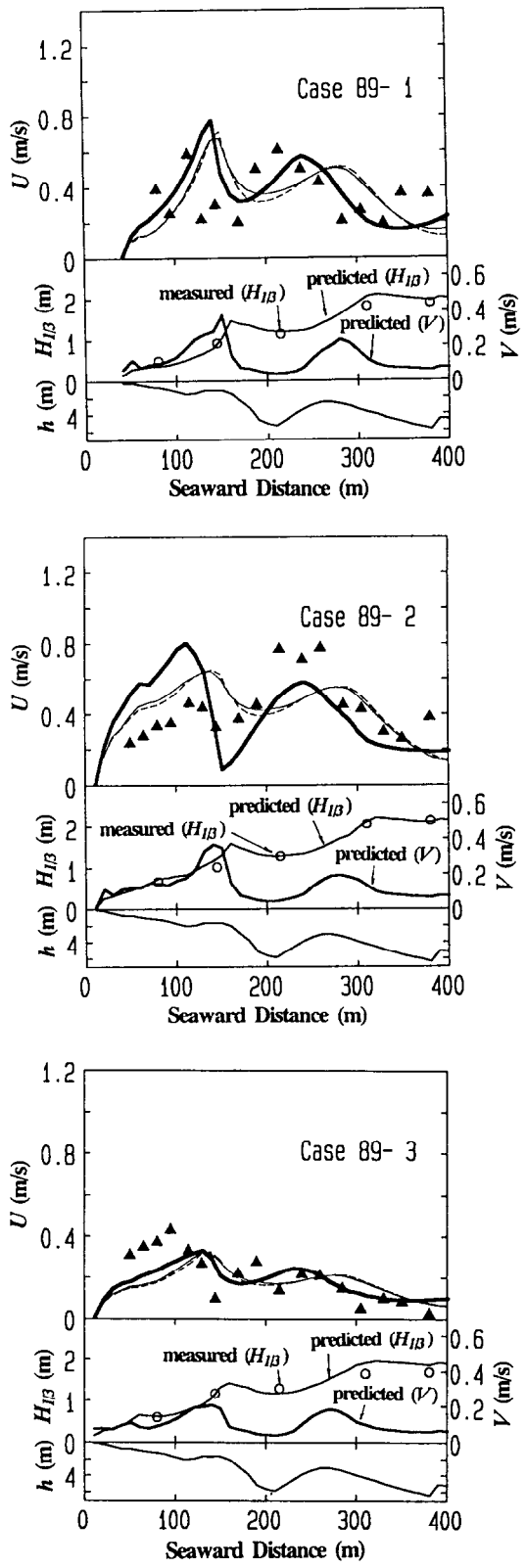

Figure 5.12 Comparisons of longshore current models with measurements at HORS in 1989 (Details are as in Figure 5.11).

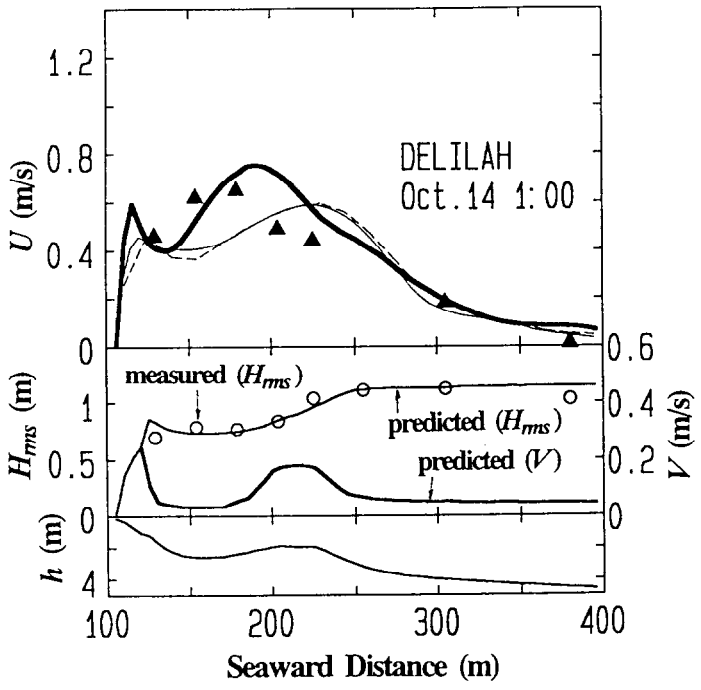

Figure 5.13 Comparison of longshore current models with DELILAH measurement (Details are as in Figure 5.11).

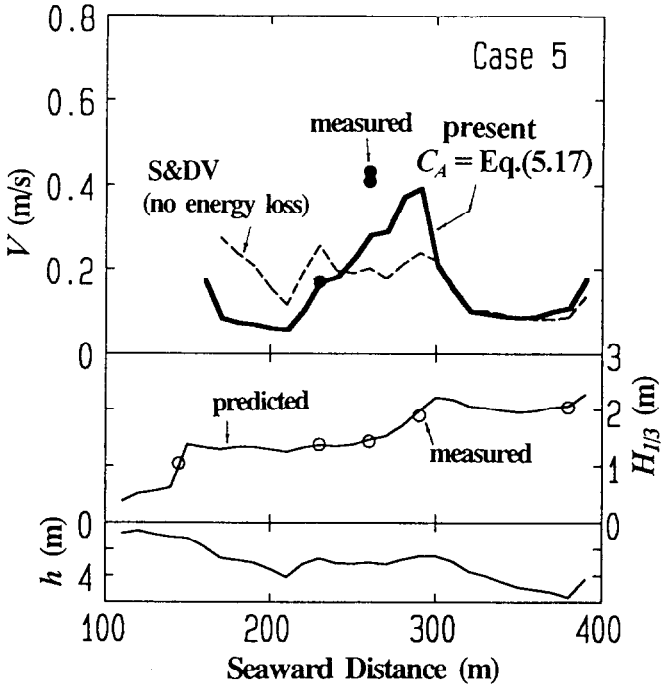

Figure 5.14 Comparison of undertow models with the measurement in Case 5 at HORS.

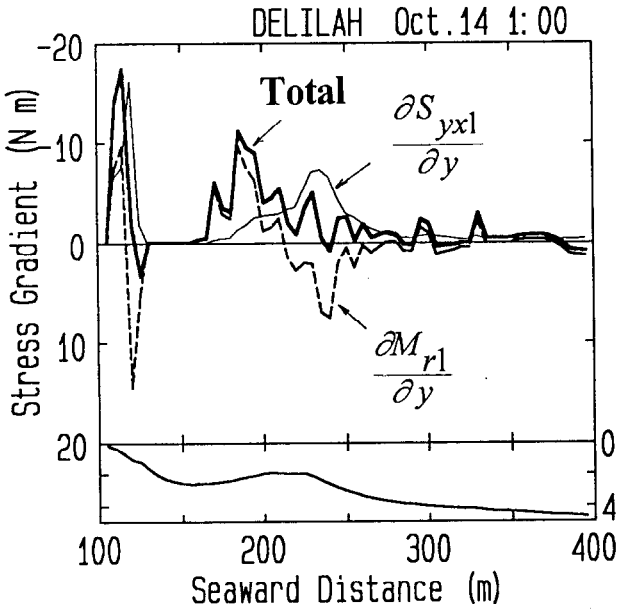

Figure 5.15 Cross-shore gradients of radiation stress ($\partial S_{yxl} / \partial y$, thin solid line), momentum flux due to surface roller ($\partial M_{rl} / \partial y$, broken line) and total stress (thick solid line) in the DELILAH measurement. The lower panel shows the beach profile.

6. Summary and Conclusions

The surf zone, extending from the wave breaking position to the shore, has strong impacts on the safety of property behind the beach, as well as on the sediment budget and the ecosystem. This is because it is a zone of active sediment movement and because it forms the transition between the marine and terrestrial environments.

Longshore bars are frequently formed in the surf zone. On barred beaches, waves break over bar crests and reform at troughs. Since wave reforming is peculiar on barred beaches, the hydro- and morpho-dynamics on barred beaches are different from those on planar beaches. These dynamics on barred beaches, however, have rarely been studied systematically using field data because data collection in the surf zone is difficult.

In this study, therefore, field measurements and numerical simulations were performed on waves, currents and morphological variations on barred beaches. The field data were obtained since 1986 at Hazaki Oceanographical Research Station (HORS), which is a research facility for field measurements in the nearshore zone and has a 427-m-long pier.

In Chapter 2, the beach profile data obtained almost daily for eight years at HORS showed that bar crests at Hasaki migrated seaward like other bar crests on coasts in the United States, the Netherlands, and New Zealand. However, the one-year duration time of the bar crest migration at Hasaki is shorter than those on the other coasts. The difference between the duration time at HORS and that in the Netherlands can be explained by the difference in the nearshore slope, though the difference between the duration time at HORS and those in the United States and New Zealand cannot be explained by the difference in the slope.

Although the bar crest migrated only seaward, the cross-shore sediment transport associated with the bar crest migration fluctuated seaward and shoreward. Seaward sediment transport occurred on and around bar crests and induced the seaward migration of the bar crest. Shoreward sediment transport, on the other hand, occurred in trough regions and contributed to the generation of the next bar. The areas with seaward and shoreward sediment transport moved as the bar crests and the troughs moved, respectively.

The magnitude of the cross-shore sediment transport rate varied temporally and

spatially. The temporal variation corresponded to the offshore wave energy; when the energy was large, the shoreward and seaward sediment movement was active. The beach profile data at HORS and a simple model showed that the spatial and the temporal variations in sediment transport rate caused the development and decay of the bar.

Field measurements of wave height and modes of wave breaking, breaking or non-breaking, at HORS described in Chapter 3 showed that the wave height-water depth ratio at wave reforming in the field was 0.35. The result that most wave height-water depth ratios at wave reforming of individual waves in the field were smaller than those in small-scale experiments is likely to indicate that waves in the field tend to continue breaking over longer relative distances than those in small-scale experiments.

A model for significant wave height and the fraction of breaking waves including the criterion for wave reforming was developed using the wave-by-wave approach. In the model, the criterion for wave reforming is H_r/h_r=0.35, and that for wave breaking is Eqs. (3.8) and (3.10), which were calibrated with small-scale experimental data. Comparisons among the model, field data and large-scale experimental data showed that the model almost agree with the measurements. However, the predicted values of wave height and the fraction of breaking waves at troughs are smaller than those measured in the field. This seems to indicate that the ratio of wave dissipation rate to the wave height is smaller in the field than in small-scale experiments.

In Chapter 4, the cross-shore distribution of the time-averaged longshore current velocity on a barred beach was discussed on the basis of fifty-two distributions obtained with a spherical float at HORS during four years. The results show that eighty-five percent of the distributions had peak velocities shoreward of the bar crests. A previously proposed model for nearshore current, however, could not reproduce the distribution. Mass and momentum fluxes due to the surface roller, which were neglected in the previous model, are considered to play a significant role in producing the longshore current with a peak velocity shoreward of the bar crest.

Hence, in Chapter 5, a one-dimensional model that included the surface roller effect was developed for undertow and longshore current velocities. The calibration of the model using undertow velocities measured over longshore bars at HORS showed that the ratio of the area of the surface roller to the square of the wave height was positively

correlated with the surf similarity parameter at the wave breaking position.

The model was then compared with undertow and longshore current velocities measured in large-scale experiments and in the field. The present model provided good predictions of the undertow velocities over the longshore bars, whereas a previously proposed model calibrated with small-scale experimental data underestimated the velocities. The cross-shore distribution of the longshore current velocity over the longshore bars predicted with the previous model had peak velocities seaward of the bar crests and was not consistent with the distributions measured in the field. However, the present model correctly predicted the distributions observed in the field with peaks shoreward of the bar crests. The result indicates that the momentum flux due to the surface roller is a cause of the cross-shore distribution of the longshore current velocity with a peak shoreward of the bar crest.

Through this study, the medium-term bar behavior and the associated sediment transport were revealed on the basis of the beach profile data at HORS. The models for waves and undertow and longshore current velocities were developed using the results of the field measurements of waves and nearshore currents at HORS, and their validity was confirmed using other data.

For predicting bar movement with high accuracy, several questions remain to be answered. These include the cross-shore distribution of suspended sediment concentration over a longshore bar and the effect of the size and the location of a longshore bar on the development of low-frequency waves and currents. These questions will be a part of future investigations at HORS.

Acknowledgements

I would like to thank Professor Kazuo Nadaoka for valuable suggestions and thoughtful guidance through this study. Thanks are also due to Professors Syunsuke Ikeda, Katsuki Takiguchi and Syuuji Fujii, and Dr. Hiroshi Yagi for stimulating discussions and useful comments to improve this manuscript. Instructive training from Professor Isao Irie and Dr. Kazumasa Katoh while I worked under them is greatly appreciated. I am also grateful to Professor Masaki Sawamoto for continuous encouragement since I studied in his laboratory.

Finally, special thanks are extended to my colleagues at HORS, who have been conducted field surveys even in miserable storms. Without them, this study would not have been completed. The colleagues are Shin-ichi Yanagishima, Hiroyuki Murakami, Tomoyoshi Isogami, Satoshi Nakamura, Masato Fukuda, Yasushi Ozaki, Norio Mochizuki, Toshiyuki Nakatsukasa, Yusuke Uchiyama, Tsuyoshi Nakashima and Satoshi Ueoka.

References

Aagaard, T. and Greenwood, B. (1999): Directionality cross-shore sediment transport in the surf zone under high-energy conditions, *Coastal Sediments '99*, ASCE, pp.1003-1018.

Allender, J.H. and Ditmars, J.D. (1981): Field measurements of longshore currents on a barred beach, *Coastal Eng.*, 5, pp.295-309.

Aubrey, D.G. (1979): Seasonal patterns of onshore/offshore sediment movement, *J. Geophys. Res.*, Vol.84, No.C10, pp.6347-6354.

Bailard, J.A. (1982): Modeling on-offshore sediment transport in the surf zone, *Proc. 18th Coastal Eng. Conf.*, ASCE, pp.1419-1438.

Battjes, J.A. (1975) : Modeling of turbulence in the surf zone, *Symp. on Modeling Techniques*, pp.1050-1061.

Battjes, J.A. and Janssen, J.P.F.M. (1978) : Energy loss and set-up due to breaking of random waves, *Proc. 16th Coastal Eng. Conf.*, ASCE, pp.569-587.

Battjes, J.A. and Stive, M.J.F. (1985) : Calibration and verification of a dissipation model for random breaking waves, *J. Geophys. Res.*, Vol.90, No.C5, pp.9159-9167.

Birkemeier, W.A. (1984): Time scales of nearshore profile changes, *Proc. 19th Coastal Eng. Conf.*, ASCE, pp.1507-1521.

Bowen, A.J. (1980): Simple models of nearshore sedimentation, beach profiles and longshore bars, *The Coastline of Canada* (ed. by MaCann, S.B.), Geological Survey of Canada, pp.1-11.

Church, J.C. and Thornton, E.B. (1992): Bottom stress modification by breaking waves within a longshore current model, *Proc. 23rd Coastal Eng. Conf.*, ASCE, pp.3012-3025.

Church, J.C. and Thornton, E.B. (1993) : Effects of breaking wave induced turbulence within a longshore current model, *Coastal Eng.*, 20, pp.1-28.

Dally, W.R., Dean, R.G. and Dalrymple, R.A. (1985): Wave height variation across beaches of arbitrary profile, *J. Geophys. Res.*, Vol.90, No.C6, pp.11,917-11,927.

Dally, W.R. (1992) : Random breaking waves: field verification of a wave-by-wave algorithm for engineering application, *Coastal Eng.*, 16, pp.369-397.

Dally, W.R. and Brown, C.A. (1995) : A modeling investigation of the breaking wave

roller with application to cross-shore currents, *J. Geophys. Res.*,Vol.100, No.C12, pp.24873-24883.

Deigaard, R., Justesen, P. and Fresoe, J. (1991) : Modelling of undertow by a one-equation turbulence model, *Coastal Eng.*, 15, pp.431-458.

De Vriend, H.J. and Stive, M.J.F. (1987) : Quasi-3D modelling of nearshore currents, *Coastal Eng.*, 11, pp.565-601.

Dibajnia, M., Shimizu, T. and Watanabe, A. (1994) : Profile change of a sheet flow dominated beach, *Proc. 24th Coastal Eng. Conf.*, ASCE, pp.1946-1960.

Ebersole, B.A. (1987) : Measurement and prediction of wave height decay in the surf zone. *Coastal Hydrodynamics*, ASCE, pp.1-16.

Ebersole, B.A. and Dalrymple, R.A. (1980): Numerical modeling of nearshore circulation, , *Proc. 17th Coastal Eng. Conf.*, ASCE, pp.2710-2725.

Faria, A.F.G., Thornton, E.B. and Stanton, T.P. (1996): Small-scale morphology related to wave and current parameters over a barred beach, *Proc. 25th Coastal Eng. Conf.*, ASCE, pp.3391-3404.

Fleischack, P.C. and de Freitas, A.J. (1989) : Physical parameters influencing the zonation of surf zone benthos, *Estuarine, Coastal and Shelf Science*, 28, pp.517-530.

Gallagher, E.l., Elgar, S. and Guza, R.T. (1998): Observations of sand bar evolution on a natural beach, *J. Geophys. Res.*, Vol.104, No.C7, pp.3203-3215.

Galloway, J.S., Collins, M.B. and Moran, A.D. (1989) : Onshore/offshore wind influence on breaking waves: an empirical study, *Coastal Eng.*, 13, pp.305-323.

Goda, Y. (1970): A synthesis of breaker indices, *Trans. Japan Soc. Civil Engrs.*, Vol.2, Part 2, pp.227-230.

Goda, Y. (1975): Irregular wave deformation in the surf zone, *Coastal Eng. in Japan*, Vol.18, pp.13-26.

Goda, Y. and Suzuki, Y. (1975): Computation of refraction and diffraction of sea waves with Mitsuyasu's directional spectrum, *Tech. Note Port and Harbour Res. Inst.*, No.230, 45p. (*in Japanese*)

Goda, Y. (1983) : A unified nonlinearity parameter of water waves, *Rep. Port and Harbour Res. Inst.*, Vol.22, No.3, pp.3-30.

Greenwood, B. and Sherman, D.J. (1986): Longshore current profiles and lateral mixing across the surf zone of a barred nearshore, *Coastal Eng.*, 10, pp.149-168.

Greenwood, B. and Osborne, P.D. (1991): Equilibrium slopes and cross-shore velocity asymmetries in a storm-dominated, barred nearshore system, *Marine Geology*, 96, pp.211-235.

Higano, J. and Yasunaga, N. (1988): The change in beach profile and bivalve distribution on a sandy beach facing to open sea, *Proc. Coastal Eng.*, JSCE, Vol.35, pp.767-771. (*in Japanese*)

Horie T., Sato, S. and Murakami, K. (1977): Boundary treatment on tidal computation, *17th Congress of the International Association for Hydraulic Research*, Vol.2, pp.359-366.

Horikawa, K. and Kuo, C.T. (1966) : A study on wave transformation inside surf zone, *Proc. 10th Coastal Eng. Conf.*, ASCE, pp.217-233.

Karlsson, T. (1969): Refraction of continuous ocean wave spectra, *J. Waterways and Harbors Div., Proc. of the ASCE*, Vol.95, No.WW4, pp.437-448.

Katoh, K. and Yanagishima, S. (1995): Changes of sand grain distribution in the surf zone, *Coastal Dynamics '95*, pp.639-650.

Komar, P. A. (1998): Beach Processes and Sedimentation, Second Edition, Prentice-Hall Inc., 544p.

Kuriyama, Y. (1991) : Investigation of cross-shore sediment transport rates and flow parameters in the surf zone using field data, *Rep. Port and Harbour Res. Inst.*, Vol.30, No.2, pp.3 - 58.

Kuriyama, Y., Katoh, K. and Ozaki, Y. (1992): Longshore current distribution, bottom profiles and waves, *Proc. Coastal Eng.*, JSCE, Vol.39, pp.196-200. (*in Japanese*)

Kuriyama, Y. and Ozaki, Y. (1993) : Longshore current distribution on a bar-trough beach –Field measurements at HORF and numerical model-, *Rep. Port and Harbour Res. Inst.*, Vol.32, No.3, pp.3 - 37.

Kuriyama, Y. (1994): Numerical model for longshore current distribution on a bar-trough beach, *Proc. 24th Coastal Eng. Conf.*, ASCE, pp.2237-2251.

Kuriyama, Y. (1996): Cross-shore movements of longshore bars, *Proc. Coastal Engineering*, JSCE, Vol.43, pp.576-580. *(in Japanese)*

Kweon, H.M. and Goda, Y. (1994) : The study of energy dissipation of regular wave on the arbitrary profile, *Proc. Civil Eng. in Ocean*, Vol.10, JSCE, pp.31-36. (*in Japanese*)

Larson, M. and Kraus, N.C. (1991): Numerical model of longshore current for bar and trough beaches, *J. Waterway, Port, Coastal, and Ocean Eng.*, Vol.117, No.4, ASCE, pp.326-347.

Larson, M. and Kraus, N.C. (1992): Dynamics of longshore bars, *Proc. 23rd Coastal Eng. Conf.*, ASCE, pp.2219-2232.

Larson, M., Capobianco, M., and Hanson, H. (2000): Relation-ship between beach profiles and waves at Duck, North Carolina, determined by canonical correlation analysis, *Marine Geology*, 163, pp.275-288.

Lippmann, T.C. and Holman, R.A. (1990): The spatial and temporal variability of sand bar morphology, *J. Geophys. Res.*, Vol.95, No.C7, pp.11575-11590.

Lippmann, T.C., Holman, R.A. and Hathaway, K.K. (1993): Episodic, nonstationary behavior of a double bar system at Duck, North Carolina, U.S.A., 1986-1991, *J. Coastal Res.*, Special Issue 15, pp.49-75.

Longuet-Higgins, M.S. (1970): Longshore current generated by obliquely incident waves, 1&2, *J. Geophys. Res.*, Vol.75, No.33, pp.6778-6801.

McLellan, T.N. and Kraus, N.C. (1991) : Design guidance for nearshore berm construction, *Coastal Sediments* '91, ASCE, pp.2000-2011.

Miller, H.C., Birkemeier, W.A. and DeWall, A.E. (1983): Effects of CERC research pier on nearshore processes, *Coastal Structure '93*, pp.769-784.

Miller, H.M., Smith, S.J., Hamilton, D.G. and Resio, D.T. (1999): Cross-shore transport processes during onshore bar migration, *Coastal Sediments '99*, ASCE, pp.1065-1080.

Murray, R.J., Robinson, D.A. and Soward, C.L. (1994) : South Gold Coast Beach nourishment project: Implementation, results, effectiveness, *Terra et Aqua*, Number 56, pp.12-23.

Nadaoka, K. and Kondoh, T. (1982): Laboratory measurements of velocity field structure in the surf zone by LDV, *Coastal Eng. in Japan*, Vol.25, pp.125-146.

Nadaoka, K., Hino, M. and Koyano, Y. (1989): Structure of the turbulent flow field under breaking waves in the surf zone, *J. Fluid Mech.*, Vol.204, pp.359-387.

Nadaoka, K., Yagi, H. and Etsudou, H. (1992): A modeling study of 3-D mass transport effects on nearshore current, *Proc. Coastal Eng.*, JSCE, Vol.39, pp.211-215. (*in Japanese*)

Nakamura, S., Katoh, K. and Ikeda, N. (1992): Generation of infragravity waves in breaking process of wave groups, *Proc. 23rd Coastal Eng. Conf.*, ASCE, pp.990-1005.

Nishi, R. (1994) : Probability of wave breaking on a plane beach, *Proc. International Symposium: Waves- Physical and Numerical Modelling*, pp.773-782.

Nishimura, H. (1988): Computation of nearshore current, *Nearshore Dynamics and Coastal Process - Theory, Measurements and Predictive Models* - (ed. by Horikawa, K.), University of Tokyo Press, pp.271-291.

Okayasu, A., Shibayama, T., and Horikawa, K. (1988): Vertical variation of undertow in the surf zone, *Proc. 21st Coastal Eng. Conf.*, ASCE, pp.478-491.

Okayasu, A., Watanabe, A. and Isobe, M. (1990): Modeling of energy transfer and undertow in the surf zone, *Proc. 22nd Coastal Eng. Conf.*, ASCE, pp.123-135.

Okayasu, A., Hara, K. and Shibayama, T. (1994): Laboratory experiments on a 3-D nearshore currents and a model with momentum flux by breaking waves, *Proc. 24th Coastal Eng. Conf.*, ASCE, pp.2461-2475.

Osiecki, D.A. and Dally, W.R. (1996) : The influence of rollers on longshore currents, *Proc. 25th Coastal Eng. Conf.*, ASCE, pp.3419-3430.

Plant, N.G. and Holman, R. (1997): Strange kinematics of sand-bars, *Coastal Dynamics '97*, ASCE, pp.355-364.

Plant, N.G., Holman, R.A. and Freilich, M.H. (1999): A simple model for interannual sandbar behavior, *J. Geophys. Res.*, Vol.104, No.C7, pp.15755-15776.

Rakha, K.A., Deigaard, R., Madsen, P.A., Brøker, I. and Rønberg, J.K. (1996) : Simulation of coastal profile development using a Boussinesq wave model, *Proc. 25th Coastal Eng. Conf.*, ASCE, pp.3048-3061.

Reniers, A.J.H.M., Thornton, E.B. and Lippmann, T.C. (1995): Longshore currents over barred beach, *Coastal Dynamics* '95, pp.413-424.

Reniers, A.J.H.M. and Battjes, J.A. (1997) : A laboratory study of longshore currents over barred and non-barred beaches, *Coastal Eng.*, 30, pp. 1-22.

Rivero F.J., Sanchez-Arcilla, A. and Beyer, D. (1994) : Comparison of a wave transformation model with LIP-11D data, *Coastal Dynamics '94*, ASCE, pp.518-532.

Roelvink, J.A. (1993) : Dissipation in random wave groups incident on a beach, *Coastal Eng.*, 19, pp.127-150.

Ruessink, B.G. and Kroon, A. (1994): The behaviour of a multiple bar system in the nearshore zone of Terschelling, the Netherlands: 1965-1993, *Marine Geology*, 121, pp.187-197.

Ruessink, B.G. and Terwindt, J.H.J. (2000): The behaviour of nearshore bars on the time scale of years: a conceptual model, *Marine Geology*, 163, pp.289-302.

Sallenger, Jr., A.H., Holman, R.A. and Birkemeier, W.A. (1985): Storm-induced response of a nearshore-bar system, *Marine Geology*, 64, pp.237-257.

Sallenger, Jr., A.H. and Howd, P.A. (1989): Nearshore bars and the break-point hypothesis, *Coastal Eng.*, 12, pp.301-313.

Sanchez-Arcilla, A., Roelvink, J.A., O'Connor, B.A., Reniers, A. and Jimenez, J. (1994): The Delta Flume '93 experiment, *Coastal Dynamics '94*, ASCE, pp.488-502.

Seyama, A. and Kimura, A. (1988) : The measured properties of irregular wave breaking and wave height change after breaking on the slope, *Proc. 21st Coastal Eng. Conf.*, ASCE, pp.419-432.

Shand, R.D. and Bailey, D.G. (1999): A review of net offshore bar migration with photographic illustrations from Wanganui, New Zealand, *J. Coastal Res.*, Vol.15, No.2, pp.365-378.

Shand, R.D., Bailey, D.G. and Shepherd, M.J. (1999): An inter-site comparison of net offshore bar migration characteristics and environmental conditions, *J. Coastal Res.*, Vol.15, No.3, pp.750-765.

Shimizu, T., Tsuru M. and Watanabe, A. (1994) : Field verification of a numerical model of beach topography change due to nearshore currents, undertow and waves, *Proc. 24th Coastal Eng. Conf.*, ASCE, pp.2610-2624.

Short, A.D. (1985): Rip-current type, spacing and persistence, Narrabeen Beach, Australia, *Marine Geology*, 65, pp.47-71.

Shuto, N. (1974): Nonlinear long waves in a channel of variable section, *Coastal Eng. Japan*, Vol.17, pp.1-12.

Smith, J.A. and Largier, J.L. (1995): Observations of nearshore circulation: Rip currents, *J. Geophys. Res.*, Vol.100, No.C6, pp.10967-10975.

Smith, J.M., Svendsen, I.A. and Putrevu, U. (1992): Vertical structure of the nearshore current at DELILAH: measured and modeled, *Proc. 23rd Coastal Eng. Conf.*, ASCE, pp.2825-2838.

Smith, J.M., Larson, M. and Kraus, N.C. (1993) : Longshore current on a barred beach: Field measurements and calculation, *J. Geophys. Res.*, Vol.98, No.C12, 22717-22731.

Southgate, H.N. and Nairn, R.B. (1993): Deterministic profile modelling of nearshore processes. Part1. waves and currents, *Coastal Eng.*, 19, pp.27-56.

Southgate, H.N. and Wallace, H.M. (1994) : Breaking wave persistence in parametric surf zone models, *Coastal Dynamics '94*, ASCE, pp.543-555.

Stive, M.J.F. and De Vriend, H.J. (1994) : Shear stresses and mean flow in shoaling and breaking waves, *Proc. 24th Coastal Eng. Conf.*, ASCE, pp.594-607.

Stive, M.J.F., Guillen, J. and Capobianco, M. (1996): Bar migration and duneface oscillation on decadal scales, *Proc. 25th Coastal Eng. Conf.*, ASCE, pp.2884-2896.

Sunamura, T. and Takeda, I. (1993): Bar movement and shoreline change: Predictive relations, *J. Coastal Res.*, Special Issue 15, pp.125-140.

Svendsen, I.A. (1984): Mass flux and undertow in a surf zone, *Coastal Eng.*, 8, pp.347-365.

Symonds, G. and Huntley, D.A. (1980): Waves and currents over nearshore bar systems, *Proc. of Canadian Coastal Conf.*, pp.64-78.

Takayama T., Ikeda, N. and Hiraishi, T. (1991): Practical computation method of directional random wave transformation, *Rep. Port and Harbour Res. Inst.*, Vol.30, No.1, pp.21-67. (*in Japanese*)

Takeda, I. and Sunamura, T. (1992): Conditions for beach erosion on a barred beach, *Zeit. Geomorph. N.F.*, 36, 4, pp.453-464.

Thornton, E.B. and Guza, R.T. (1982) : Energy saturation and phase speeds measured on a natural beach, *J. Geophys. Res.*, Vol.87, No.C12, pp.9499-9508.

Thornton, E.B. and Guza, R.T. (1983) : Transformation of wave height distribution, *J. Geophys. Res.*,Vol.88, No.C10, pp.5925-5938.

Thornton, E.B., Humiston, R.T. and Birkemeier, W. (1996): Bar/trough generation on a natural beach, *J. Geophys. Res.*, Vol.101, No.C5, pp.12097-12110.

Whitford, D.J. and Thornton, E.B. (1988): Longshore current forcing at a barred beach, *Proc. 21st Coastal Eng. Conf.*, ASCE, pp.77-90.

Wijnberg, K.M. and Wolf, F.C.J. (1994): Three-dimensional behaviour of a multiple bar system, *Coastal Dynamics '94*, pp.59-73.

Wijnberg, K.M. and Terwindt, J.H.J. (1995): Extracting decadal morphological

behaviour from high-resolution, long-term bathymetric surveys along the Holland coast using eigenfunction analysis, *Marine Geology*, 126, pp.301-330.

Winant, D.C., Inman, D.L. and Nordstrom, C.E. (1975): Description of seasonal beach changes using empirical eigenfunction, *J. Geophys. Res.*, Vol.80, No.15, pp.1979-1986.

Wright, L.D. and Short, A.D. (1983): Morphodynamics of beaches and surf zones in Australia, *CRC Handbook of Coastal Processes and Erosion*, edited by Komar, D., CRC Press Inc., pp.35-64.

Yamaguchi, M., Tanabe, H. and Nishioka, Y. (1983): A numerical solution of nearshore currents taking account of wave-induced mass flux, *Proc. 30th Japanese Conf. on Coastal Eng.*, JSCE, pp.480-484. (*in Japanese*)

Yamaguchi, M. (1988): A numerical model of nearshore currents due to irregular waves, *Proc. of the 21st Coastal Eng. Conf.*, ASCE, pp.1113-1126.

Yanagishima, S. and Katoh, K. (1990): Field observation on wave set-up near the shoreline, *Proc. 22nd Coastal Eng. Conf.*, ASCE, pp.95-108.

Yamamoto, K. and Sato, S. (1998): Large wave tank experiments on bar and berm formation due to irregular waves, *Proc. Coastal Engineering*, JSCE, Vol.45, pp.526-530. *(in Japanese)*